

SPRINGER BRIEFS IN EARTH SYSTEM SCIENCES

Mainak Choudhuri  
Michal Nemčok

# Mantle Plumes and Their Effects

 Springer

# **SpringerBriefs in Earth System Sciences**

## **Series editors**

Gerrit Lohmann, Bremen, Germany

Lawrence A. Mysak, Montreal, Canada

Justus Notholt, Bremen, Germany

Jorge Rabassa, Ushuaia, Argentina

Vikram Unnithan, Bremen, Germany

More information about this series at <http://www.springer.com/series/10032>

Mainak Choudhuri · Michal Nemčok

# Mantle Plumes and Their Effects

 Springer

Mainak Choudhuri  
Petroleum E & P  
Reliance Industries Limited  
Mumbai, Maharashtra  
India

Michal Nemčok  
Energy and Geoscience Institute  
University of Utah  
Salt Lake City, UT  
USA

and

EGI Laboratory at SAV  
Bratislava  
Slovakia

ISSN 2191-589X                      ISSN 2191-5903 (electronic)  
SpringerBriefs in Earth System Sciences  
ISBN 978-3-319-44238-9              ISBN 978-3-319-44239-6 (eBook)  
DOI 10.1007/978-3-319-44239-6

Library of Congress Control Number: 2016947195

© The Author(s) 2017

This work is subject to copyright. All rights are reserved by the Publisher, whether the whole or part of the material is concerned, specifically the rights of translation, reprinting, reuse of illustrations, recitation, broadcasting, reproduction on microfilms or in any other physical way, and transmission or information storage and retrieval, electronic adaptation, computer software, or by similar or dissimilar methodology now known or hereafter developed.

The use of general descriptive names, registered names, trademarks, service marks, etc. in this publication does not imply, even in the absence of a specific statement, that such names are exempt from the relevant protective laws and regulations and therefore free for general use.

The publisher, the authors and the editors are safe to assume that the advice and information in this book are believed to be true and accurate at the date of publication. Neither the publisher nor the authors or the editors give a warranty, express or implied, with respect to the material contained herein or for any errors or omissions that may have been made.

Printed on acid-free paper

This Springer imprint is published by Springer Nature  
The registered company is Springer International Publishing AG Switzerland

*To my wife, who helped me  
to finish this book quickly*

# Preface

This book attempts to collect the information that has been gathered from the literature survey during the preparation of a doctoral thesis and constitutes the theoretical background for it.

Plumes are hot, buoyant upwellings from the mantle that reach the base of the lithosphere, producing regions of excess volcanism on the surface, known as hot spots. The presence of a plume is debated hotly in the literature. But a hot spot is an unambiguous feature on the surface of the Earth. In this book, we have tried to describe the observable features on the crust that has been ascribed due to the presence of a plume. The surface elevations surrounding a hot spot have been explained by the presence of a plume head below the lithosphere. It results in a broad swell and uplift of the crust above the plume head, with a moat-like depression surrounding the erupting volcanoes. As the lithospheric plate moves away, it leaves a trail of extinct volcanoes and a distinctive stacking pattern of sediments in the moats around the volcanoes. These surface uplifts are of two types: a temporary dynamic uplift, which disappears when the plume-related thermal anomaly dissipates, and a permanent uplift due to crustal underplating from the plume magmatism. There are different methods to identify these uplifts and estimate their magnitude, both in the case of present day, or in the case of geological past.

The chapters in the book present a brief synopsis of the current academic understanding of the plume hypothesis, its surface manifestations, and shortcomings.

Chapter 1 prepares the background parameters for plume emplacement. It deals with the elastic properties of the lithosphere and estimation of the elastic thickness of the crust.

Chapter 2 introduces the plume hypothesis, discusses the major plume types, and briefly touched upon its effect on the lithosphere. It would make the reader conversant with the basic characteristic of a mantle plume.

Chapters 3 and 4 focus on, respectively, the dynamic and permanent topography produced by an impinging plume head below the lithosphere. Estimation of the uplifts from subsidence analysis is also discussed here.

Chapter 5 discusses the thermal effects of a plume head, thermal uplift, and interactions between a mid-oceanic ridge and a plume head.

Chapter 6 describes the geomorphic features of eruption centers, hotspot morphology, flux variation, and hydrothermal circulation in a hot spot, flexure around the hotspot track, and sedimentation in response to hotspot volcanism.

Finally, Chap. 7 touches upon the historical background of the plume hypothesis, its criticisms, and alternate ideas.

This book should be useful to research students studying lithospheric uplifts surrounding a hot spot and its estimation, or to the casual reader interested in the plume hypothesis.

At the end, we would like to thank Mr. Neeraj Sinha, Reliance Industries Limited, Navi Mumbai, and Dr. Rostilav Melichar, Masaryk University, Brno, for their encouragements during the preparation of the initial drafts of this book.

Mumbai, India  
Salt Lake City, USA

Mainak Choudhuri  
Michal Nemčok

# Contents

<b>1 Elastic Properties of the Lithosphere</b> . . . . .	1
1.1 Elastic Thickness of the Lithosphere . . . . .	1
1.2 Estimation of Elastic Thickness . . . . .	6
References. . . . .	16
<b>2 Plumes and Hotspots</b> . . . . .	19
2.1 Introduction . . . . .	19
2.2 The Plume Hypothesis . . . . .	20
2.3 Characteristics of Plumes . . . . .	22
2.4 Classification of Plumes . . . . .	24
2.4.1 Superplumes . . . . .	28
2.4.2 Secondary and Tertiary Plumes. . . . .	31
2.5 Plume-Related Lithospheric Uplift . . . . .	32
2.6 Morphology of Hotspot Tracks. . . . .	34
2.7 Moat and Arch . . . . .	37
References. . . . .	39
<b>3 Dynamic Crustal Uplift Due to Plume Activity</b> . . . . .	43
3.1 Ascent of a Mantle Plume . . . . .	43
3.2 Dynamic Uplift and Topography . . . . .	45
3.3 Timeframe and Factors for Dynamic Uplift . . . . .	49
3.4 Estimation of Dynamic Uplift. . . . .	51
References. . . . .	59
<b>4 Permanent Crustal Uplift Due to Plume Activity</b> . . . . .	63
4.1 Plume-Related Volcanism. . . . .	63
4.2 Permanent Uplift . . . . .	63
4.2.1 Factors for Permanent Uplift. . . . .	65
4.2.2 Identification and Estimation of Permanent Uplift. . . . .	65
References. . . . .	71
<b>5 Effects of Plume-Related Thermal Anomaly</b> . . . . .	73
5.1 Plume Heat Flow . . . . .	73

5.2	Thermal Uplift . . . . .	77
5.2.1	Thermal Rejuvenation Model . . . . .	78
5.3	Thermal Subsidence . . . . .	81
5.4	Plume-Ridge Interactions . . . . .	82
5.4.1	Ridge-Centred Plumes . . . . .	82
5.4.2	Off-Ridge Plumes . . . . .	83
5.4.3	Migrating Ridges . . . . .	84
5.4.4	Ridge Jump . . . . .	85
	References. . . . .	88
<b>6</b>	<b>Morphology of Hotspots . . . . .</b>	<b>91</b>
6.1	Growth of Submarine Volcanoes . . . . .	91
6.2	Morphogenesis of Eruption Centers . . . . .	92
6.3	Hotspot Volcano Spacing . . . . .	96
6.4	Magma Flux Variation . . . . .	99
6.5	Heat Flow and Hydrothermal Circulation . . . . .	102
6.6	Flexural Moat and Arch—Spatial and Temporal Development. . . . .	108
6.6.1	Deposition in Flexural Moat . . . . .	111
6.6.2	History of Moat Deposition. . . . .	118
	References. . . . .	119
<b>7</b>	<b>The Great Plume Debate . . . . .</b>	<b>125</b>
7.1	Brief History. . . . .	125
7.2	Problems/Critiques . . . . .	126
7.3	Plate Tectonic Considerations . . . . .	132
	References. . . . .	133

# Chapter 1

## Elastic Properties of the Lithosphere

### 1.1 Elastic Thickness of the Lithosphere

The elastic thickness ( $T_e$ ) is the computed thickness of a lithospheric plate that responds elastically to long term geological loading by flexure. The loading should take place for more than  $10^5$  years. The elastic thickness represents the integrated strength of the lithosphere and is a measure of its resistivity to deformation. Since the lithospheric yield strength envelopes indicate brittle failure in the upper crust and ductile behavior below, the elastic thickness is generally correlated with a part of the lithosphere that can support long term geological loads by flexing, which is termed as the “elastic core”. In contrast, the seismogenic thickness,  $T_s$ , represents the thickness of the uppermost brittle layer of the crust that responds to stresses by faulting and associated earthquakes.

There are two end members describing the long term behavior of the lithosphere under load, of which the elastic plate model (Gunn 1943) is the more successful one. In this model the lithosphere is treated as a thin elastic plate overlying an inviscid substratum. The differential equation for the deformation is given by:

$$Dd^4y/dx^4 + (\rho_m - \rho_{infill})yg = 0 \quad (1.1)$$

where  $D$  is the flexural rigidity of the plate,  $x$  is the distance along the surface before deformation,  $y$  is the deformation,  $\rho_m$  is the average density of the substratum (asthenospheric mantle), and  $\rho_{infill}$  is the average density of the material infilling the sediment catchment area created by the deformation.

If we put boundary conditions as (1) the elastic beam being infinite in length, (2) deformation being negligible at great distances from a line load  $P_b$  per unit width, and (3) a continuous, symmetrical deformation on either side of the load, the deformation (Fig. 1.1) is given by:

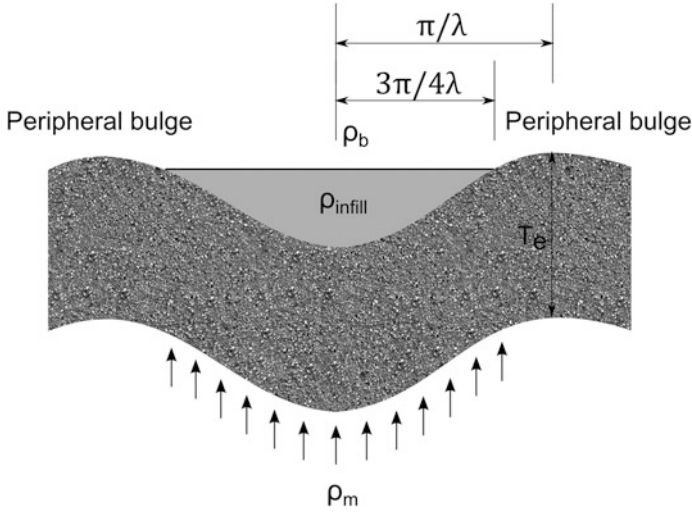


**Fig. 1.1** Flexure of a thin elastic plate over an inviscid substratum due to a line load with  $P_b$  per unit width (modified from Watts 1983)

$$y = \{P_b \lambda / 2(\rho_m - \rho_{\text{infill}})g\} e^{-\lambda x} \cdot (\cos \lambda x + \sin \lambda x) \quad (1.2)$$

where  $\lambda$  is a parameter determining the wavelength and amplitude of deformation, given by:

$$\lambda = \{(\rho_m - \rho_{\text{infill}})g/4D\}^{1/4}. \quad (1.3)$$

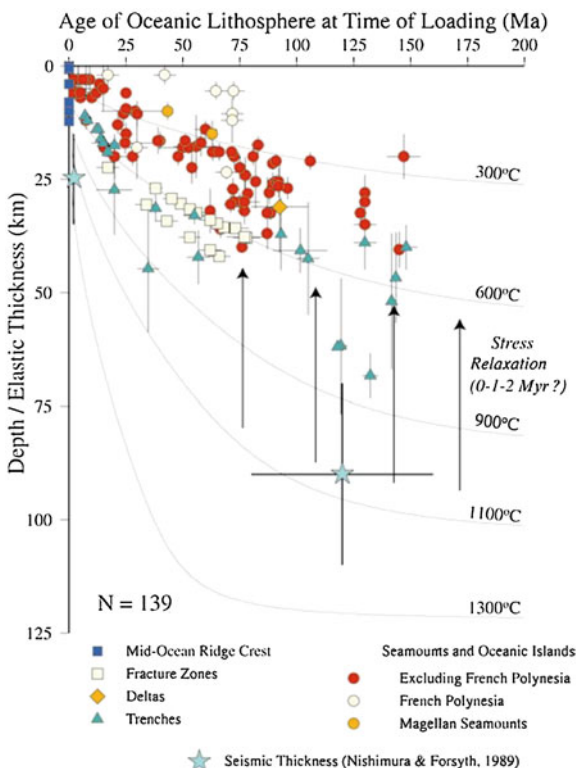
In this model, the elastic thickness of the deforming plate,  $T_e$ , is given by

$$T_e = \{D12(1 - \sigma^2)/E\}^{1/3} \quad (1.4)$$

where  $E$  is the Young's modulus and  $\sigma$  is the Poisson's ratio.

The elastic plate model have been very successful in predicting observed flexures in regions of volcanic and sediment loads, from which it has been possible to estimate long term elastic properties of the lithosphere and its relationship to both load and plate ages (e.g., Watts 1978; Caldwell and Turcotte 1979; Cazenave et al. 1980).  $T_e$  ranges from 2 to 40 km for the oceanic crust. It shows a clear dependency on plate and load ages. For the continental crust,  $T_e$  ranges from 0 to 100 km and has no clear age relationship. A plot of  $T_e$  versus age of the oceanic lithosphere at the time of loading (Watts and Zhong 2000, Table 1, p. 858) shows that younger lithosphere has  $T_e$  much lower than that of the older lithospheres (Fig. 1.2). The  $T_e$  estimates closely follow the depth of the 300–600 °C isotherm calculated from a cooling plate model, which was first pointed out by Watts (1978).

**Fig. 1.2** Plot of elastic thickness of the oceanic lithosphere against the age of the lithosphere at the time of loading (Watts and Zhong 2000)

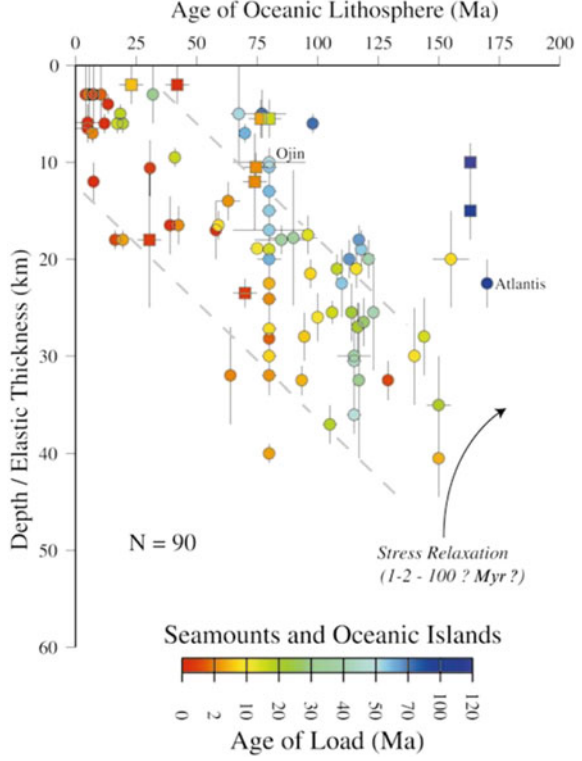


A similar plot of  $T_e$  with age of lithosphere (Watts and Zhong 2000; Fig. 1.3) suggests that older seamounds have a lower  $T_e$  than younger ones for the same age of the lithosphere. This indicates a load-induced relaxation of the lithosphere, and change in the flexural rigidity, all of which suggest visco-elastic behavior. The visco-elastic model of the lithosphere encompasses the change in  $T_e$  with time by assuming an initial elastic flexure, followed by viscous relaxation with time (Fig. 1.4). The flexural equation for a visco-elastic plate overlying an inviscid substratum is given by Nadai (1963) as:

$$D_0 \partial^4 y / \partial x^4 + (\rho_m - \rho_{infill}) g (\tau y' + y) = 0 \tag{1.5}$$

where  $D_0$  is the instantaneous flexural rigidity of the plate,  $\tau$ , equal to  $\eta/E$  where  $\eta$  is the viscosity and  $E$  is the Young's modulus, is the Maxwell relaxation time and  $y'$  is the derivative of  $y$  with respect to time. For an applied load of the form  $(\rho_l - \rho_w) g h \cos(kx)$ , the displacement is given by Watts (2001):

**Fig. 1.3** Plot of elastic thickness of the oceanic lithosphere against the age of the lithosphere at seamounts and oceanic islands (Watts and Zhong 2000)



$$y = \frac{(\rho_l - \rho_w)g h \cos(kx)}{(\rho_m - \rho_{infill}) \left[ 1 + \frac{D_0 k^4}{(\rho_m - \rho_{infill})g} \right]} \left[ 1 + \frac{D_0 k^4}{(\rho_m - \rho_{infill})g} \left[ 1 - e^{-t/\tau} \left\{ 1 + \frac{D_0 k^4}{(\rho_m - \rho_{infill})g} \right\} \right] \right]^{-1} \quad (1.6)$$

where  $\rho_l$  is the load density,  $\rho_w$  is the density of the displaced material (water/air),  $h$  is the height of the load measured from peak and trough amplitude, and  $k$ , equal to  $2\pi/\lambda_w$  where  $\lambda_w$  is the wavelength of deformation, is the wave-number of the load in the direction of  $x$ .

$$\text{For } t \rightarrow 0, \quad y \rightarrow (\rho_l - \rho_w)h \cos(kx)/(\rho_m - \rho_{infill}) \cdot \left\{ 1 + D_0 k^4/(\rho_m - \rho_{infill})g \right\}^{-1} \quad (1.7)$$

and

$$\text{for } t \rightarrow \infty, \quad y \rightarrow (\rho_l - \rho_w)h \cos(kx)/(\rho_m - \rho_{infill}). \quad (1.8)$$

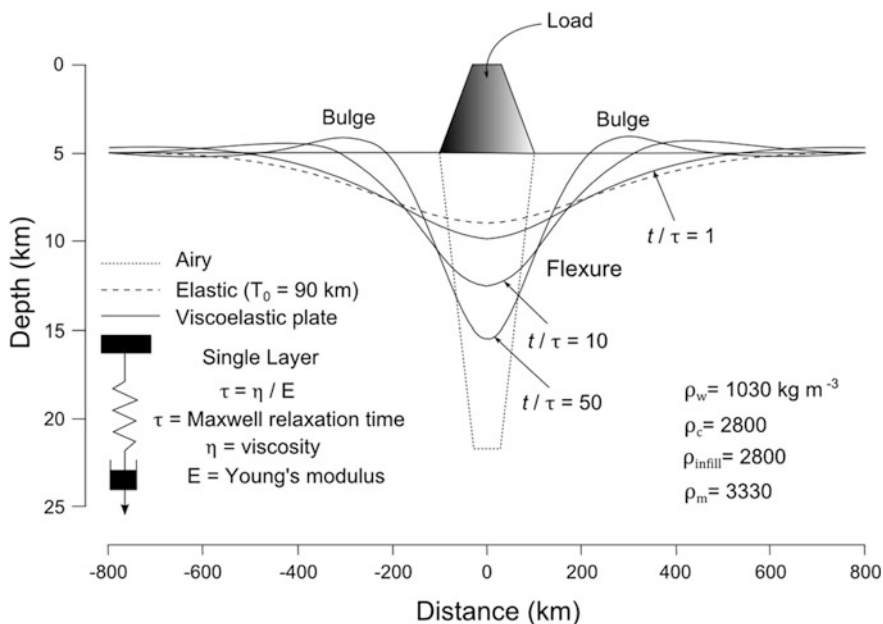


**Fig. 1.4** Flexure of a thin visco-elastic plate over an inviscid substratum (modified from Watts and Zhong 2000)

Thus, for short loading time, the visco-elastic plate behaves like an elastic plate with flexural rigidity  $D_0$ , while for long duration of loading it approaches Airy isostasy, if both  $\rho_l$  and  $\rho_{infill} \rightarrow \rho_c$ , which is the crustal density (Watts 2001). The rate at which the short-term elastic behavior gives way to the long-term viscous behavior depends on the width of the load. A wide load reaches Airy response more rapidly than narrow load (Fig. 1.5).

The visco-elastic model is more popular than the elastic model due to its time-variant nature of deformation. Numerous authors (e.g., Walcott 1970; Sleep and Snell 1976; McNutt and Parker 1978; Lambeck and Nakiboglu 1981; Quinlan and Beaumont 1984) have used this model to explain the lithospheric flexure. An implication of the visco-elastic model is that on long timescales, the response of the lithosphere to loads approaches that of the Airy mechanism. This is in contradiction to gravity/geoid and seismic studies of old volcanic islands such as the Emperor Chain, which are supported by flexure of the lithosphere. An improvement on this problem is a multilayered visco-elastic model, used, for example, by Courtney and Beaumont (1983), Zhong (1997) and Watts and Zhong (2000). This model is based on laboratory studies of thermal creep and observations of seafloor bathymetry corresponding to a cooling plate model. It can adequately explain the dependency of  $T_c$  on load and thermal age of the lithosphere. The multilayered visco-elastic model shows the elastic and visco-elastic plate models as end-member cases of the flexural loading. The success of the elastic plate model is ascribed to the viscosity

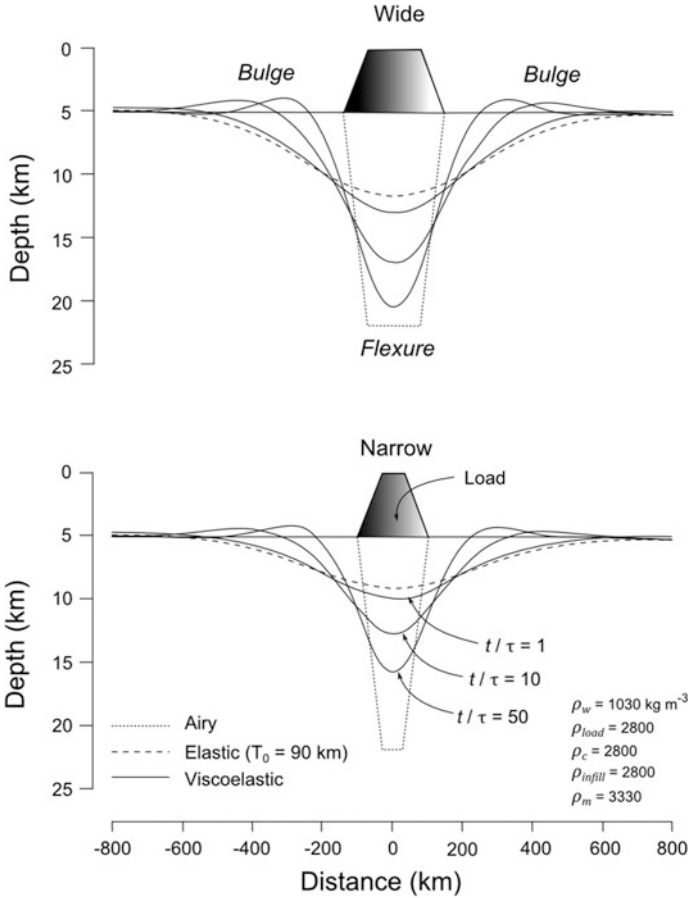


**Fig. 1.5** Flexure of a thin visco-elastic plate over an inviscid substratum by **a** a wide and **b** a narrow two-dimensional surface load (modified from Watts 2001)

of the uppermost oceanic lithosphere, which is so high that it essentially behaves as an elastic layer in geologic timescales.

## 1.2 Estimation of Elastic Thickness

There are a number of methods to estimate  $T_e$  of a thin elastic plate. Their choice depends on the available data, which includes free air and Bouguer gravity anomaly, bathymetry/topography, and seismic data. Most of the methods are focused on estimating the flexural rigidity,  $D$ , from which  $T_e$  can be easily calculated. The different techniques can be used both for forward modeling of the gravity

data from topography, and inverse modeling of the state of isostasy, done directly from topography and gravity. Customarily, the mathematical operations are performed in the wave-number domain by using Fourier transform, although the line-integral technique can be used as well (e.g., Talwani et al. 1959). The methods are mostly used in 2D, but can be extended into 3D by defining the wave-vector as  $k = (k_x^2 + k_y^2)^{1/2}$ .

If seismic data is available, and the surface of flexure can be observed (e.g., Watts and ten Brinks 1989), the deformation can be directly computed. Using bathymetry data, a flexural response function [ $\Phi_e(k)$  of Walcott (1976) and Watts (2001)] can be used to estimate  $D$ , from which  $T_e$  can be calculated using Eq. 1.4. The flexure of an elastic plate under load is given by Eq. 1.7, or by the equation  $y = (\rho_c - \rho_w)h \cos(kx)/(\rho_m - \rho_{infill}) \cdot \Phi_e(k)$ , which is the same as Eq. 1.7, using  $\rho_l = \rho_c$ , the density of the crust. The flexural response function,  $\Phi_e(k)$ , is given by:

$$\Phi_e(k) = \{1 + Dk^4/(\rho_m - \rho_{infill})g\}^{-1}. \tag{1.9}$$

Equation 1.7 gives the flexural response at a single point for a particular  $k$ . For a 2D load of arbitrary shape, both the flexure  $y$  and topographic component  $h\cos(kx)$  are replaced by their discrete Fourier transform  $Y(k)$  and  $H(k)$  in the wave-number domain, so that the equation is reduced to:

$$Y(k) = (\rho_c - \rho_w)/(\rho_m - \rho_{infill}) \cdot H(k) \Phi_e(k). \tag{1.10}$$

The equation can be solved for  $Y(k)$ , using different values of  $D$ . The flexure  $y$  can be obtained from  $Y(k)$  by an inverse Fourier transform. Convolution of  $h$  and an inverse transform function of  $\Phi_e(k)$ , which is an impulse function, can also be used to get  $y$  directly in the spatial domain (Watts 2001; Fig. 1.6). Knowing the bathymetry and the flexure, the value of  $D$  that gives best fit to the observation is taken, and  $T_e$  is calculated using Eq. 1.4.

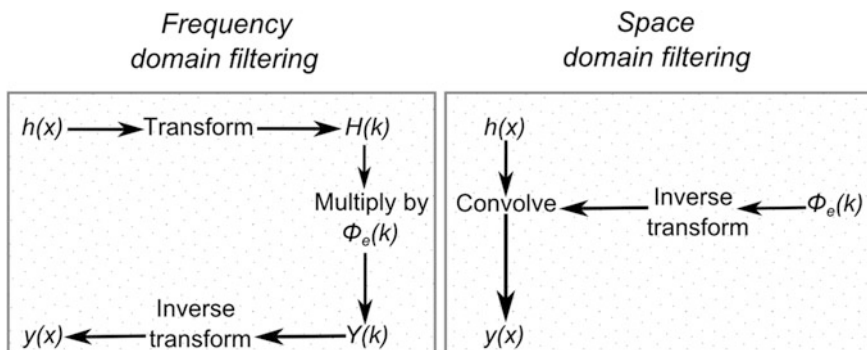


**Fig. 1.6** Schematic workflow in frequency (wave-number) and spatial domain filtering of a topographic data set (modified from Watts 2001)

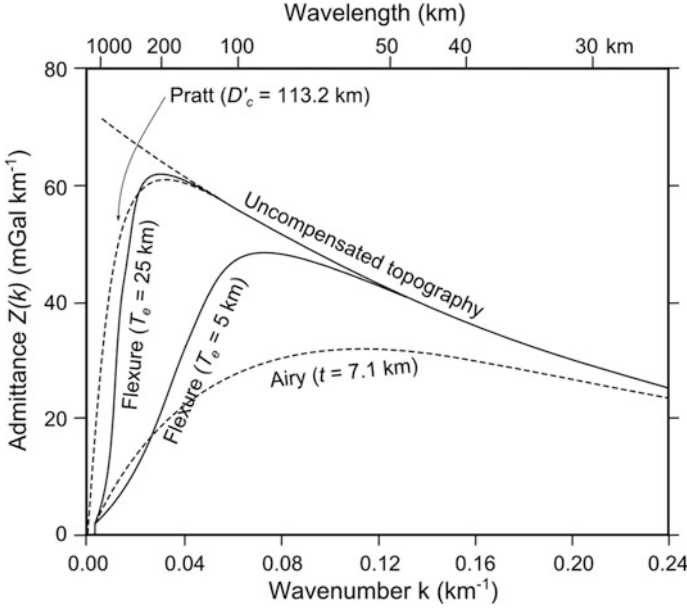


**Fig. 1.7** Gravitational admittance for uncompensated topography, Airy, Pratt, and flexural isostasy (modified from Watts 2001)

With bathymetry and free air gravity anomaly data, the gravitational admittance can be used to estimate  $T_e$  from  $D$  for an elastic plate (e.g., Banks et al. 1977). The gravitational admittance,  $Z(k)$ , is the transfer function that modifies the topography to produce the gravity anomaly, and is given by:

$$Z(k) = \Delta g(k)/H(k) \quad (1.11)$$

where  $\Delta g(k)$  is the discrete Fourier transform of the gravity anomaly in the wave-number domain.

As gravity anomaly is dependent on the isostatic response of the load, the gravitational admittance,  $Z(k)$ , contains the information on isostasy. It can be either estimated from the gravity anomaly itself, to test the bathymetry, or calculated for different models of isostasy from bathymetry, to predict the gravity (Fig. 1.7). For flexural isostasy of an elastic plate, the free air gravity admittance is given by Watts (2001):

$$Z(k)_{\text{flex}} = 2\pi G(\rho_1 - \rho_w)e^{-kd} \left\{ 1 - \frac{\phi_c(k) \left( (\rho_2 - \rho_{\text{infill}}) + (\rho_3 - \rho_2)e^{-kt_2} + (\rho_m - \rho_3)e^{-k(t_2+t_3)} \right)}{(\rho_m - \rho_{\text{infill}})} \right\} \quad (1.12)$$

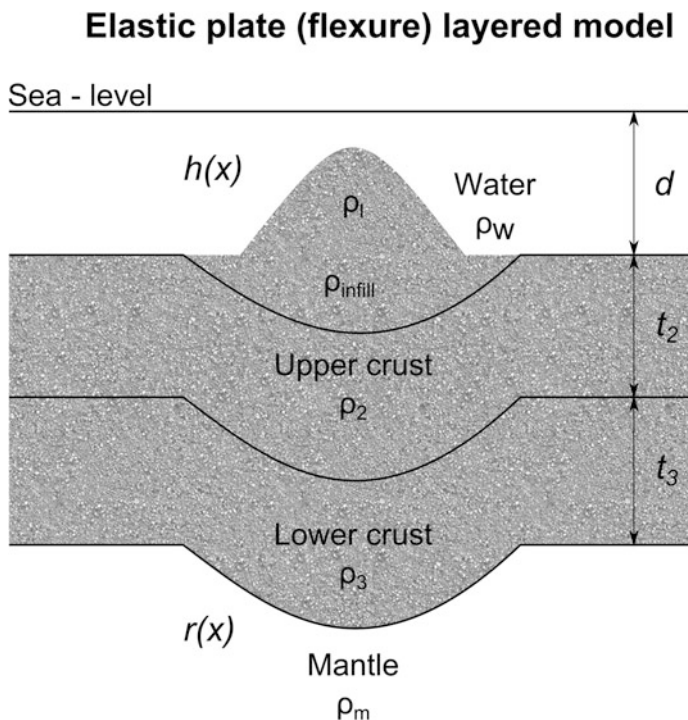


**Fig. 1.8** Parameters for the flexural model of isostatic compensation for an elastic plate (modified from Watts 2001)

where  $G$  is the gravitational constant,  $d$  is the mean water depth,  $\rho_2$  and  $\rho_3$  are the densities of the upper and lower crustal layers, and  $t_2$  and  $t_3$  are the thickness of same layers (Fig. 1.8).

Equations 1.11 and 1.12 and an inverse Fourier transform are usually used to get the gravity anomaly from the bathymetry, which is then matched with the observed anomaly. The best fit result is used to get  $T_e$ . However,  $T_e$  may also be computed from the observed gravity anomaly by the inverse transfer function,  $Z^{-1}(k)$  ( $=H(k)/\Delta g(k)$ ), and matched with the bathymetry, as shown by various authors (e.g., Dixon et al. 1983; Watts et al. 1985; Goodwillie and Watts 1993; Smith and Sandwell 1994; Lyons et al. 2000).

Transformation of spatial data into wave-number domain results in noise, which can be reduced by cross-spectral techniques. A better estimation of  $Z(k)$  may be obtained by dividing the cross-spectrum of the input and output with the power spectrum of the input (Munk and Cartwright 1966). Watts (1978) gives the admittance in this case as:

$$Z(k) = \Delta g(k)H^*(k)/H(k)H^*(k) \quad (1.13)$$

where the asterisk (\*) denotes complex conjugate.

A spectral smoothening is required to reduce noise in the data obtained from the ship track. McKenzie and Bowin (1976) have used this method to estimate the admittance after smoothening by subdividing long ship track profiles into a number of smaller, same length profiles. Their admittance is given by:

$$Z(k) = C_c(k)/E_t(k) \quad (1.14)$$

where  $C_c(k)$  is the cross-spectrum of the gravity anomaly and topography, and  $E_t(k)$  is the power spectrum of the bathymetry. They are given as (McKenzie and Bowin 1976; Watts 1978):

$$C_c(k) = \frac{1}{N} \sum_{m=1}^N \Delta g_m(k)H_m^*(k) \quad (1.15)$$

and

$$E_t(k) = \frac{1}{N} \sum_{m=1}^N H_m(k)H_m^*(k) \quad (1.16)$$

where N is either the number of along track segments (McKenzie and Bowin 1976), or the number of profiles of the same geological feature (Watts 1978).

Two parameters, coherence and phase of the admittance, are useful in estimating the admittance (McKenzie and Bowin 1976; Watts 1978).

The coherence,  $\gamma^2(k)$ , is given by:

$$\gamma^2(k) = C_c(k)C_c^*(k)/E_{\Delta g}(k)E_t(k) \quad (1.17)$$

where

$$E_{\Delta g}(k) = \frac{1}{N} \sum_{m=1}^N \Delta g_m(k)\Delta g_m^*(k) \quad (1.18)$$

represents the power spectrum of gravity, and the phase of the admittance,  $\phi_z$ , is given by:

$$e^{-i2\phi_z(k)} = Z(k)/Z^*(k). \quad (1.19)$$

In the case of noisy data, a better estimate of coherence than that from Eq. 1.17 is given by Munk and Cartwright (1966):

$$\gamma_0^2(k) = (N\gamma^2(k) - 1)/(N - 1). \quad (1.20)$$

The coherence is a measure of the gravity field caused by the topography alone, without the effects of isostasy or water depth. Thus, for small wavelengths, the coherence will be small due to suppression of the topographic gravity effects by the water depth, while for long wavelengths, isostatic response masks the gravity due to topography. The phase of admittance checks for the real part of the complex admittance calculated. For wavelengths where coherency is high, the phase should be close to zero for the admittance to be real (Fig. 1.9). The admittance calculated by spectral techniques is independent of the isostatic response of the load, and can be used to identify the compensation mechanism in regions of interest (Watts 2001).

In the *continents*, the gravitational admittance is calculated from the Bouguer anomaly gravity data. That data is already corrected for the topography, representing the density distribution within the crust only. Furthermore, they are reduced to geoid, which makes calculations easier. For surface loading of an elastic plate, the Bouguer gravity admittance is given by Watts (2001):

$$Z(k)_{\text{surface}} = -2\pi G\rho_c e^{-kZ_t} \Phi'_e(k) \quad (1.21)$$

where  $\Phi'_e(k) = \{1 + Dk^4/(\rho_m - \rho_c)g\}^{-1}$ , being similar to Eq. 1.9 with  $\rho_{\text{infill}} = \rho_c$ .

For buried loads one could use (Watts 2001):

$$Z(k)_{\text{buried}} = 2\pi G(\rho_m - \rho_c) [e^{-kZ_t} - \{e^{-kZ_L} \cdot (Dk^4 + \rho_m g)/(\rho_m - \rho_c)g\}] \quad (1.22)$$

where  $Z_t$  and  $Z_L$  are the mean thickness of the crust and upward acting force, the buried load, below the mean sea level, respectively (Figs. 1.10 and 1.11).

Forsyth (1985) had given an expression of Bouguer admittance for combined surface and buried loading.

$$Z(k)_{\text{surface + buried}} = -2\pi G\rho_c e^{-kZ_t} \left\{ \frac{\frac{H_b^2}{\Phi_e''(k)} + H_t^2 \Phi_e(k)}{H_b^2 + H_t^2} \right\} \quad (1.23)$$

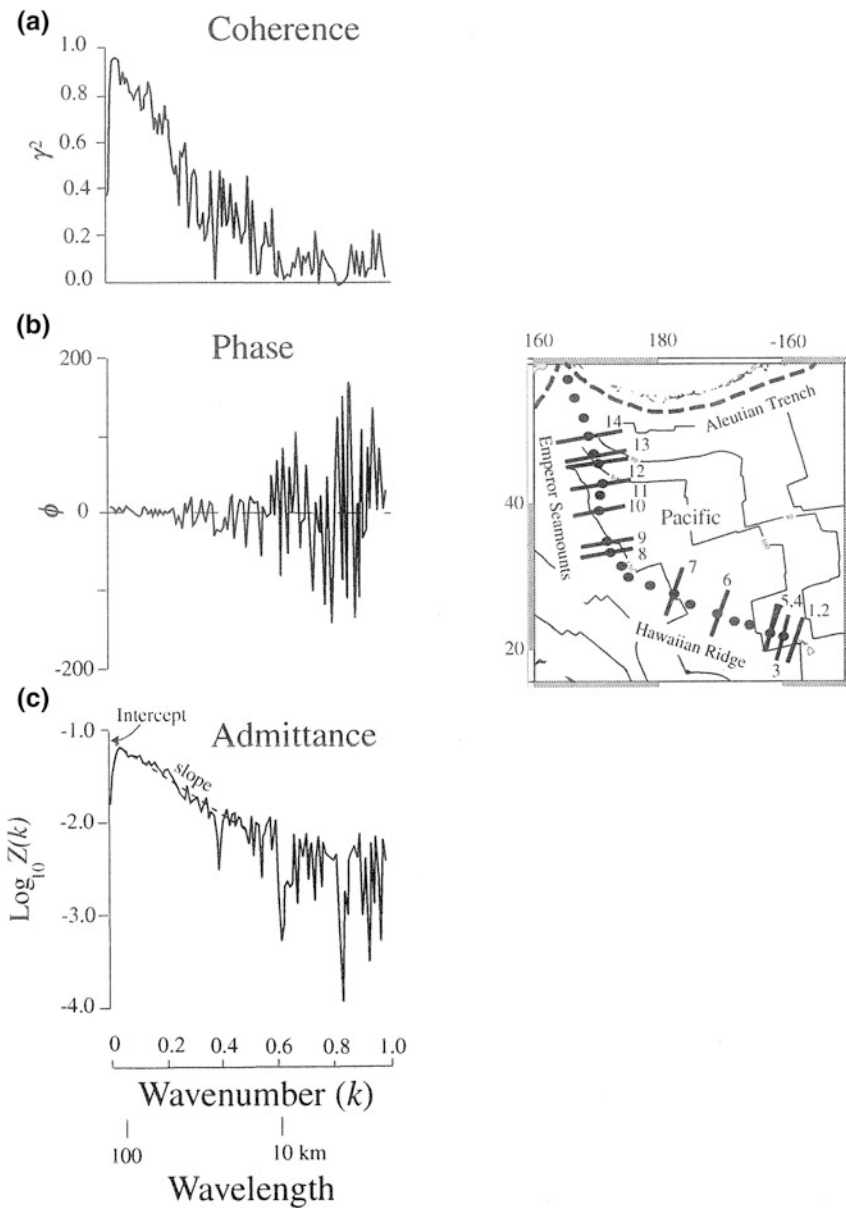
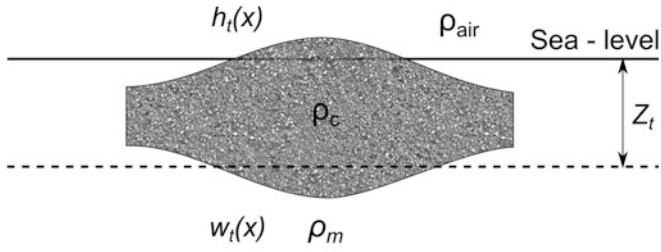


**Fig. 1.9** The **a** coherence, **b** phase, and **c** admittance determined from spectral analysis of bathymetry and free-air gravity anomaly along the Hawaiian-Emperor seamount chain (Watts 1978, 2001)

**(a) Surface loading**



**(b) Buried loading**

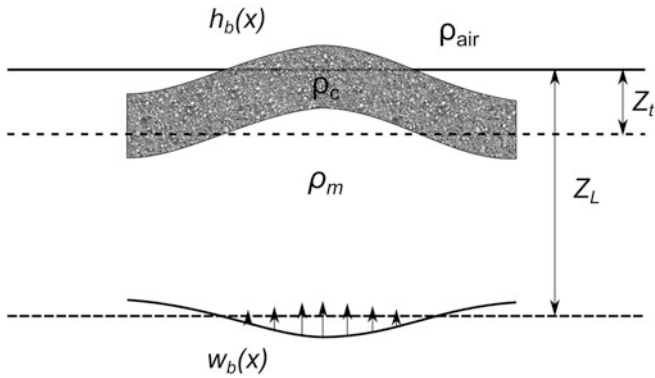


**Fig. 1.10** Parameters for the calculation of the Bouguer admittance for surface loading and buried loading of continents (modified from Watts 2001)

where  $H_b$  and  $H_t$  are the contribution of the buried and surface load to the observed topography, respectively,  $H = H_b + H_t$ , and  $\Phi_e'''(k) = \{1 + Dk^4/(\rho_m g)\}^{-1}$  (Watts 2001).

$H_b$  and  $H_t$  are related to the loading ratio  $f_l$ :

$$f_l = |H_b|(\rho_m - \rho_c)/\Phi_e'(k)\rho_c H_t. \tag{1.24}$$

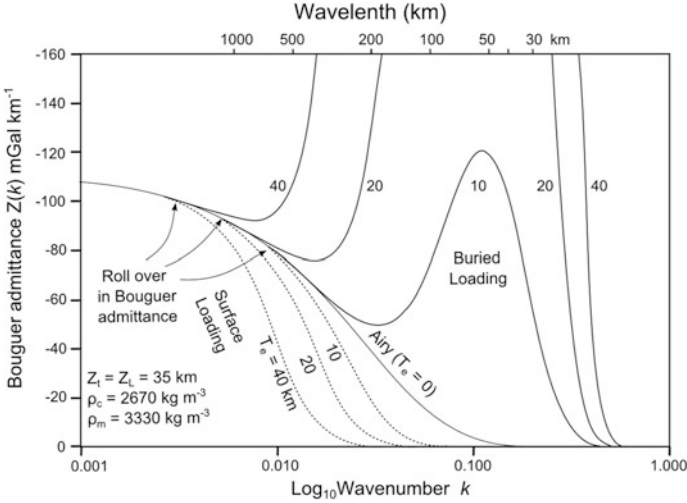


**Fig. 1.11** Bouguer gravitational admittance for the surface and buried loading models (modified from Watts 2001)

The coherence,  $\gamma^2$ , is given by:

$$\gamma^2 = \langle H_t W_t + H_b W_b \rangle^2 / \langle H_t^2 + H_b^2 \rangle \langle W_t^2 + W_b^2 \rangle \quad (1.25)$$

where  $\langle \rangle$  indicates spectral averaging,  $W_b$  and  $W_t$  are the contributions of the buried and surface loads to the observed flexure at the base of the crust respectively, and  $W = W_b + W_t$ .

Bouguer admittance and coherence plots for the continents are shown in Figs. 1.12 and 1.13 respectively. Note the pronounced roll-over in Bouguer admittance plot that points to a dominant surface loading in the continental cases. It is to be observed in the coherence plots that continent-wide coherences do not fit well with calculated values, while those of the sub-regions do. The reason for this may be that the continents are a composite of tectonically distinct sub regions, each one of which having a different rigidity.

A new approach for estimating the flexural rigidity,  $D$ , is the convolution method of Braitenberg et al. (2002). In this method, the calculations are done in the spatial domain by convolving the topography grid with the flexural response of a point load, using an impulse function.

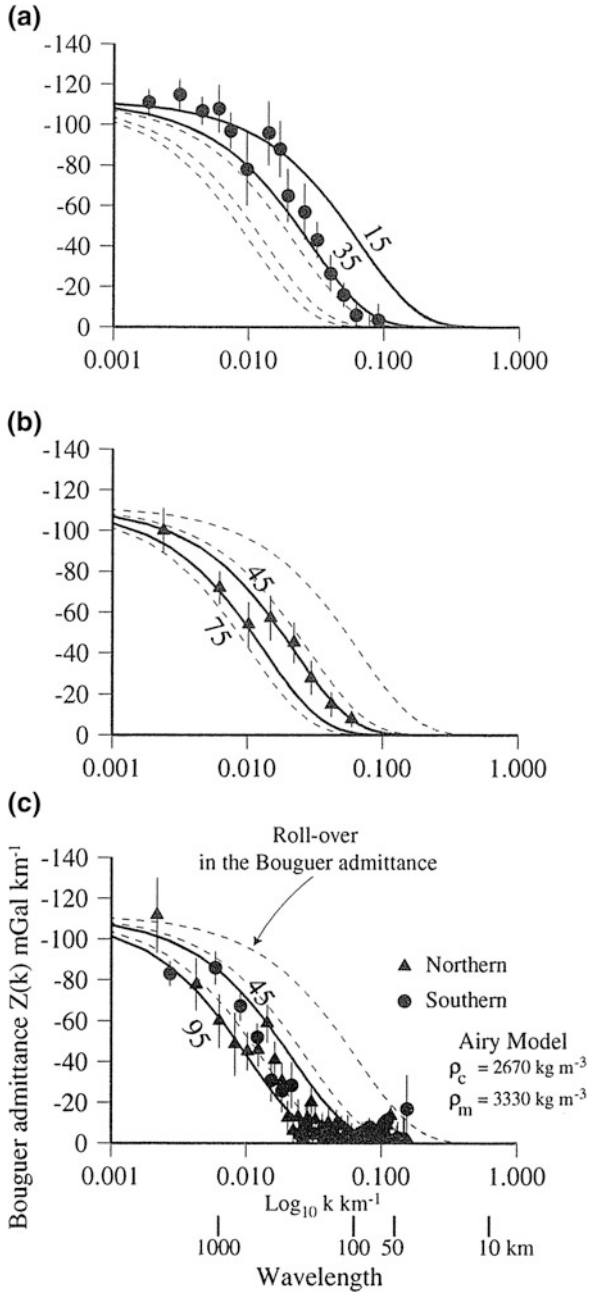


**Fig. 1.12** Comparison of observed and calculated Bouguer gravitational admittance for **a** North America, **b** Australia, and **c** Africa (Watts 2001)

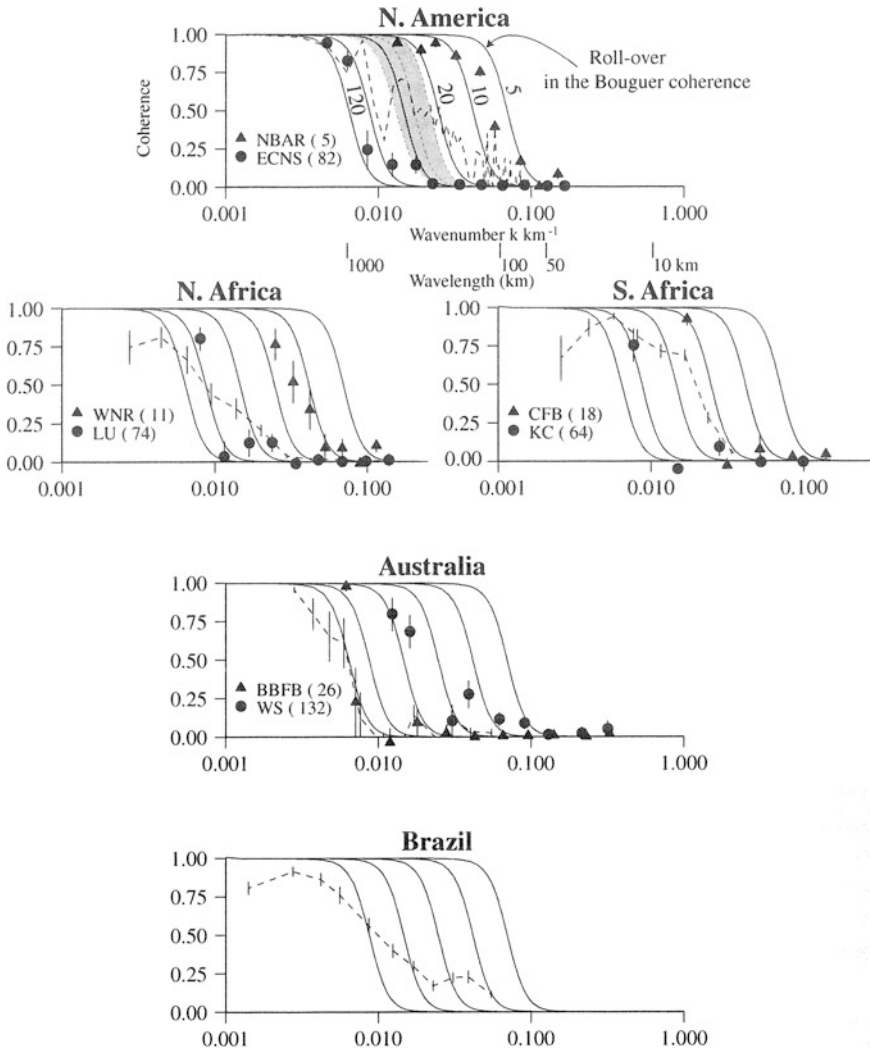


**Fig. 1.13** Comparison of observed and calculated Bouguer coherences for North America, Africa, Australia and Brazil (Watts 2001)

## References

- Banks RJ, Parker RL, Huestis SP (1977) Isostatic compensation on a continental scale: local versus regional mechanism. *Geophys J R Astron Soc* 51:431–452
- Braitenberg C, Ebbing J, Götze H-J (2002) Inverse modeling of elastic thickness by convolution method—the eastern Alps as a case example. *Earth Planet Sci Lett* 202:387–404
- Caldwell JG, Turcotte DL (1979) Dependence of the elastic thickness of the oceanic lithosphere on age. *J Geophys Res* 84:7572–7576

- Cazenave A, Lago B, Dominh K, Lambeck K (1980) On the response of the ocean lithosphere to seamount loads from Geos 3 satellite radar altimeter observations. *Geophys J R Astron Soc* 63:233–252
- Courtney RC, Beaumont C (1983) Thermally-activated creep and flexure of the oceanic lithosphere. *Nature* 305:201–204
- Dixon TH, Naraghi M, McNutt MK, Smith SM (1983) Bathymetric prediction from Seasat altimeter data. *J Geophys Res* 88:1563–1571
- Forsyth DW (1985) Subsurface loading and estimates of the flexural rigidity of continental lithosphere. *J Geophys Res* 90:12623–12632
- Goodwillie AM, Watts AB (1993) An altimetric and bathymetric study of elastic thickness in the central Pacific Ocean. *Earth Planet Sci Lett* 118:311–326
- Gunn R (1943) A quantitative evaluation of the influence of the lithosphere on the anomalies of gravity. *Franklin Inst J* 236:47–65
- Lambeck K, Nakiboglu SM (1981) Seamount loading and stress in the ocean lithosphere, 2. Viscoelastic and elastic-viscoelastic models. *J Geophys Res* 86:6961–6984
- Lyons SN, Sandwell DT, Smith WHF (2000) Three-dimensional estimation of elastic thickness under the Louisville Ridge. *J Geophys Res* 105:13239–13252
- McKenzie DP, Bowin CO (1976) The relationship between bathymetry and gravity in the Atlantic Ocean. *J Geophys Res* 81:1903–1915
- McNutt MK, Parker RL (1978) Isostasy in Australia and the evolution of the compensation mechanism. *Science* 199:773–775
- Munk WH, Cartwright DE (1966) Tidal spectroscopy and prediction. *J Geophys Res* 259:533–581
- Nadai A (1963) Theory of flow and fracture of solids, vol 2. McGraw-Hill, New York
- Quinlan GM, Beaumont C (1984) Appalachian thrusting, lithospheric flexure and the Paleozoic stratigraphy of the eastern Interior of North America. *Can J Earth Sci* 21:973–996
- Sleep NH, Snell NS (1976) Thermal contraction and flexure of mid-continent and Atlantic marginal basins. *Geophys J R Astron Soc* 45:125–154
- Smith WHF, Sandwell DT (1994) Elastic lithosphere thickness estimated from dense satellite altimetry and sparse shipboard bathymetry. *Suppl EOS Trans Am Geophys Union* 75(44):154
- Talwani M, Worzel JL, Landisman M (1959) Rapid gravity computations for two-dimensional bodies with applications to the Mendocino submarine fracture zone. *J Geophys Res* 54:49–59
- Walcott RI (1970) Flexural rigidity and viscosity of the lithosphere. *J Geophys Res* 75:3941–3953
- Walcott RI (1976) Lithospheric flexure, analysis of gravity anomalies, and the propagation of seamount chains. In: Sutton GH, Manghnani MH, Moberly R (eds) *The geophysics of the Pacific Ocean basin and its margins*. *Geophys Monogr Ser* 19. Am Geophys Union, Washington, pp 431–438
- Watts AB (1978) An analysis of isostasy in the world's oceans: 1. Hawaiian-Emperor seamount chain. *J Geophys Res* 83:5989–6004
- Watts AB (1983) The strength of the Earth's crust. *Marine Tech Soc J* 17: 12–17
- Watts AB (2001) *Isostasy and flexure of the lithosphere*. Cambridge University Press, New York, p 458
- Watts AB, ten Brink US (1989) Crustal structure, flexure and subsidence history of the Hawaiian Islands. *J Geophys Res* 94:10473–10500
- Watts AB, Zhong S (2000) Observations of flexure and the rheology of oceanic lithosphere. *Geophys J Int* 142:855–875
- Watts AB, Cochran JR, Patriat P, Doucoure M (1985) A bathymetry and altimetry profile of the Southwest Indian Ridge at 31°S. *Earth Planet Sci Lett* 73:129–139
- Zhong S (1997) Dynamics of crustal compensation and its influences on crustal isostasy. *J Geophys Res* 102(B7):15287–15299

# Chapter 2

## Plumes and Hotspots

### 2.1 Introduction

The plate tectonic processes adequately explain two principal types of basaltic volcanism on the earth's surface, the mid-oceanic ridge and island arc volcanism. Apart from these, another important type of basaltic volcanism occurs away from the plate margins. The most volumetric forms of this type are the continental flood basalts, oceanic plateaus and aseismic ridges, collectively referred as large igneous provinces. These are explained by the plume hypothesis, initially put forward by Wilson (1963) and Morgan (1971, 1972) to explain the age-progressive chains of volcanic islands like Hawaii that stretch across the ocean basins. The plume hypothesis attributes flood basalts and giant oceanic plateaus to the melting of the head of a plume (Richards et al. 1989; Campbell and Griffiths 1990) and aseismic ridges to the melting of a plume tail (Wilson 1963; Morgan 1971).

A mantle plume is a buoyant upwelling of abnormally hot rock within the Earth's mantle. As the plume rises to shallow depths below the lithosphere, the head may melt partially to give rise to volcanic provinces. Hotspots are observed surface features on the crust characterized by excess volcanisms that are thought to be fed by the underlying anomalously hot mantle.

Mantle plumes are interpreted to be the cause of many or most of the hotspots. However, in recent literature the terms are often used interchangeably. Thus, Anderson and Natland (2005) wrote “*Unfortunately, the terms hotspot and plume have become confused. In recent literature the terms are used interchangeably. A plume is a hypothetical mantle feature. A hotspot is a region of magmatism or elevation that has been deemed to be anomalous in some respect because of its volume or location. In the plume hypothesis, a hotspot is the surface manifestation of a plume, but the concepts are different; one is the presumed effect, and the other is the cause.*”

## 2.2 The Plume Hypothesis

Fluid flow from thermal boundary layers occurs due to buoyancy, as a direct result of density differences due to temperature between materials on either side of the layer. The earth interior has two such thermal boundary layers—the crust-mantle boundary, where heat is transferred by conduction, and the lower mantle-outer core boundary, where heat conduction takes place by convecting plumes of hot material rising from the liquid outer core.

Laboratory experiments (e.g., Griffiths and Campbell 1990) suggest that Rayleigh-Taylor instability occurring in the D'' layer in outer core leads to the formation of upwellings that are focused into narrow conduits, which rise through the mantle, driven by their thermal buoyancy. These plume materials are hotter than the surrounding mantle by about 100–300 °C (Campbell and Davies 2006), indicating two orders of lower viscosity, and hence are lighter. However, to gain

**Fig. 2.1** Photograph of a laboratory model of a starting thermal plume showing the structure caused by heat conduction and consequent entrainment of surrounding fluid (Campbell and Griffiths 1990). The dark area is hot material from the plume source and the lighter material is cooler entrained material

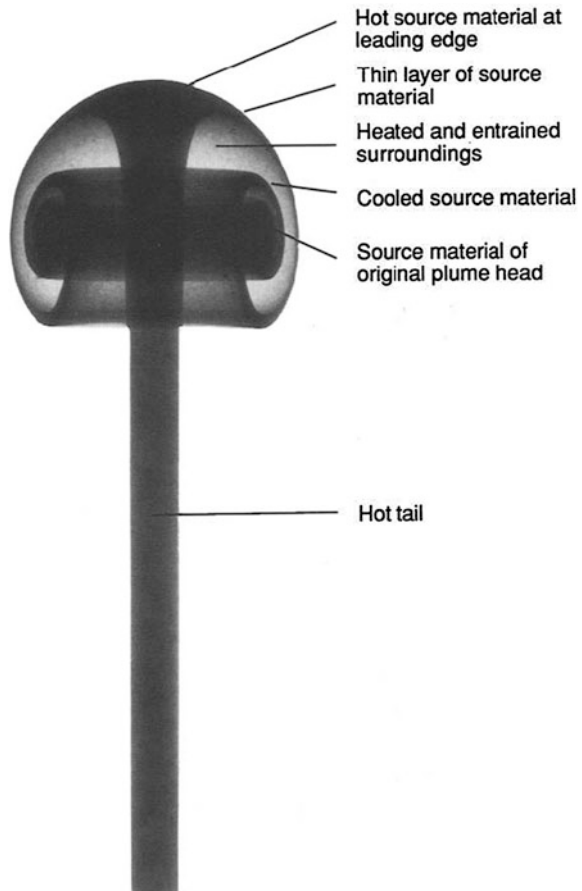
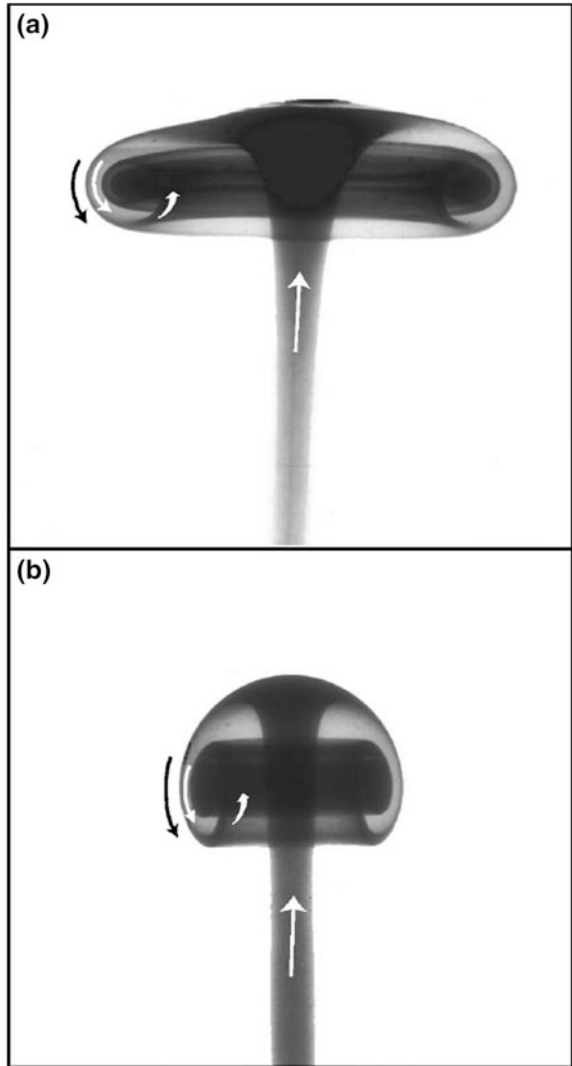


**Fig. 2.2** Photograph of a laboratory model of a starting thermal plume (a) *mid-way* through its ascent and (b) at the *top* of its ascent (Campbell and Davies 2006). The *white arrows* show motion within the plume and the *black arrows* the direction of motion in the boundary layer adjacent to the plume



sufficient buoyancy, a large amount of material needs to accumulate, connected by a relatively narrow tail or feeder conduit, which connects the plume head with the reservoir. The tail is hotter and less viscous than the head, which cools by heat exchange with the surrounding, entraining partial melt from the mantle during its ascent (Figs. 2.1 and 2.2). As the plume rises through the mantle, the head grows by entrainment and a constant flux of materials by the tail (Griffith and Campbell 1990), which ascends faster. When a stagnation point is reached, material flows radially with a spiraling motion, giving the head a characteristic mushroom shape.

Numerical and analogue modelings suggest that the plume shape and mobility is controlled by the magnitude of the viscosity contrast with the surrounding mantle (Kellogg and King 1997; Lowman et al. 2004; Lin and van Keken 2006). As the contrast increases, the plume conduit becomes narrower and the head becomes broader, mushroom shaped, allowing the plume to rise more efficiently through the mantle. Nevertheless, a great variety of shapes are also possible if the density contrasts due to chemical variations are taken into account (Farnetani and Samuel 2005; Lin and van Keken 2006).

### 2.3 Characteristics of Plumes

The plumes can be characterized as follows (Campbell 2006, 2007; Campbell and Davies 2006):

1. New plumes consist of a large head followed by a narrow tail. Laboratory experiments on thermal plumes (e.g., Griffiths and Campbell 1990) suggest that the shape is controlled by the viscosity contrast between the plume material and the surrounding mantle. Flood basalts/oceanic plateaus and hotspots tracks are considered the eruptive products from the plume head and tail, respectively.
2. Plumes originate from a thermal boundary layer, probably the core-mantle boundary. Most of the plumes are supposed to originate from the D'' layer in the lower mantle. However, using seismic methods to trace plume tails to their origin is difficult because of their small diameter, and the method had met with little success.
3. Flattened plume heads should be 2000–2500 km in diameter at the base of the lithosphere, while the narrow tails have a diameter of 100–200 km in the upper mantle. The plume-head diameter depends on the thermal anomaly of the plume with the adjacent mantle, its buoyancy flux, kinematic viscosity of the lower mantle, and the height of ascent from the origin, with the last one being the most important factor.
4. Plume heads stalled at the base of the lithosphere should be seismically detectable for ca. 100 my, and remain hot for about 300 my. It depends on the rate of heat conduction by the lithosphere, which itself is a slow process. This explains the low heatflow anomaly near some hotspots, as in Hawaii. As the plume loses heat, it cools down, and depending upon its thickness, the thermal anomaly disappears within 300 my, as predicted in the case of the Ontong-Java plateau.
5. The temperature excess of a plume head is predicted to be  $\sim 300$  °C at the centre of the head and to taper to  $\sim 100$  °C towards its margins. These temperature anomalies are predicted based on anomalous crustal thicknesses produced by the plume (McKenzie and Bickle 1988). The highest temperature in the centre is due to the rising tail connecting the head with the mantle reservoir. At the margins, the plume entrains mantle material and becomes cooler.

6. Plume heads can erupt millions of cubic kilometres of magma. The melting rate of a mantle plume depends on the depth of emplacement of the hot plume head at the base of the lithosphere, and the presence of recycled oceanic crusts in the form of eclogite in the plume source. Modelling indicates a melting rate of 1–10 km<sup>3</sup>/a, and a total melt volume of 1–20 million km<sup>3</sup>, depending on the assumed conditions (Leitch and Davies 2001). These results cover the range of observed values for most of the large igneous provinces.
7. Rifting over a plume head produces a narrow zone of thickened oceanic crust, typically 100–200 km wide. As long as lithospheric extension pulls up the hot plume material towards the rift, anomalous melting and crustal thickening continues. The 150–200 km thick plume head is completely pulled up after only 150–200 km of extension, limiting the anomalous crust to a narrow zone at the centre of the newly formed ocean basin.
8. Both plume heads and tails erupt high temperature picrites. The temperature of erupted magmas are estimated from their MgO content, which shows a linear relationship of 4 wt% increase in MgO with 100 °C rise in magma temperature. The maximum MgO content of plume-derived picrite from Reunion-Deccan, Iceland-North Atlantic province, Hawaii, Siberian Traps, Emeishan, etc. ranges from 18 to 22 wt%, indicating a thermal anomaly of 150–250 °C for both the plume head and the tail.
9. Picrites erupt early during flood volcanism and are most abundant near the centre of the plume head and less abundant towards its margins. This occurs because only the hottest materials in the centre of the plume head ascends to shallow levels, and undergo adiabatic decompression melting to produce picritic lava, which decreases towards the periphery. These picritic flows are often covered by later lava, and are rarely seen in flood basalt provinces. However, they have been documented for the Parana-Etendeka, Deccan, Emeishan, North Atlantic, Siberian Traps and Karoo.
10. Flood basalt volcanism is preceded by a domal uplift of 500–1000 m due to arrival of the plume head in the upper mantle. The uplift is caused by the impact of the plume head, buoyancy due to ponding of the plume materials at the base of the lithosphere, thermal and magmatic underplating. The best documented example of domal uplift occurs in the Emeishan flood basalt province in south-west China (He et al. 2003), where the timing of the uplift is documented to begin 3–5 my before volcanism.
11. The position of hot-spots produced over plumes is fixed with respect to the mantle. The lower mantle has an average viscosity about 30 times higher than that of the upper mantle, indicating a ten times slower convective velocity. This slow convective motion fixes the lower mantle plumes within the upper mantle, so that they move ten times slower than the plates. This makes the plume effectively stationary with respect to the lithospheric plates, so that the hotspot track follows the direction of the plate motions.

## 2.4 Classification of Plumes

Increasing research focused on the evolution of hotspot magmatism led to the development of a number of ideas for their genesis, apart from variations in the mantle plume hypothesis itself. Turcotte and Oxburgh (1973) proposed tensional cracking of the lithosphere and subsequent volcanism to explain the age progressive chains of volcanism. Morgan (1978) had proposed a different type of hotspot island apart from those produced by plumes. More recent studies (Sleep 1990, 2002; Clouard and Bonneville 2001) have debated with the ideas of primary versus secondary hotspots, as discussed later. Anderson (1998, 2000) have rejected the plume hypothesis altogether, explaining the presence of mid-plate volcanism by plate movement-induced stresses fracturing the lithosphere and edge-driven convection in the upper mantle by localized thermal perturbations. Similar views have also been mentioned by Ballmer et al. (2007). The presence of such diverse views led Courlliot et al. (2003) to attempt a classification of the surface hotspots in terms of their originating plumes, based on criteria that look for deep-seated mantle sources:

1. the presence of a linear chain of volcanoes with continuous age progression, indicating a long-lived plume source;
2. a flood basalt at the origin of the track, corresponding to the impingement of the plume head below the lithosphere;
3. a buoyancy flux of greater than  $10^3 \text{ kg s}^{-1}$ , for generating a topographic anomaly
4. a consistently high  $^4\text{He}/^3\text{He}$  or  $^{21}\text{Ne}/^{22}\text{Ne}$  ratio, indicating a deep-seated, primitive mantle reservoir; and
5. a significantly low shear wave velocity in the underlying mantle, indicating the presence of hot, partially melted material below the hotspots.

Applying these criteria to a selection of hotspots (Table 2.1) that were active in the last one million years (Davies 1988; Sleep 1990; Steinberger 2000) led to a threefold classification of their possible sources (Courlliot et al. 2003; Fig. 2.3):

1. Seven hotspots, including Hawaii, Easter, Louisville, Iceland, Afar, Reunion and Tristan, satisfy all five criteria. They were possibly originated by plumes from the lower mantle, due to chemical heterogeneity and instability in the D'' layer (Olson et al. 1987; Bercovici and Kelly 1997), termed "Morganian" by Courlliot et al. (2003). They can also be called as primary plumes.
2. About twenty hotspots may be associated with plumes from the bottom of the transition zone, at the top of large domes that correspond to the superswells, also known as superplumes (Courlliot et al. 2003). Examples include Caroline, McDonald, Pitcairn, Samoa and Tahiti. These can be called as secondary plumes.
3. The remainder of about twenty hotspots could originate from thermal perturbations in the upper mantle. They are called as "Andersonian" by Courlliot et al. (2003), also known as tertiary plumes. These hotspots may be linked to

**Table 2.1** Main characteristics of selected hotspots (Courtillot et al. 2003)

Scores for 49 hotspots with respect to five criteria used to diagnose a potentially deep origin										
Hotspot	Lat	Lon (°E)	Track	Flood/plateau	Age (Ma)	Buoy.	Reliab.	<sup>3</sup> He/ <sup>4</sup> He	Tomo (500)	Count
<b>Afar</b>	<b>10N</b>	<b>43</b>	<b>No</b>	<b>Ethiopia</b>	<b>30</b>	<b>1</b>	<b>Good</b>	<b>High</b>	<b>Slow</b>	<b>4</b>
Ascension	8S	346	No	No	-	NA	NA	NA	0	0+?
Australia E	38S	143	Yes	No	-	0.9	Fair	NA	0	1+?
Azores	39N	332	No?	No	-	1.1	Fair	High?	0	1+?
Baja/Guadalupe	27N	247	Yes?	No	-	0.3	Poor	Low	0	0+?
Balleny	67S	163	No	No	-	NA	NA	NA	0	0+?
Bermuda	33N	293	No	No?	-	1.1	Good	NA	0	0+?
Bouvet	54S	2	No	No	-	0.4	Fair	High	0	1+?
<b>Bowie</b>	<b>53N</b>	<b>225</b>	<b>Yes</b>	<b>No</b>	-	<b>0.3</b>	<b>Poor</b>	<b>NA</b>	<b>slow</b>	<b>2+?</b>
Cameroon	4N	9	Yes?	No	-	NA	NA	NA	0	0+?
Canary	28N	340	No	No	-	1	Fair	Low	Slow	2
Cape Verde	14N	340	No	No	-	1.6	Poor	High	0	2
<b>Caroline</b>	<b>5N</b>	<b>164</b>	<b>Yes</b>	<b>No</b>	-	<b>2</b>	<b>Poor</b>	<b>High</b>	<b>0</b>	<b>3</b>
Comores	12S	43	No	No	-	NA	NA	NA	0	0+?
Crozet/Pr. Edward	45S	50	Yes?	Karoo?	183	0.5	Good	NA	0	0+?
Darfur	13N	24	Yes?	No	-	NA	Poor	NA	0	0+?
Discovery	42S	0	No?	No	-	0.5	Poor	High	0	1+?
<b>Easter</b>	<b>27S</b>	<b>250</b>	<b>Yes</b>	<b>mid-Pac mnt?</b>	<b>100?</b>	<b>3</b>	<b>Fair</b>	<b>High</b>	<b>Slow</b>	<b>4+?</b>
Eifel	50N	7	Yes?	No	-	NA	NA	NA	0	0+?
Fernando	4S	328	Yes?	CAMP?	201?	0.5	Poor	NA	0	0+?
<b>Galapagos</b>	<b>0</b>	<b>268</b>	<b>Yes?</b>	<b>Caribbean?</b>	<b>90</b>	<b>1</b>	<b>Fair</b>	<b>High</b>	<b>0</b>	<b>2+?</b>
Great Meteor/New England	28N	328	Yes?	No?	-	0.5	Poor	NA	0	0+?

(continued)

Table 2.1 (continued)

Hotspot	Lat	Lon (°E)	Track	Flood/plateau	Age (Ma)	Buoy.	Reliab.	$^3\text{He}/^4\text{He}$	Tomo (500)	Count
<i>Hawaii</i>	20N	204	Yes	<i>Subducted?</i>	>80?	8.7	Good	High	Slow	4+?
Hoggar	23N	6	No	No	–	0.9	Poor	NA	Slow	1
<i>Iceland</i>	65N	340	Yes?	<i>Greenland</i>	61	1.4	Good	High	Slow	4+?
Jan Mayen	71N	352	No?	Yes?	–	NA	Poor	NA	Slow	1+?
Juan de Fuca/Cobb	46N	230	Yes	No	–	0.3	Fair	NA	Slow	2+?
Juan Fernandez	34S	277	Yes?	No	–	1.6	Poor	High	0	2+?
Kerguelen (Herad)	49S	69	Yes	Rajmahal?	118	0.5	Poor	high	0	2+?
<i>Louisville</i>	51S	219	Yes	<i>Ontong-Java</i>	122	0.9	Poor	NA	Slow	3+?
Lord Howe (Tasman East)	33S	159	Yes?	No	–	0.9	Poor	NA	Slow	1+?
Macdonald (Cook-Austral)	30S	220	Yes?	Yes?	–	3.3	Fair	High?	Slow	2+?
Marion	47S	38	Yes	Madagascar?	88	NA	NA	NA	0	1+?
Marqueses	10S	222	Yes	Shatski?	???	3.3	NA	Low	0	2+?
Martin/Trindade	20S	331	Yes?	No	–	0.5	Poor	NA	Fast	0+?
Meteor	52S	1	Yes?	No	–	0.5	Poor	NA	0	0+?
Pitcairn	26S	230	Yes	No	–	3.3	Fair	High?	0	2+?
Raton	37N	256	Yes?	No	–	NA	NA	NA	Slow	1+?
<i>Reunion</i>	21S	56	Yes	<i>Deccan</i>	65	1.9	Poor	High	0	4
St. Helena	17S	340	Yes	No	–	0.5	Poor	Low	0	1
<i>Samoa</i>	14S	190	Yes	<i>No?</i>	14?	1.6	Poor	High	Slow	4
San Felix	26S	280	Yes?	No	–	1.6	Poor	NA	0	1+?
Socorro	19N	249	No	No	–	NA	Poor	NA	Slow	1+?
Tahiti/Society	18S	210	Yes	No	–	3.3	Fair	High?	0	2+?

(continued)

**Table 2.1** (continued)

Scores for 49 hotspots with respect to five criteria used to diagnose a potentially deep origin										
Hotspot	Lat	Lon (°E)	Track	Flood/plateau	Age (Ma)	Buoy.	Reliab.	<sup>3</sup> He/ <sup>4</sup> He	Tomo (500)	Count
<b>Tasmanid (Tasman Central)</b>	<b>39S</b>	<b>156</b>	<b>Yes</b>	<b>No</b>	–	<b>0.9</b>	<b>Poor</b>	<b>NA</b>	<b>Slow</b>	<b>2</b>
Tibesti	21N	17	Yes?	No	–	NA	Poor	NA	0	0+?
<i>Tristan</i>	<b>37S</b>	<b>348</b>	<b>Yes</b>	<i>Parana</i>	<b>133</b>	<b>1.7</b>	<i>Poor</i>	<i>Low</i>	<b>0</b>	<b>3</b>
Vema	33S	4	Yes?	Yes? (Orange R.)	–	NA	Poor	NA	0	0+?
<b>Yellowstone</b>	<b>44N</b>	<b>249</b>	<b>Yes?</b>	<b>Columbia?</b>	<b>16</b>	<b>1.5</b>	<b>Fair</b>	<b>High</b>	<b>0</b>	<b>2+?</b>

Columns from left to right are: (1) hotspot name; (2, 3) hotspot latitude and longitude; (4) existence of a linear track or chain of dated seamounts extending from the presently active hotspot site; (5, 6) existence and age of a trap (or flood basalt, oceanic plateau); (7, 8) buoyancy flux (in  $10^3 \text{ kg s}^{-1}$ ) and its reliability; (9) existence of consistently high <sup>3</sup>He/<sup>4</sup>He ratios for the hotspot; (10) existence of a slow shear velocity ( $V_s$ ) anomaly at 500 km depth below the hotspot surface trace, based on the tomographic model of Ritsema et al. (1999); (11) count of positive responses to the five characteristics listed in the text (columns 4, 5, 7, 9 and 10). Hotspots with a total count of at least two (out of five) are shown in bold type, those with a count of at least three are in bold italics

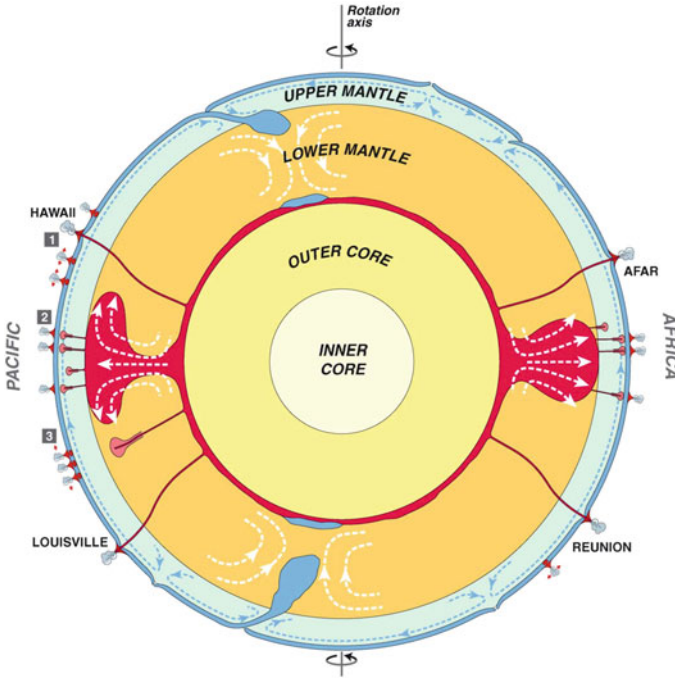


**Fig. 2.3** A schematic cross-section of the dynamic Earth, outlining the sources of the three types of plumes/hotspots identified in Courlliot et al. (2003): 1—the primary, deeper plumes possibly coming from the lowermost mantle boundary layer ( $D''$  in the broad sense), 2—the secondary plumes possibly coming from the transition zone at the locations of the superswells, while 3—the tertiary hotspots may have a superficial origin, linked to tensile stresses in the lithosphere and decompression melting (Courlliot et al. 2003)

perturbations in the asthenosphere and/or be a passive response to forms of lithospheric breakup. They are the subject matter of current research (e.g., Anderson 1998, 2000).

### 2.4.1 Superplumes

The geographic distribution of the world's major hotspots falls on two hemispheres antipodal to each other, and corresponds to crustal uplifts in East Africa and Central Pacific ocean (Courlliot et al. 2003). The same pattern is visible in seismic tomography images of shear wave velocity extending from the transition zone to the core-mantle boundary (Masters et al. 1982, 1996; Dziewonski and Woodhouse 1987; Su et al. 1994; Li and Romanowicz 1996; Ritesma et al. 1999; Gu et al. 2001) (Fig. 2.4). They are associated with superplumes, whose origin appears to be

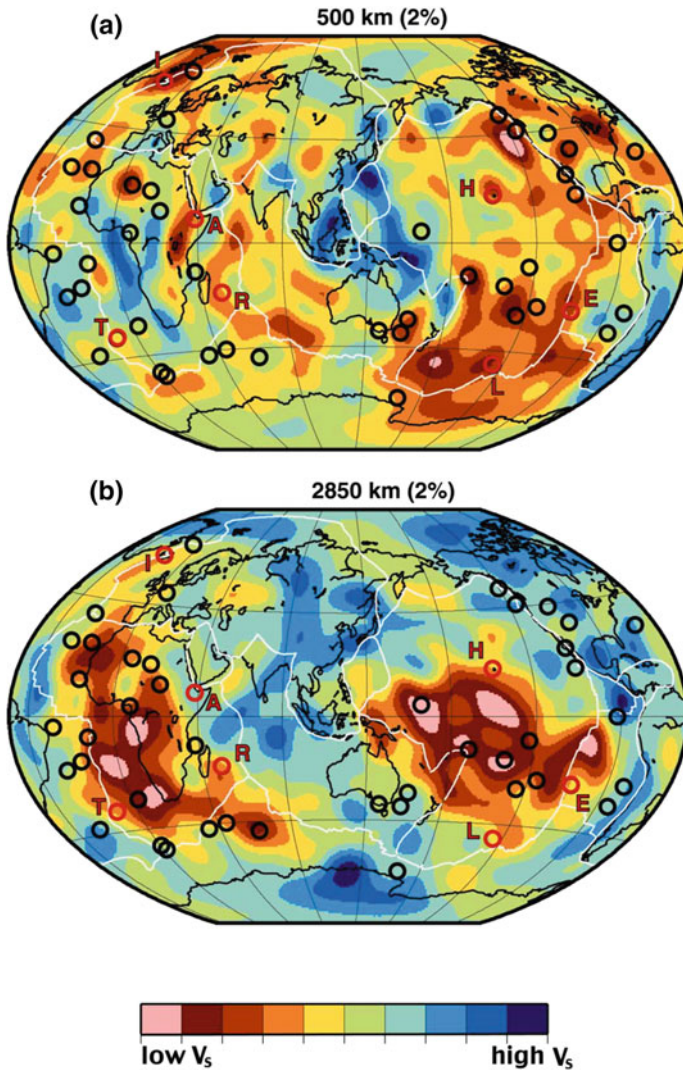


**Fig. 2.4** Distribution of the 49 hotspots (*black circles*) from Table 2.1 superimposed on a section at (a) 500 km and (b) 2850 km depths through Ritsema et al.'s (1999) tomographic model for shear wave velocity ( $V_s$ ) (Courlliot et al. 2003). The primary hotspots are shown as *red circles* with the *first letter* of their name indicated for reference

related directly to the mantle circulation. The present day convection in the lower mantle appears to be quadrupolar (Busse 1983; see Fig. 2.3), where cold, dense material subducts and sinks in the mantle, while hot, less dense, partially melted material ascends slowly below two antipodal positions below Africa and Central Pacific, forming the superplumes, with many hotspots situated over them (Chase

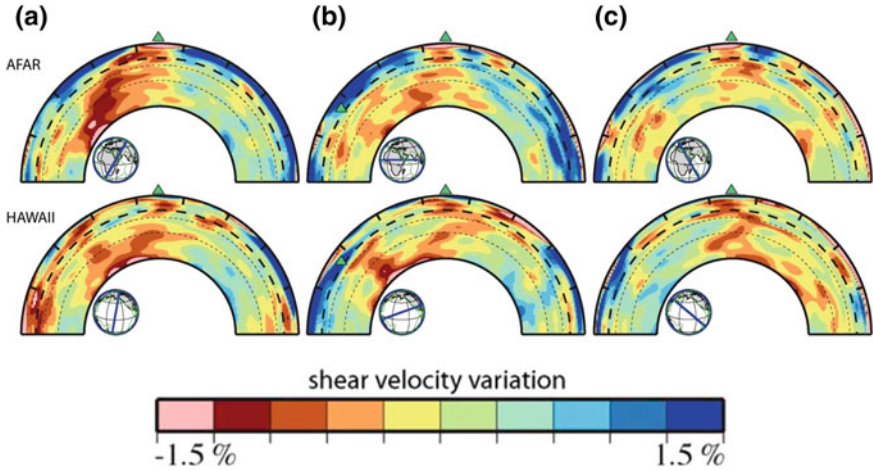


**Fig. 2.5** Shear velocity anomalies derived from model S20RTS in 180° wide cross-sections through the mantle. The *triangles* indicate the location of the Afar and Hawaii hotspots. The *red* regions have lower shear velocity than the global average at the same depth, while the *blue* regions have higher velocity than the global average, ranging between  $\pm 1.5\%$ . The 670-km discontinuity is marked by the *thick dashed line*, while the *thin dashed lines* indicate 1000 and 1700 km depth (modified from Ritsema and Allen 2003)

1979). These massive mantle upwellings, when studied in detail, appear to be of complex structure and compositionally heterogeneous (Breger and Romanowicz 1998). The shape of the African superplume at its base is complex, and it does not ascend vertically into the mantle (Fig. 2.5). A lowering of the shear wave velocity between 670 and 1000 km indicates an obstruction in the upwelling from the core-mantle boundary (Ritesma et al. 1999). However, its sharp margins suggest a stable structure in the deep mantle, and compositional heterogeneity with the surrounding mantle (Ritesma and Allen 2003).

#### 2.4.1.1 Origin of Primary Plumes

Some deep-seated plumes can be traced up to the transition zone in the upper mantle (Morganian plumes of Courlliot et al. 2003). They must, therefore, generate from instabilities in a thermal boundary layer, either at the transition zone itself or at the core-mantle boundary. Seismic tomography is not yet able to resolve plume tails in the lower mantle, but certain indirect evidences point to their origin in the lower mantle, at the D'' layer. These plumes have large flood basalt provinces associated with them, that requires melting of more than  $10^8$  km<sup>3</sup> of mantle material (Richards et al. 1989; Campbell and Griffiths 1990).

Laboratory fluid mechanic experiments suggest that it is easier to produce thermal instabilities of such large magnitude in the core-mantle boundary than at the

transition zone (Whitehead and Luther 1975; Stacey and Loper 1983; Olson et al. 1987; Bercovivi and Kelly 1997). Many of these flood basalt provinces are enriched in Fe–Si with respect to Mg (Courlliot et al. 2003), which again favors a depleted lower mantle origin for the originating plumes (Javoy 1999). The hotspot tracks associated with these plumes tend to last long, up to 130 my. For example, hotspots like Louisville and Tristan are becoming inactive, while the younger ones, like Reunion and Iceland, are still active. The observation is supported by fluid mechanic experiments, which indicate that plumes with a large head and a long enduring tail can only generate at lower mantle depths (Whitehead and Luther 1975; Stacey and Loper 1983; Olson et al. 1987; Bercovivi and Kelly 1997). Recent experiment by Farnetani and Samuel (2005), however, indicates that deep-seated plumes without a distinct head-tail structure and laterally heterogeneous tail can also occur due to shearing in the mantle.

It seems probable that the lower mantle generates two different modes of upwelling, superplumes and primary plumes, both of which develop from buoyancy anomalies. Thermo-chemical convection in a heterogeneous mantle is able to produce both these modes, depending on the local buoyancy ratio, representing a ratio of chemical density anomaly to a ratio of thermal density anomaly. For a large amount of thermal buoyancy anomaly, producing a low buoyancy ratio, the superplumes are generated. For a high chemical density anomaly, producing a high buoyancy ratio, long lived thermo-chemical primary plumes are developed (Davaille 1999, Davaille et al. 2002). Density anomalies of chemical origin in the mantle, as inferred from mineral physics and seismic studies, would be sufficient to produce both these modes depending on local conditions (Bina 1998).

#### ***2.4.2 Secondary and Tertiary Plumes***

Secondary plumes are those generated in the upper mantle, either from a primary plume/superplume or from thermal perturbations in the transition zone. The 670 km discontinuity in the mantle transition zone presents a suitable stagnation zone for plumes starting from the D'' layer. Here a separation takes place between heavier and lighter fractions in a plume containing a high proportion of denser components, such as subducted former basaltic crust (Campbell and Davies 2006). This leads to the formation of a new thermo-chemical plume head starting from the transition zone (Farnetani and Samuel 2005). Secondary thermal plumes are also generated from the thermal boundary layer between a superplume and the rest of the mantle, when the superplume get stalled at the transition zone, as seems to be the case under Polynesia (Courlliot et al. 2003). Such secondary plumes produce short-lived tracks without any flood basalts, such as Tahilti and Pitcarin. However, their motions are consistent with the primary plumes from which they are derived. Another possible origin of plumes from the 670 km discontinuity in the transition zone is by local thermal instability (White and Mckenzie 1989). Such plumes are likely to be

composed of heated upper mantle material with an entrained lower mantle axial zone (Fitton et al. 1997).

Anderson (1998, 2000) had suggested that long wavelength temperature variations of the asthenosphere depart from the mean by  $\pm 200$  °C. This ‘normal’ temperature variation at the top of the convecting mantle due to slab cooling, cratonic roots, continental insulations and edge-driven convection is sufficient to induce pseudo-plume-like upwellings leading to excess intra-plate magmatism. The process can be augmented by shears driven by moving plates and the rise of the asthenosphere between cratons. Ballmer et al. (2007) have pointed out that small-scale sub-lithospheric convection can give rise to chains of volcanic islands, which can lack a definite age progression, without requiring the presence of any plume underneath.

## 2.5 Plume-Related Lithospheric Uplift

Impingement of a hot, ascending mantle plume below the lithosphere results in the formation of a broad swell, 2000–2500 km in diameter, above the flattened plume head (e.g., Griffiths and Campbell 1991; He et al. 2003; Fig. 2.6). The different mechanisms generating the lithospheric uplift can be summarized as:

1. Dynamic uplift is generated when abnormally hot mantle is emplaced beneath the lithosphere. The support mechanism is a combination of impact of the plume, buoyancy due to ponding of the plume material below the lithosphere (Guillou-Frottier et al. 2007) and thermo-mechanical erosion at the base of the lithosphere (Davies 1994; d’Acremont et al. 2003). It is indicated by a positive

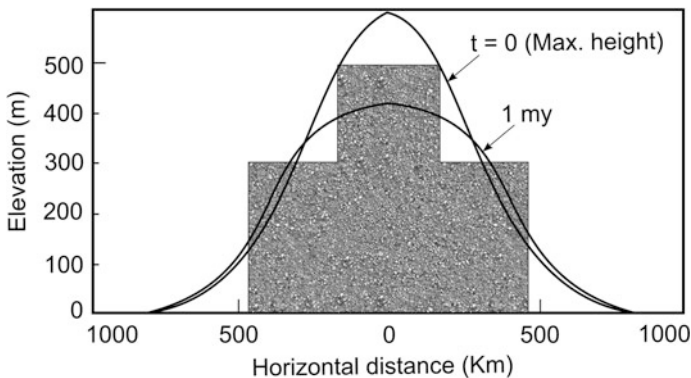


**Fig. 2.6** Uplift above a plume head, as predicted by Griffiths and Campbell (1991), compared with the uplift observed at the center of the Emeishan flood basalt by He et al. (2003) (modified from Campbell and Davies 2006). Predicted profiles are given for maximum uplift ( $t = 0$ ) when the top plume is at a depth of  $\sim 250$  km, and 1 my later ( $t = 1$  my) when flattening of the head is essentially complete

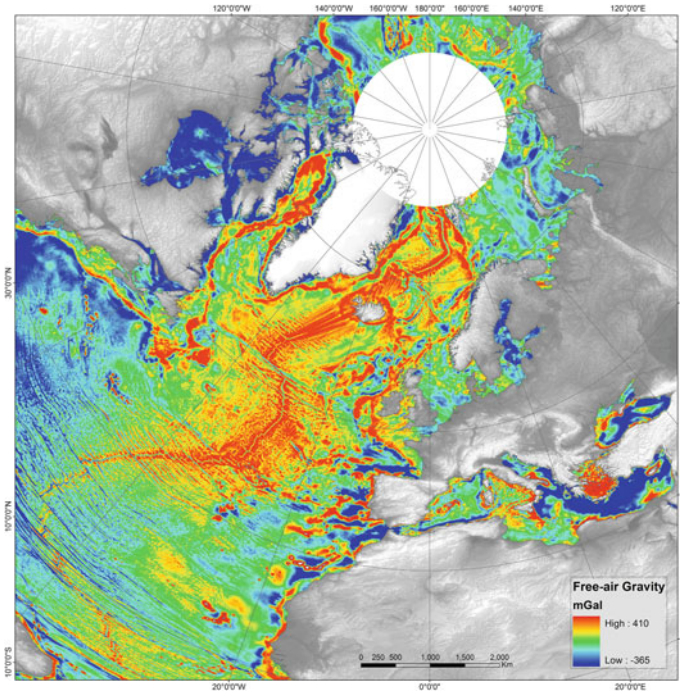


**Fig. 2.7** Free-air gravity anomaly over part of the northern hemisphere, displayed using a Polar Lambert azimuthal equal-area projection. Note the long-wavelength gravity high centred on Iceland, and extending from south of the Azores to Spitzbergen and from Baffin Island to Scandinavia. Gravity anomaly data from Sandwell and Smith (2009)

anomaly of wavelength more than 1000 km long in the free-air gravity data (Sclater et al. 1975; McKenzie 1994) (Fig. 2.7). The uplift is a transient phenomenon, which disappears when the thermal anomaly dissipates by conduction and convection (Nadin et al. 1995, 1997; Jones et al. 2002). The Iceland plume in the North Atlantic region serves as a typical example.

2. Permanent uplift occurs due to crustal thickening when plume-related thermal anomalies induce melting and the melt is injected into or just beneath the crust. The ensuing magmatic underplating results in isostatic uplift of the crust (Brodie and White 1994, 1995; Clift 1997; Clift and Turner 1998; White and Lovell 1997). For example, permanent uplift affected Britain and Ireland during Paleocene time, and the regions flanking the line of continental separation at the Paleocene- Eocene boundary (Jones et al. 2002).
3. Isostatic thermal uplift occurs due to heating and decrease of density of the lithosphere by the ascending hot plume material. It is a transient phenomenon, adding to the dynamic topography, which dissipates with the disappearance of the plume head (Sleep 1990; Clift and Turner 1998).

## 2.6 Morphology of Hotspot Tracks

The features like morphology and volume of eruption of hotspot tracks (Figs. 2.8 and 2.9) strongly depend on the nature the affected lithosphere, particularly its age during the time of eruption. Hotspot ridges fall into two broad categories (Honsho and Tamaki 1995; Fig. 2.10):

1. volcanic ridges formed in intra-plate setting tend to form discrete seamounts or guyots, which originate in a thick plate, regionally supported by lithospheric flexure, and
2. volcanic ridges formed in young lithosphere near sea-floor spreading centers tend to form continuous ridges, locally supported by the Airy isostasy of low density roots.

Example of the former is provided by the Hawaii-Emperor Chain, while the 90°E Ridge provides the second example.

The Hawaii-Emperor Chain extends for about 6000 km across the North Pacific, with about 107 individual volcanoes (Clague and Dalrymple 1987; Fig. 2.11a) being constructed in the last 70 my by the Hawaiian hotspot. The bathymetric profile

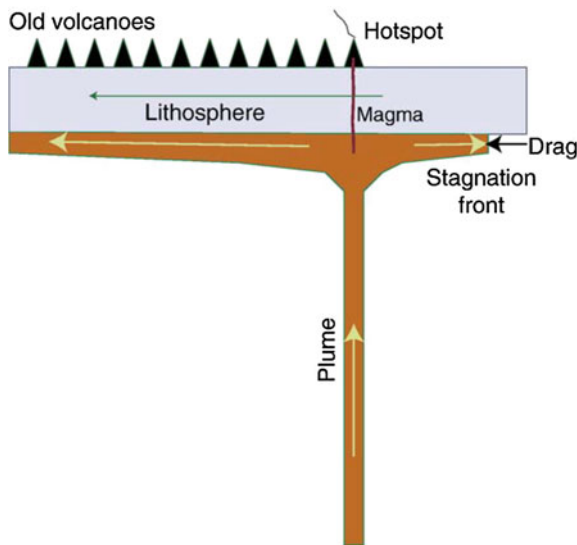


**Fig. 2.8** Schematic diagram of a hotspot track produced by plume beneath fast-moving plate (Sleep 2006). A chain of volcanoes forms when the plate passes over the plume. Lateral flow of buoyant plume material complicates the flow pattern beneath the base of the lithosphere. The plate drags the plume material along with it. A stagnation front exists upstream of the hotspot

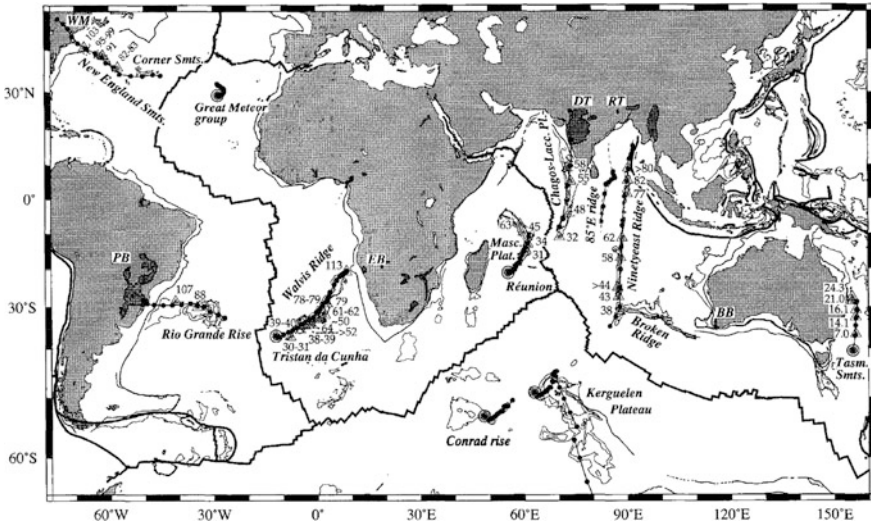


**Fig. 2.9** Major hotspot tracks in Atlantic and Indian oceans (Muller et al. 1993). Large shaded circles are locations of present-day hotspots. WM—younger White Mountains, DT—Deccan Traps, RT—Rajmahal Traps, PB—Paraná flood basalts, EB—Etendeka flood basalts, BB—Bunbury basalts. Triangles with numbers indicate radiometric ages of hotspot tracks

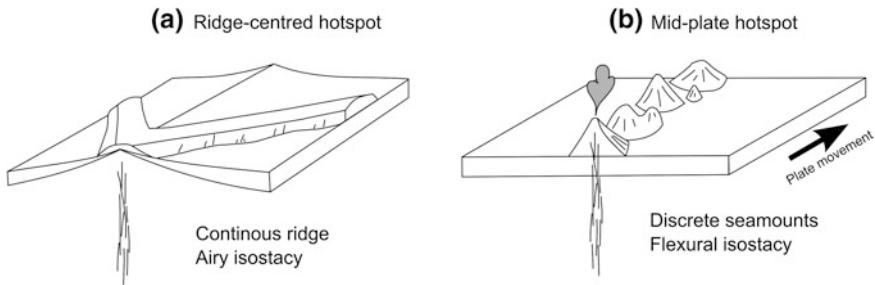


**Fig. 2.10** Diagram showing morphological differences between two broad categories of hotspot tracks, (a) hotspots formed in young lithosphere near spreading centers, and (b) hotspots in intra-plate setting (modified from Honsho and Tamaki 1995)

across the chain shows a broad, symmetrical depression, the Hawaiian Deep, surrounding the ridge, and the broad Hawaiian Arch surrounding the Deep. The isostatic equilibrium can be explained by the elastic plate model, with a best fitting elastic thickness of 20–30 km for the Hawaiian and about 20 km for the Emperor Chain. The age of the crust during eruption is between 80 and 90 my for the Hawaiian chain, and then decreases from about 80 my at the bend to 20 my towards the northern end (Honsho and Tamaki 1995).

The 90°E Ridge has resulted from the volcanism of the Kerguelen hotspot (Royer et al. 1991) and extends for about 4000 km along the 90°E meridian

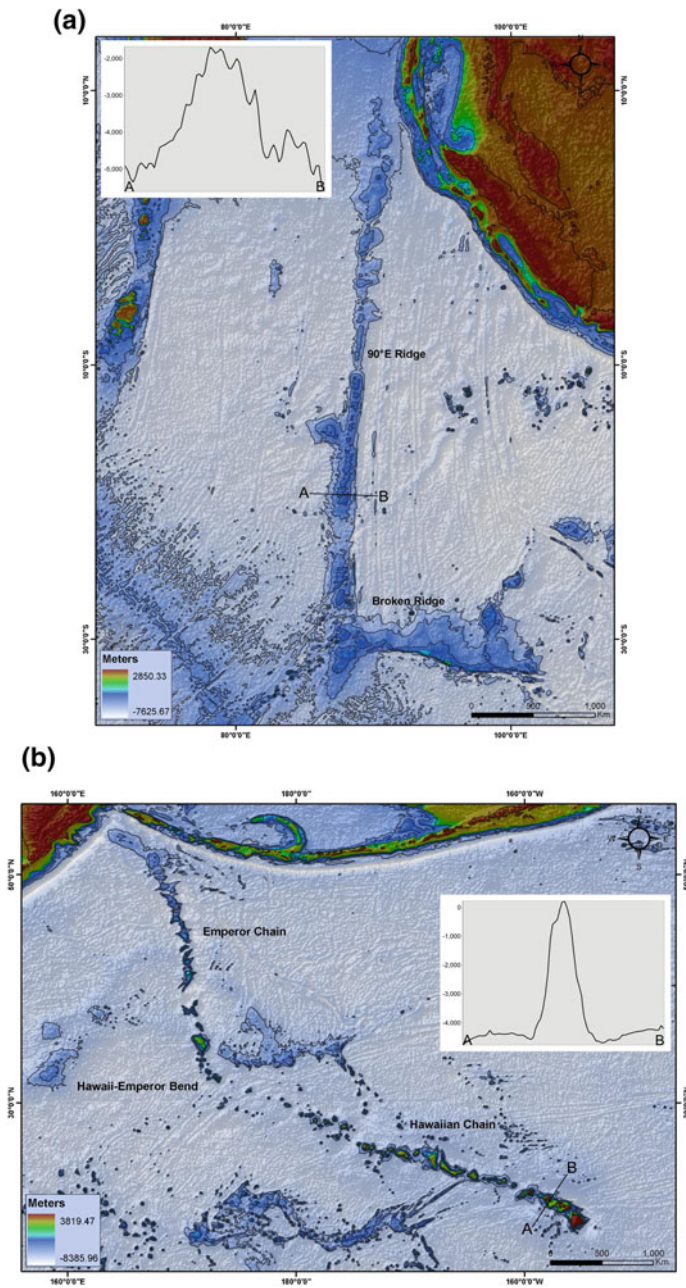


**Fig. 2.11** Bathymetry for (a) Hawaiian-Emperor seamount chain, and (b) Ninetyeast ridge, contoured at 500 m intervals (redrawn after Honsho and Tamaki 1995). Lines with annotations represent location of profiles shown in inset

(Fig. 2.11b). It has the continuous shape of an elongated plateau without any break. The profile across it shows no depressions around the ridge, except those associated with fracture zones to the east. The ridge has a steep eastern flank indicative of block faulting (Detrick and Watts 1979). Its isostatic adjustments are explained by the Airy model, with a best fitting elastic thickness of 15–25 km (Honsho and Tamaki 1995). Drilling results from DSDP legs 21 and 26, and ODP leg 121, show a close correspondence between the age of the ridge and the surrounding oceanic crust, indicating its eruption in a young lithosphere near a spreading centre.

## 2.7 Moat and Arch

The impact of a mantle plume beneath the lithosphere leads to a broad swell around the erupting centers, within which voluminous magma eruption takes place. The load of the volcanoes bends the underlying elastic lithosphere, creating a trough-like depression around the volcano called flexural moat. Away from the moat, isostatic upwelling causes the formation of a peripheral bulge, also termed as flexural arch (Rees et al. 1993). Examples come from Hawaii, Marquesas and Canary Islands (Figs. 2.12 and 2.13).

The best studied example comes from the Hawaiian island, where lithospheric flexure induced by the weight of the volcanoes creates the Hawaiian moat, called the Hawaiian Deep, surrounding the island chain. The moat is bounded by a sea-floor rise known as the Hawaiian Arch, located about 250 km seaward of the island chain (Hamilton 1957; Menard 1964). Both the flexural moat and bulge are superimposed on a bathymetric high of larger wavelength of about 1200 km, known as the Hawaiian Swell (Detrick and Crough 1978). The moat and the bulge are divided into flanking segments in the north, south and front, known respectively as the North Hawaiian Moat/Arch, South Hawaiian Moat/Arch, and Frontal Hawaiian Moat/Arch. Moat to bulge relief in the flanking segments exceeds 1 km compared to about 200–450 m in the frontal region. This indicates less subsidence of the oceanic crust in the front (Leslie et al. 2002). The frontal segments are short-lived in comparison to the flanking segments due to being devoured by the growing Hawaiian ridge as the Pacific plate migrates across the Hawaiian hotspot. Widespread mass-wasting derived sediments fill up the moats that get eventually covered by subsequent volcanic rocks of the Hawaiian ridge (Moore and Clague 1992; Rees et al. 1993; Smith et al. 1999; Naka et al. 2002).

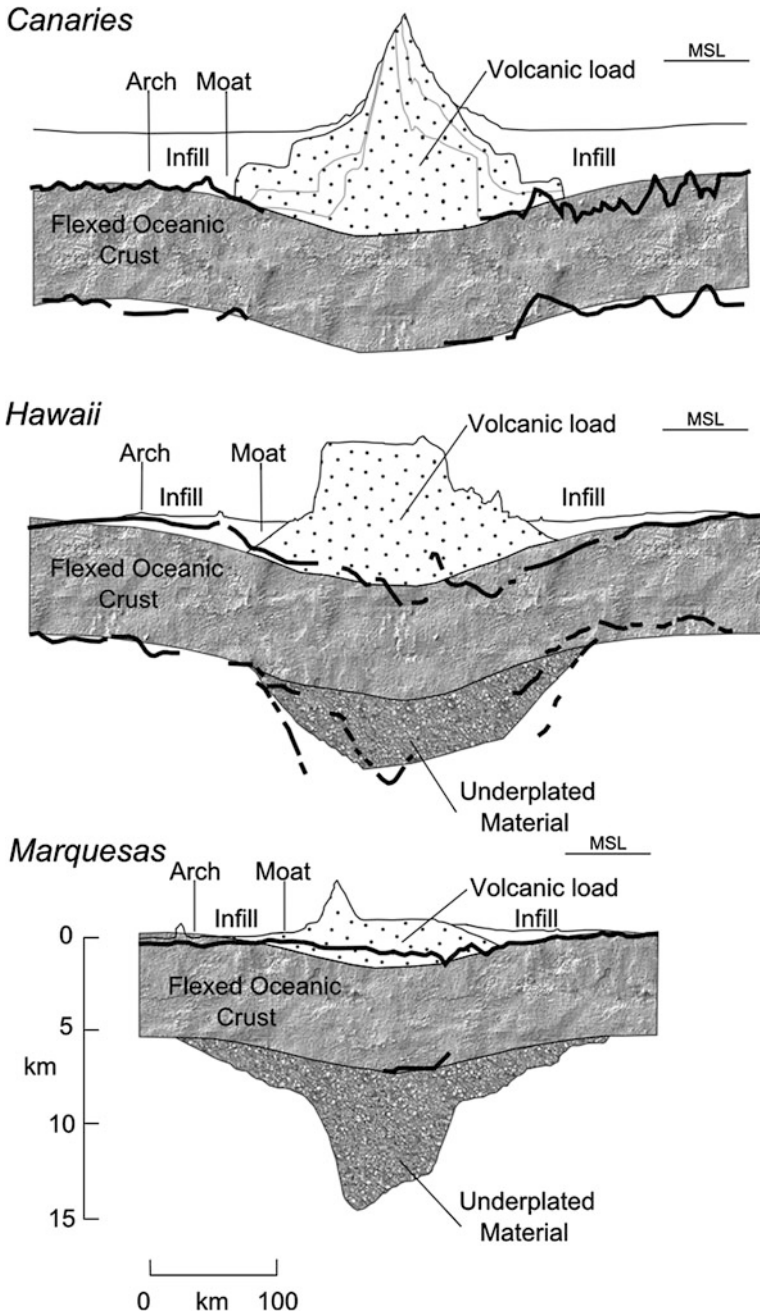


**Fig. 2.12** Transects across Canary Islands, Hawaii and Marquesas, showing the development of the flexural moat and arch (modified from Watts et al. 1997)

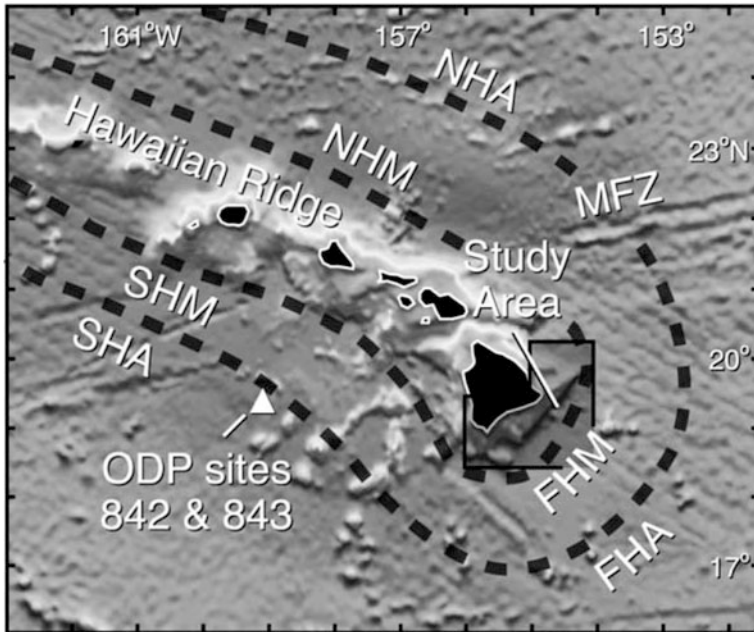


**Fig. 2.13** Shaded relief bathymetric map of the Hawaiian Ridge and surrounding flexural moat and arch (Leslie et al. 2002). The moat and arch are subdivided into frontal regions, i.e. the Frontal Hawaiian Moat (*FHM*) and Arch (*FHA*), and flanking segments, i.e. the Northern and Southern Hawaiian Moat, and the Northern and Southern Hawaiian Arch (NHM, SHM, NHA and SHA, respectively). MFZ denotes Molokai fracture zone. The location of ODP Drill Sites 842 and 843 on the South Arch is indicated by *triangle*, as also the study area of Leslie et al. (2002)

## References

- Anderson DL (1998) The edges of the mantle. In: Gurnis M et al (eds) *The core-mantle boundary region*. American Geophysical Union, Washington, DC, pp 255–271
- Anderson DL (2000) The thermal state of the upper mantle: no role for mantle plumes. *Geophys Res Lett* 27:3623–3626
- Anderson DL, Natland JH (2005) A brief history of the plume hypothesis and its competitors: concept and controversy. In: Foulger GR, Natland JH, Presnall DC (eds) *Plates, plumes, and paradigms*. Geological Society of America Special Paper 388, pp 119–145
- Ballmer MD, van Hunen J, Ito G, Tackley PJ, Bianco TA (2007) Non-hotspot volcano chains originating from small-scale sublithospheric convection. *Geophys Res Lett* 34 (L23310). doi:[10.1029/2007GL031636](https://doi.org/10.1029/2007GL031636)
- Bercovici D, Kelly A (1997) The non-linear initiation of diapirs and plume heads. *Phys Earth Planet Int* 101:119–130
- Bina CR (1998) Lower mantle mineralogy and the geophysical perspective. In: Hemley RJ (ed) *Ultra-high pressure mineralogy*. Reviews in mineralogy, vol 37. Mineralogical Society of America
- Bréger L, Romanowicz B (1998) Three-dimensional structure at the base of the mantle beneath the central Pacific. *Science* 282:718–720

- Brodie J, White N (1994) Sedimentary basin inversion caused by igneous underplating: Northwest European continental shelf. *Geology (Boulder)* 22(2):147–150
- Brodie J, White N (1995) The link between sedimentary basin inversion and igneous underplating. In: Buchanan JG, Buchanan PG (eds) *Basin inversion*. Geological Society Special Publications, London, pp 21–38
- Busse FH (1983) Quadrupole convection in the lower mantle. *Geophys Res Lett* 10(4):285–288
- Campbell IH (2006) Large igneous provinces and the mantle plume hypothesis. *Elements* 1: 265–269
- Campbell IH (2007) The case for mantle plumes. <http://www.mantleplumes.org/Plumes.html>. Accessed 28 June 2016
- Campbell IH, Davies GF (2006) Do mantle plumes exist? *Episodes* 29(3)
- Campbell IH, Griffiths RW (1990) Implications of mantle plume structure for the evolution of flood basalts. *Earth Planet Sci Lett* 99:79–93
- Chase CG (1979) Subduction, the geoid, and lower mantle convection. *Nature* 282:464–468
- Clague DA, Dalrymple GB (1987) The Hawaiian-Emperor volcanic chain: part I, geologic evolution. In: Decker RW et al (eds) *Volcanism in Hawaii*. Reston, Virginia, United States Geological Survey Professional Paper 1350, pp 5–54
- Clift PD (1997) The thermal impact of Paleocene magmatic underplating in the Faeroe-Shetland-Rockall region. In: Fleet AJ, Boldy SAR (eds) *Petroleum geology of Northwest Europe*. Proceedings of the 5th conference, London, UK, pp 585–593
- Clift PD, Turner J (1998) Paleogene igneous underplating and subsidence anomalies in the Rockall-Faeroe-Shetland area. *Mar Pet Geol* 15(3):223–243
- Clouard V, Bonneville A (2001) How many Pacific hotspots are fed by deep-mantle plumes? *Geology* 21:695–698
- Courtillot V, Davaille A, Besse J, Stock J (2003) Three distinct types of hotspots in the Earth's mantle. *Earth Planet Sci Lett* 205:295–308
- d'Acromont E, Leroy S, Burov EB (2003) Numerical modelling of a mantle plume: the plume head-lithosphere interaction in the formation of an oceanic large igneous province. *Earth Planet Sci Lett* 206:379–396
- Davaille A (1999) Simultaneous generation of hotspots and superswells by convection in a heterogeneous planetary mantle. *Nature* 402:756–760
- Davaille A, Girard F, Le Bars M (2002) How to anchor hotspots in a convecting mantle? *Earth Planet Sci Lett* 203:621–634
- Davies GF (1988) Ocean bathymetry and mantle convection, 1. Large-scale flow and hotspots. *J Geophys Res* 93:10467–10480
- Davies GF (1994) Thermomechanical erosion of the lithosphere by mantle plumes. *J Geophys Res* 99(B8):15709–15722
- Detrick RS, Crough ST (1978) Island subsidence, hotspots and lithospheric thinning. *J Geophys Res* 83:1236–1244
- Detrick RS, Watts AB (1979) An analysis of isostasy in the world's oceans 3. Aseismic ridges. *J Geophys Res* 84:3637–3653
- Dziewonski AM, Woodhouse JH (1987) Global images of the Earth's interior. *Science* 236:37–48
- Farnetani CG, Samuel H (2005) Beyond the thermal plume paradigm. *Geophys Res Lett* 32 (L07311)
- Fitton JG, Saunders AD, Norry MJ, Hardarson BS, Taylor RN (1997) Thermal and chemical structure of the Iceland plume. *Earth Planet Sci Lett* 153:197–208
- Griffiths RW, Campbell IH (1990) Stirring and structure in mantle starting plumes. *Earth Planet Sci Lett* 99:66–78
- Griffiths RW, Campbell IH (1991) Interaction of mantle plume heads with the Earth's surface and the onset of small-scale convection. *J Geophys Res* 96:18295–18310
- Gu YJ, Dziewonski AM, Su W, Ekstrom G (2001) Models of the mantle shear velocity and discontinuities in the pattern of lateral heterogeneities. *J Geophys Res* 106:11169–11189
- Guillou-Frottier L, Burov E, Nehlig P, Wyns R (2007) Deciphering plume–lithosphere interactions beneath Europe from topographic signatures. *Glob Planet Change* 58:119–140

- Hamilton EL (1957) Marine geology of the southern Hawaiian Ridge. *Geol Soc Am Bull* 68:1011–1026
- He B, Xu Y-G, Chung S-L, Xiao L, Wang Y (2003) Sedimentary evidence for a rapid crustal doming prior to the eruption of the Emeishan flood basalts. *Earth Planet Sci Lett* 213:389–403
- Honsho C, Tamaki K (1995) Differences in morphology and structure between hotspot tracks: effects of the lithospheric age at the time of formation. In: Yukutake T (ed) *The Earth's central part: its structure and dynamics*. pp 331–342
- Javoy M (1999) Chemical earth models. *Comptes Rendus de l'Académie des Sciences - Series IIA - Earth and Planetary Science* 329:537–555
- Jones SM, White N, Clarke BJ, Rowley E, Gallagher K (2002) Present and past influence of the Iceland Plume on sedimentation. In: Dore AG, Cartwright JA, Stoker MS, Turner JP, White N (eds) *Exhumation of the North Atlantic margin: timing, mechanisms, and implications for petroleum exploration*. Geological Society of London, Special Publications, London, pp 13–25
- Kellog LH, King SD (1997) The effect of temperature dependant viscosity on the structure of new plumes in the mantle: results of a finite element model in a spherical axisymmetrical shell. *Earth Planet Sci Lett* 148:13–26
- Leitch AM, Davies GF (2001) Mantle plumes and flood basalts: enhanced melting from plume ascent and an eclogite component. *J Geophys Res* 106:2047–2059
- Leslie SC, Moore GF, Morgan JK, Hills DJ (2002) Seismic stratigraphy of the Frontal Hawaiian Moat: implications for sedimentary processes at the leading edge of an oceanic hotspot trace. *Mar Geol* 184:143–162
- Li XD, Romanowicz B (1996) Global mantle shear velocity model developed using non-linear asymptotic coupling theory. *J Geophys Res* 101:22245–22272
- Lin SC, van Keken PE (2006) Dynamics of thermochemical plumes: 1. Plume formation and entrainment of a dense layer. *Geochem Geophys Geosyst* 7 (Q02006). doi:[10.1029/2005GC001071](https://doi.org/10.1029/2005GC001071)
- Lowman JP, King SD, Gable CW (2004) Steady plumes in viscous stratified, vigorously convecting, three-dimensional numerical mantle convection models with mobile plates. *Geochem Geophys Geosyst* 5 (Q01L01). doi:[10.1029/2003GC000583](https://doi.org/10.1029/2003GC000583)
- Masters G, Jordan TH, Silver PG, Gilbert F (1982) Aspherical Earth structure from fundamental spheroidal-mode data. *Nature* 298:609–613
- Masters G, Johnson S, Laske G, Bolton H (1996) A shear velocity model of the mantle. *Philos Trans R Soc Lond Ser A* 354:1385–1410
- McKenzie D (1994) The relationship between topography and gravity on Earth and Venus. *Icarus* 112:55–88
- McKenzie D, Bickle MH (1988) The volume and composition of melts generated by extension of the lithosphere. *J Petrol* 29:625–679
- Menard HW (1964) *Marine geology of the Pacific*. McGraw-Hill, New York
- Moore JG, Clague DA (1992) Volcano growth and evolution of the island of Hawaii. *Geol Soc Am Bull* 104:1471–1484
- Morgan WJ (1971) Convection plumes in the lower mantle. *Nature* 230:42–43
- Morgan WJ (1972) Plate motions and deep mantle convection. *Geol Soc Am Bull* 132:7–22
- Morgan WJ (1978) Rodriguez, Darwin, Amsterdam, ... a second type of hotspot island. *J Geophys Res* 83:5355–5360
- Müller RD, Royer J-Y, Lawver LA (1993) Revised plate motions relative to the hotspots from combined Atlantic and Indian Ocean hotspot tracks. *Geology* 21(3):275–278
- Nadin PA, Kuszniir NJ, Toth J (1995) Transient regional uplift in the early Tertiary of the northern North Sea and the development of the Iceland Plume. In: White RS, Morton AC (eds) *Second Arthur Holmes European research meeting*. J Geol Soc Lond. Reykjavik, Iceland, pp 953–958
- Nadin PA, Kuszniir NJ, Cheadle MJ (1997) Early Tertiary plume uplift of the North Sea and Faeroe-Shetland basins. *Earth Planet Sci Lett* 148(1–2):109–127
- Naka J, Kanamatsu T, Lipman PW, Sisson TW, Tsuboyama N, Morgan JK, Smith JR, Ui T (2002) Deepsea volcanoclastic sedimentation around the southern flank of Hawaii Island. In:

- Takahashi E, Lipman PW, Garcia MO, Naka J, Aramaki S (eds) Hawaiian volcanoes: deep underwater perspectives. AGU Monograph 128, pp 29–50
- Olson P, Schubert G, Anderson C (1987) Plume formation in the D" layer and the roughness of the core-mantle boundary. *Nature* 327:409–413
- Rees BA, Detrick RS, Coakley BJ (1993) Seismic stratigraphy of the Hawaiian flexural moat. *GSA Bull* 105(2):189–205
- Richards MA, Duncan RA, Courtillot VE (1989) Flood basalts and hot-spot tracks: plume heads and tails. *Science* 246:103–107
- Ritsema J, Allen RM (2003) The elusive mantle plume. *Earth Planet Sci Lett* 207(1):1–12
- Ritsema J, van Heijst HJ, Woodhouse JH (1999) Complex shear wave velocity structure imaged beneath Africa and Iceland. *Science* 286:1925–1928
- Royer JY, Peirce JW, Weissel JK (1991) Tectonic constraint on the hot-spot formation of Ninetyeast Ridge. In: Weissel J, Peirce J, Taylor E, Alt J, et al (eds) *Proceedings of ODP scientific results. College Station TX (Ocean Drilling Program)*, pp 763–776
- Sandwell DT, Smith WHF (2009) Global marine gravity from retracked Geosat and ERS-1 altimetry: ridge segmentation versus spreading rate. *J Geophys Res* 114 (B0141)
- Slater JG, Lawyer LA, Parsons B (1975) Comparison of long wavelength residual elevation and free-air gravity anomalies in the North Atlantic and possible implications for the thickness of the lithospheric plate. *J Geophys Res* 80:1031–1052
- Sleep NH (1990) Hotspots and mantle plumes: some phenomenology. *J Geophys Res* 95 (B5):6715–6736
- Sleep NH (2002) Ridge-crossing mantle plumes and gaps in tracks. *Geochem Geophys Geosyst* 3 (12):1–33. doi:[10.1029/2001GC000290](https://doi.org/10.1029/2001GC000290)
- Sleep NH (2006) Mantle plumes from top to bottom. *Earth Sci Rev* 77:231–271
- Smith JR, Malahoff A, Shor AN (1999) Submarine geology of the Hilina Slump and morpho-structural evolution of Kilauea volcano, Hawaii. *J Volcanol Geotherm Res* 94:59–88
- Stacey FD, Loper DE (1983) The thermal boundary layer interpretation of D" and its role as a plume source. *Phys Earth Planet Int* 33:45–55
- Steinberger B (2000) Plumes in a convecting mantle: Models and observations for individual hotspots. *J Geophys Res* 105:11127–11152
- Su WR, Woodward RL, Dziewonski AM (1994) Degree 12 model of shear velocity heterogeneity in the mantle. *J Geophys Res* 99:6945–6981
- Turcotte DL, Oxburgh ER (1973) Mid-plate tectonics. *Nature* 244:337–339
- Watts AB, Peirce C, Collier J, Dalwood R, Canales JP, Henstock TJ (1997) A seismic study of lithospheric flexure in the vicinity of Tenerife, Canary Islands. *Earth Planet Sci Lett* 146:431–447
- White N, Lovell B (1997) Measuring the pulse of a plume with the sedimentary record. *Nature* 387 (6636):888–891
- White R, McKenzie D (1989) Magmatism at rift zones: the generation of volcanic continental margins and flood basalts. *J Geophys Res* 94:7685–7729
- Whitehead JR, Luther DJ (1975) Dynamics of laboratory diaper and plume models. *J Geophys Res* 80:705–717
- Wilson JT (1963) A possible origin of the Hawaiian Islands. *Can J Phys* 41:863–870

# Chapter 3

## Dynamic Crustal Uplift Due to Plume Activity

### 3.1 Ascent of a Mantle Plume

Plume ascent is driven by buoyancy due to density difference from the surrounding material. The mechanism of plume ascent is investigated in a number of studies (e.g., Weinberg and Podladchikov 1994 and references therein).

For isothermal spherical plume and Newtonian viscosity, Stoke's law gives the forces acting on the plume as the buoyancy force (D'Acremont et al. 2003):

$$f_a = \Delta\rho g(4/3\pi r^3) \tag{3.1}$$

and the viscous drag force:

$$f_v = 6\pi r\eta v_s \tag{3.2}$$

where  $\Delta\rho$  is the density contrast (10–100 kg/m<sup>3</sup>),  $r = D/2$  is the plume radius,  $\eta$  is the mean viscosity of the surrounding material, and  $v_s$  is the ascent velocity.

To initiate ascent, the ratio  $f_a/f_v$  should exceed 1, which gives the ascent velocity as:

$$v_s = 2/9\Delta\rho gr^2\eta^{-1} \tag{3.3}$$

The heat diffusion time,  $t_d$ , and ascent time,  $t_a$ , are then given by:

$$t_d = rK^{-1} \tag{3.4}$$

and

$$t_a = (d - h)v_s \tag{3.5}$$

where  $d$  is the initial plume depth and  $h$  is the final depth below the lithosphere,  $K$  is the thermal diffusivity (defined in Eq. 1.33, Chap. 1).

Equation 3.1 is obtained for infinite space and is only applicable at great depths, during the initiation of the plume. It gives ascent rates of 0.2–0.5 m/yr (e.g., Whitehead and Luther 1975). Temperature-dependent Newtonian viscosity gives values of 1–2 m/yr (e.g., Loper and Stacey 1983), which is still low. Based on strain rate of rocks, Weinberg and Podladchikov (1994) gave approximate ascent rates for non-Newtonian viscosity as:

$$\begin{aligned} v_y &= \Delta\rho g r^2 / 3\eta_{\text{eff}} \\ &= 3^{-(n-1)} r A (\Delta\rho g r)^n / \left( 3.6^{n-1} e^{(Q/R_g T)} \right) \end{aligned} \quad (3.6)$$

where  $\eta_{\text{eff}}$  is the effective viscosity,  $A$ ,  $n$  and  $Q$  are power law constants for viscous creep in the mantle (see D’Acremont et al. 2003, Table 2, p. 386, or Burov and Guillou-Frottier 2005, Table 2, p. 476),  $R_g$  is the universal gas constant and  $T$  is the absolute temperature of the surrounding material. Assuming typical parameters, the ascent rate can be as high as 10–5000 m/yr (Burov and Guillou-Frottier 2005).

The density difference,  $\Delta\rho$ , is a combination of thermal and chemical density difference of the plume from the surrounding. It can be written as (Burov and Guillou-Frottier 2005):

$$\Delta\rho = \Delta\rho_{\text{ch}} + \alpha\rho_m \Delta T \quad (3.7)$$

The actual density of the plume material is given by:

$$\rho_p = \rho_m + \Delta\rho_{\text{ch}} + \alpha\rho_m \Delta T \quad (3.8)$$

where  $\alpha$  is the coefficient of thermal expansion,  $\Delta\rho_{\text{ch}}$  is the chemical density difference,  $\rho_p$  and  $\rho_m$  are the plume and initial mantle densities, respectively, and  $\Delta T$  is the temperature difference.

Depth invariant  $\alpha$  gives  $\Delta T$  values in the order of 100–300 °C and  $\Delta\rho$  due to thermal expansion in the order of 10–30 kg/m<sup>3</sup>. Experimental data suggest a strong dependence of  $\alpha$  on temperature and pressure. It increases up to the Moho, then decreases from 1300 °C isotherm at about 150–200 km depth with increasing temperature and pressure (Cooper and Simmons 1977; Bauer and Handin 1983), and then gets reduced to half by 400–660 km depth. Consequently, an ascending plume at this depth requires either higher  $\Delta T$ , up to 500 °C, or higher  $\Delta\rho_{\text{ch}}$  (Burov and Guillou-Frottier 2005).

For fast ascent at great depths, the heat transfer from the plume is negligible. However, in later stages of ascent, as the velocity decreases, the heat loss and thermal softening of the surrounding rock increase. The velocity decline is caused by (D’Acremont et al. 2003):

1. increased viscosity of the cold lithospheric rocks,
2. decrease in chemical density contrast, and
3. presence of the free upper surface of the lithosphere.

Plume head flattening starts as soon as the plume reaches the base of the lithosphere. The flattening is caused by the ascent of the trailing edge being faster than that of the leading one. The factors controlling the flattening can be listed as:

1. decrease in buoyancy force near the surface causing a decrease in the ascent velocity of the leading edge (D'Acremont et al. 2003);
2. increasing viscosity gradient in the lithosphere-asthenosphere boundary causing the slowdown of the leading edge (Olson and Nam 1986); and
3. the strength of the lithospheric plate that generates higher pressure on the leading edge of the plume (Olson and Nam 1986; D'Acremont et al. 2003).

The diameter of the plume head is given by (Griffiths and Campbell 1990)

$$D = Q^{1/5} (v/g\alpha\Delta T)^{1/5} k^{2/5} Z^{3/5} \quad (3.9)$$

where  $Q$  is the buoyancy flux,  $v$  is the kinematic viscosity of the lower mantle,  $Z$  ( $=d - h$ ) is the height of rise of the head and  $k$  is the thermal conductivity.

The main factor governing the diameter of the plume head is its ascent height. Thus, for a plume starting at the core-mantle boundary, the calculated diameter is 1000–1200 km, which flattens to a disk of 2000–2400 km at the base of the lithosphere. The calculated time for the plume to travel this distance is about 100 my (Campbell 2006).

## 3.2 Dynamic Uplift and Topography

Impingement of an ascending plume beneath the lithosphere results in a dynamic topography, whose uplift can be estimated from both theoretical and experimental results (e.g., Olson and Nam 1986; Griffiths et al. 1989; Hill 1991; Ribe and Christensen 1994; Ribe 1996; D'Acremont et al. 2003; Burov and Guillou-Frotier 2005).

Laboratory experiments on the evolution of the surface topography due to buoyant uprise of a diapir through viscous fluid have been studied by Olson and Nam (1986) and Griffiths et al. (1989). They showed that as the diapir approaches the lithosphere, a broad axisymmetric swell appears. It initially increases in height, reaches a maximum when the leading edge of the diapir is  $0.2 D$  below the surface, and then subsides as the diapir flattens below the surface. The maximum uplift,  $H_{\max}$ , is given by Griffiths et al. (1989):

$$H_{\max} = 0.25(1 - \lambda)(\Delta\rho D_0)/\rho_m \quad (3.10)$$

where  $\lambda = (\rho_m - \rho_l)/(\rho_m - \rho_p)$ ,  $\rho_m$ ,  $\rho_l$  and  $\rho_p$  are the upper mantle, lithospheric and plume head densities, respectively, and  $D_0$  is the diameter of the plume head.

Hill (1991) quantified the surface uplift over a spreading mantle plume as:

$$H = \alpha \Delta T L \quad (3.11)$$

where  $H$  is the dynamic uplift and  $L$  is the thickness of the flattened plume head.

The general sequence of events shows that the uplift begins long before the plume head reaches the lithosphere, subsequently reaching a maximum, and then eventually turns into slow subsidence (Olson and Nam 1986; Griffiths et al. 1989; Campbell and Griffiths 1990; Griffiths and Campbell 1990). Uplift begins 10–20 my before the plume reaches the lithosphere, when it is still at a depth of  $\sim 500$  km. It reaches a maximum when the plume is  $\sim 0.1$ – $0.2$   $D$  from the surface, at  $\sim 150$ – $200$  km depth (Griffiths et al. 1989; Campbell and Griffiths 1990). Griffiths et al. (1989) demonstrated that for large density and viscosity contrast of the lithosphere from the plume material, two orders of swells forms: an initial broad dome, and subsequently an elevated central region. The outer swell decays when the diapir nears the base of the lithosphere, and only the central high remains, supported by the buoyant plume below. Using  $\Delta T = 100$  °C, Campbell and Griffiths (1990) calculated a maximum uplift of 500–1000 m when the plume is at a depth of 100–200 km. This corresponds to an uplift rate of 20–40 m/my at the centre of the plume. Basaltic magmatism succeeds the maximum uplift. This happens when the leading edge of the plume reaches the base of the lithosphere.

Numerical modeling by D’Acremont et al. (2003) predicts that for non-Newtonian viscosity (Weinberg and Podladchikov 1994) and flexural isostasy, an elastic-plastic-viscous oceanic lithosphere reacts to a deep plume head at 300–350 km by a surface uplift of  $\sim 1700$  m only after 0.1 my of plume initiation from the upper mantle, at 400 km depth. The bulge increases in wavelength to  $\sim 1600$  km by 0.95 my, and the highest uplift of 1800 m is recorded at 1.4 my after the start of the plume. The Newtonian model with local isostatic compensation shows an uplift about 25 % higher than that calculated using a non-Newtonian model (Fig. 3.1). This indicates the effect of plate flexure, and hence rheology, playing an important role in the surface deformation (also see Ribe and Christensen 1994).

Burov and Guillou-Frottier (2005) first duplicated work of D’Acremont et al. (2003) for the oceanic lithosphere, and also extended it to the continental setting. Their modeling of oceanic lithosphere shows the formation of a small domal uplift of  $\sim 300$  km wavelength, superposed on a broader uplift, within 0.4 my of plume initiation from a depth of 600 km (Fig. 3.2). After the plume reaches the base of the lithosphere, by 2.5 my, thermo-mechanical erosion causes further uplift of the lithosphere. Consequent destabilization and sagging of the lithosphere leads to alternate zones of extension and compression as the plume head separates into two diverging zones, which takes place by 5 my after plume initiation.

The continental lithosphere, due to its layered rheology, acts as a multi-frequency modulator (Guillou-Frottier et al. 2007), which suppresses some

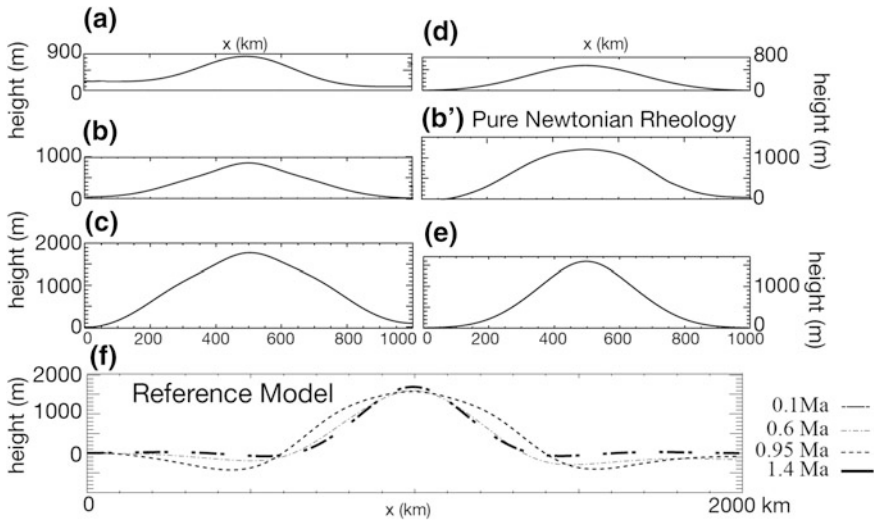


**Fig. 3.1** Dynamic surface topography between 0.1 and 1.4 my for elastic-plastic-viscous oceanic lithospheric rheology at different Rayleigh numbers, temperature differences and density differences (a–e) (D’Acremont et al. 2003). (b’) is benchmark model for pure Newtonian rheology and local isostasy. The reference model f is shown with uplifts at different times. The major long wavelength surface uplift of 1600 m wavelength occurs at 0.95 my

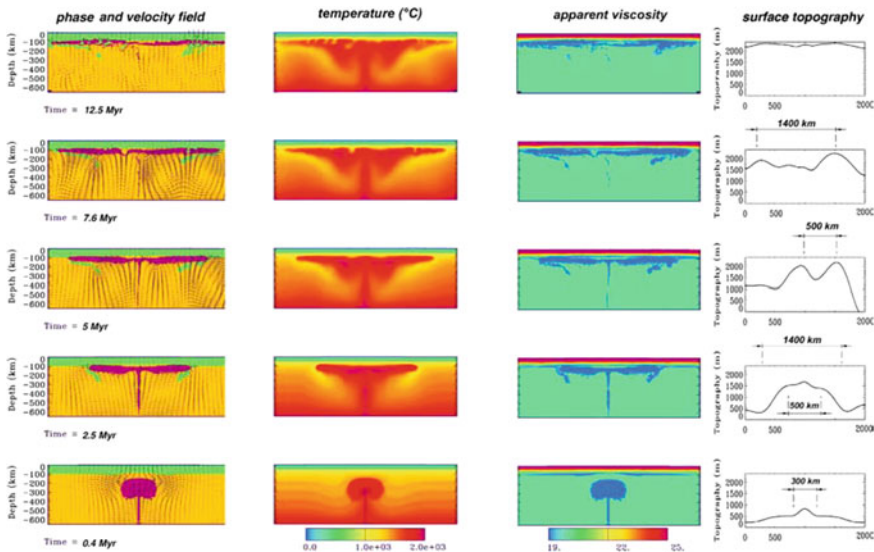


**Fig. 3.2** Deformation experiments in oceanic lithosphere with elastic-plastic-viscous rheology, Rayleigh number of  $10^5$ , temperature difference of 250 °C and background viscosity at depth  $\geq 10^{20}$  Pa s (Burov and Guillou-Frottier 2005). Shown from left to right are phase and velocity, temperature (°C), apparent viscosity (Pa s) and surface deformation (m). Color code for the phase field is: blue oceanic crust (7 km thick), green olivine lithosphere, yellow olivine/peridotite mantle, purple plume material. Each phase corresponds to a distinct set of rheological and physical properties

deformation wavelength at the expense of others, so that the surface topography is a superposition of deformations in the crust and mantle (Fig. 3.3). Laterally homogeneous, thin (100 km), elastic-plastic-viscous continental lithosphere with a thermal age of 150 my (Fig. 3.4) exemplifies this by showing the formation of a series of uplifts and basins instead of a large domal uplift, due to mechanical decoupling of the crust and mantle (Gerbault et al. 1998). Large scale extension and domal uplift of  $\sim 1200$  km long wavelength and  $<800$  m amplitude occurs during the initial phases of plume ascent. This takes place at less than 0.5 my after plume initiation, when the plume head is at a depth of 300–350 km in the mantle. The highest uplift of 1000 m occurs during 1–2.5 my after the plume initiation. Further evolution leads to the formation of alternate highs and basins of middle wavelength, represented by less than 300 km wavelength and 700–800 m elevation, which are superposed on the regional uplift. Following deformations lead to decoupling of the crust and mantle. Smaller 50–200 km crustal wavelengths interfere with larger 50–1000 m mantle wavelengths, depending on geothermal gradient and rheology. This produces a complex surface topography. In the final stages of surface evolution, a bimodal distribution of wavelengths can be identified: 20–80 m from crustal instabilities, and 200–400 m from deformation in the lithospheric mantle (Guillou-Frottier et al. 2007). However, in old cratonized lithosphere ( $\sim 400$  my thermal age), due to coupling of the crust and mantle, its strength increases, and the plate deforms as a single unit, producing long wavelength, small amplitude regional deformation.

Similar two-phase lithospheric uplift has also been reported by earlier studies (e.g., Monnereau et al. 1993; Davies 1994). They have documented an initial uplift of 500–700 m and a maximum uplift of 1300–1500 m.

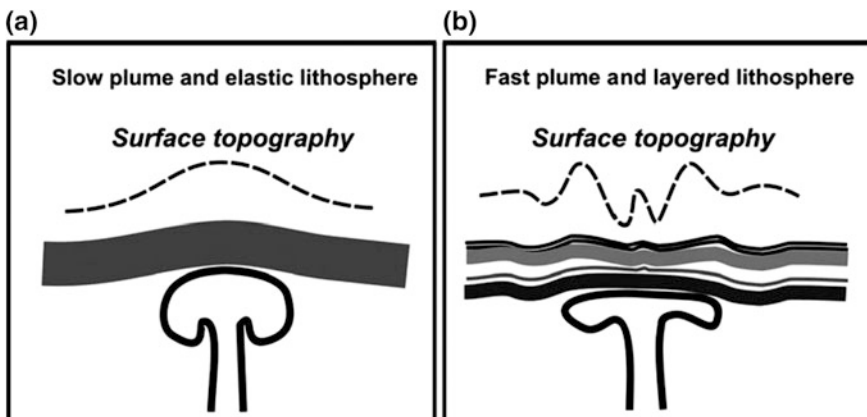


**Fig. 3.3** Plume-lithosphere interactions (Guillou-Frottier et al. 2007). **a** A slow plume impinging on an elastic lithosphere produces a single wavelength uplift. **b** Rheological stratification in the lithosphere results in the formation of topographic undulation

### 3.3 Timeframe and Factors for Dynamic Uplift

A generalized sequence of temporal events during plume-lithosphere interaction has been summarized based on the work of various authors (Griffiths et al. 1989; Campbell and Griffiths 1990; D’Acremont et al. 2003; Burov and Guillou-Frottier 2005; Guillou-Frottier et al. 2007). The description below is applicable to the oceanic lithosphere (Fig. 3.2), with differences in the continental lithosphere (Fig. 3.4) pointed out where applicable.

1. A broad regional uplift of  $\sim 1700$  m occurs after 0.1 (in less than 0.3–0.5) my of plume initiation, when the plume is at a depth of 300–350 km. A small central high of  $\sim 300$  km wavelength gets superposed over the regional uplift by 0.4 my. In the continental crust, large-scale extension follows a regional domal uplift of  $\sim 1200$  km and amplitude  $< 800$  m within the first 0.5 my.
2. By 0.95 my, the regional swell increases to  $\sim 1600$  km wavelength.

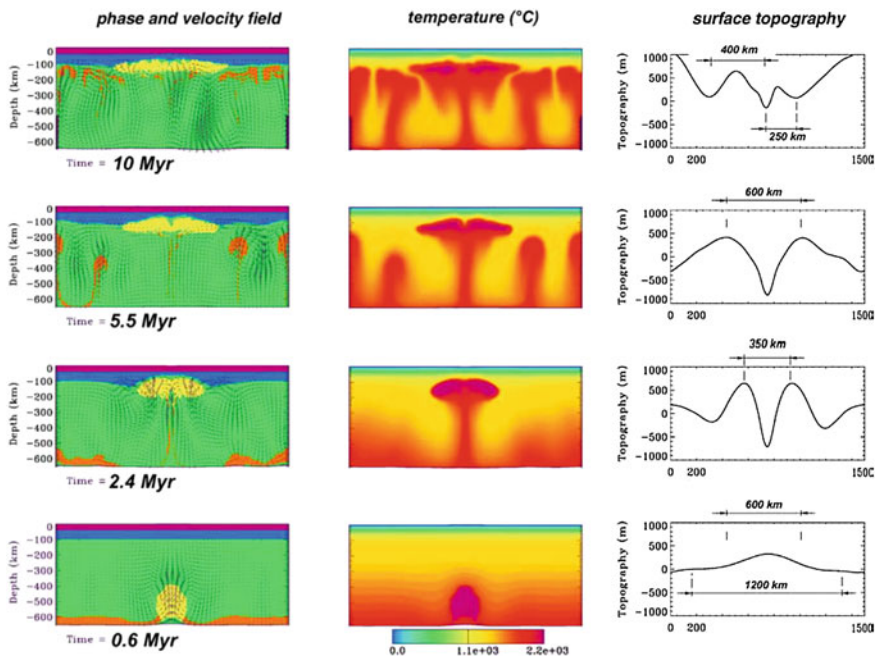


**Fig. 3.4** Deformation experiments in a thin tri-layered continental lithosphere with elastic-plastic-viscous rheology, thermal age of 150 my, Rayleigh number of  $10^6$  and background viscosity at depth  $\geq 5 \times 10^{19}$  Pa s (Burov and Guillou-Frottier 2005). Shown from left to right are phase and velocity, temperature ( $^{\circ}\text{C}$ ) and surface deformation (m). Color code for the phase field is: *purple* continental crust (40 km thick), *blue* olivine lithosphere, *green* olivine/peridotite mantle, *yellow* and *orange* plume material. Each phase corresponds to a distinct set of rheological and physical properties

3. The plume reaches the base of the lithosphere by 2.5 my, and begins to flatten out. A highest uplift of  $\sim 1800$  m is recorded at 1.4 my when the plume is at a depth of 150–200 km. The continental lithosphere, in contrast, shows a smaller highest uplift of 1000 m within 1–2.5 my.
4. By 2.5–5 my, thermo-mechanical erosion caused by the plume lead to sufficient destabilization of the lithosphere. It eventually starts to sag, forming alternate zones of extension and compression. In the continental realm, alternate highs and lows of  $<300$  km wavelength and 700–800 m amplitude form, superposed over the regional uplift by this time.
5. Further deformation in the continental crust leads to a complex topography due to interference of smaller, 50–200 km, crustal wavelengths with larger, 50–1000 m, mantle wavelengths.
6. Final thermal weakening of the lithosphere takes a long time of 10–20 to 50 my.

Based on the analysis of dynamic uplift by different authors (Olson and Nam 1986; Griffiths et al. 1989; D’Acremont et al. 2003; Burov and Guillou-Frottier 2005) the factors influencing the spatio-temporal development of the surface swell can be tabulated as follows:

1. Plume radius depends mostly on the height of rise (Eq. 3.9, Griffiths and Campbell 1990). Smaller radius leads to decreased wavelength of surface deformation due to concentrated flexure of the lithosphere (Burov and Guillou-Frottier 2005).
2. Plume depth is measured either in actual depth or spherical radius of the plume. It controls the temporal evolution of surface deformation.
3. Temperature anomaly between the plume and the surrounding material ( $\Delta T$  in Eq. 3.11; Hill 1991) is generally taken at a convenient constant value between 100 and 300 °C, but it may be upto 500 °C high (e.g., D’Acremont et al. 2003).
4. Lithospheric thickness controls the strength of the lithosphere and hence the wavelength of surface topography. Thickening reduces the Rayleigh number of the system and results in long wavelength, small amplitude surface deformation. Coupling between crust and mantle increases the effective strength further, leading to large-scale doming without any alternating basins. Thermo-mechanical erosion at the base of the lithosphere helps in the initiation of alternate highs and lows at the surface (Burov and Guillou-Frottier 2005).
5. Lithospheric density controls the buoyancy of the lithosphere and allows flattening and spreading of the plume.
6. Lithospheric age influences the model of isostasy, as well as coupling between crust and mantle. The wavelength of surface deformation depends on lithospheric flexure in addition to the plume radius, as inferred by D’Acremont et al. (2003) from intraplate deviatoric stresses.
7. Lithospheric rheology can be described by either elastic-plastic-viscous model or Newtonian model. It controls the surface topography. The topography is further controlled individual thicknesses of the crust and lithospheric mantle. They influence the resultant wavelength of the surface deformation by

superposition of deformation in the crust and mantle (Burov and Guillou-Frottier 2005).

8. Density contrast between lithosphere-asthenosphere and asthenosphere-plume ( $\lambda$  and  $\Delta\rho$  in Eq. 3.10; Griffiths et al. 1989). The plume-asthenosphere density contrast depends on  $\alpha$ , the coefficient of thermal expansion, and  $\Delta T$ , the temperature anomaly, which is taken to be constant. The plume maintains positive buoyancy for a long time after its flattening (D'Acremont et al. 2003).
9. Viscosity profile through the lithosphere-asthenosphere and asthenosphere-plume controls strain rate and thermo-mechanical erosion of the lithosphere (D'Acremont et al. 2003). However, Griffiths et al. (1989) state that viscosity contrasts is a less important factor.
10. Rayleigh number of the plume integrates the effect of viscosity, temperature and density contrasts between the plume and the surrounding, and controls the mode of heat transfer. Its value is generally taken as  $10^5$ – $10^6$  for upper mantle plume behavior (Burov and Guillou-Frottier 2005). It is less than that of the mantle, which ranges between  $10^6$  and  $10^8$ . Therefore, the primary mode of heat transfer is conduction.

### 3.4 Estimation of Dynamic Uplift

Inferring the magnitude of plume related uplift depends on the availability of data and timing of the uplift. A summary of different techniques used for estimation of timing of uplift and erosion is given by Anell et al. (2009; Table 1, p. 82). For present-day dynamic uplift, such as those in Iceland and North Atlantic, long wavelength free-air gravity anomaly and anomalous bathymetry of the affected ocean basin have been used successfully in estimating the amount of uplift. For past uplifts, such as those in Rockall-Faeroe-Shetland area, North Atlantic and Emeishan flood basalts, north-west China, the amount of dynamic support can be estimated from erosional removal of sediments. The erosional removal is measured from well logs, seismic thickness maps or from mass balance studies. It can be also estimated from paleo-topographic reconstructions or from anomalous subsidence history.

The North Atlantic region is presently dynamically supported by the Iceland plume, as evidenced by the anomalous bathymetry of the region. The topography anomaly can be calculated by subtracting the expected depth of the oceanic crust, determined from its age using a cooling plate model (e.g., Parsons and Sclater 1977; Stein and Stein 1992), from the observed bathymetry. Together with dynamic uplift, a component of uplift due to magmatic underplating, representing permanent uplift, occurs. The amount of permanent uplift needs to be separated from the total uplift to get the dynamic uplift. The amount of this permanent uplift can be estimated from wide-angle seismic data. The circum-Iceland region has an anomalous crust, which is 7–10 km thick (White 1997). This thickened crust accounts for a permanent uplift of 0–0.5 km (Jones et al. 2002), based on isostatic balancing. As

the anomalous topography variation is greater than the permanent uplift of 0.5 km (Fig. 3.5), the difference can be attributed to the dynamic support of the Iceland plume. The magnitude of dynamic support close to Iceland is 1.5–2 km, while the adjacent continental shelves in eastern Greenland and NW Europe are experiencing an uplift of at least 0.5 km. The dynamic topography is partially controlled by the active mid-ocean ridge system, as evidenced by the active Kolbeinsey Ridge being elevated higher than the extinct Aegir Ridge (Jones et al. 2002).

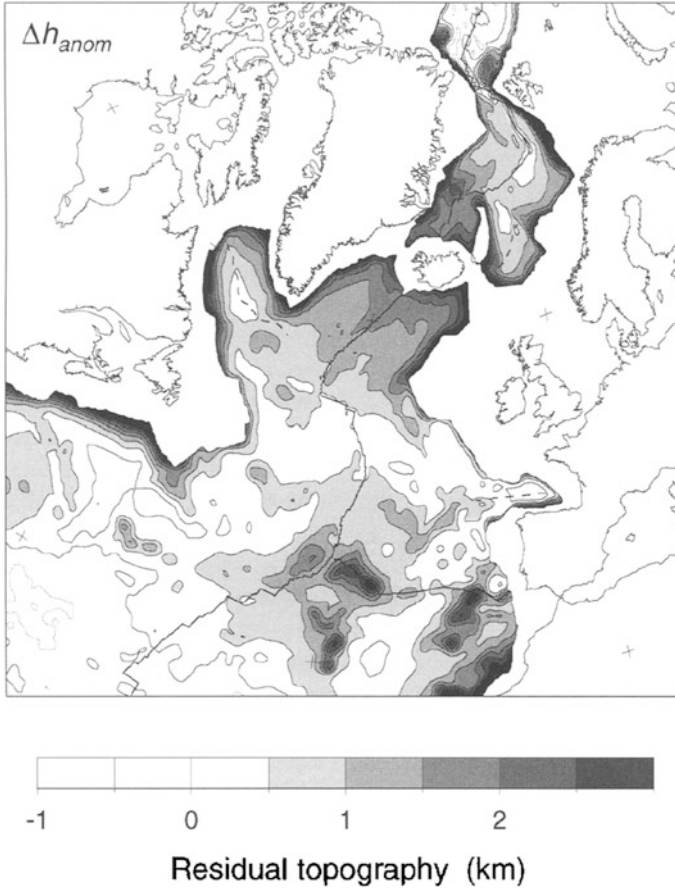


**Fig. 3.5** Anomalous topography of the North Atlantic Ocean, calculated by subtracting the age-depth cooling relationship of Parsons and Sclater (1977) from the ETOPO5 bathymetry grid (Jones et al. 2002). The age of oceanic lithosphere was taken from Müller et al. (1997). The Greenland-Iceland-Faroes Ridge was excluded from the calculation because its age is not well known. Anomalous topography is corrected for sediment loading of oceanic basement using the method of Le Douaran and Parsons (1982) and the sediment thickness map of Laske and Masters (1997). It should be noted that the anomalous topography displayed here contains both a component of present-day dynamic support and a permanent component caused by crustal thickness variations

Free air gravity anomaly can be used to estimate the dynamic uplift, as upwelling regions in the mantle are characterized by positive anomalies at the surface (Fig. 3.6). The gravity anomaly is related to the surface topography by the relation:

$$Z(k) = \Delta g(k)/H(k) \tag{3.12}$$

where  $Z(k)$  is the gravitational admittance, and  $\Delta g(k)$  and  $H(k)$  are the discrete Fourier transform of the gravity anomaly and the surface topography, respectively, in the wave-number ( $k$ ) domain, described earlier. Between wavelengths 500 and 3000 km, the admittance shows a linear relationship between gravity anomaly and topography:

$$\Delta h_{\text{conv}} = \Delta g/Z \tag{3.13}$$

where  $\Delta h_{\text{conv}}$  is the anomalous topography,  $\Delta g$  is the observed free air gravity anomaly, and  $Z$  is the admittance. The admittance value is taken as 35 mGal km<sup>-1</sup> for sub-aqueous and 50 mGal km<sup>-1</sup> for sub-aerial topographies.

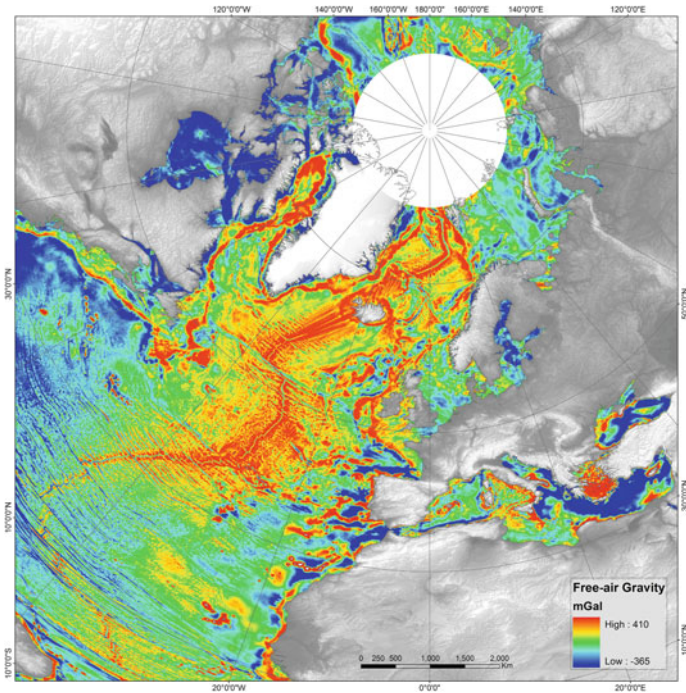


**Fig. 3.6** Free-air gravity anomaly over part of the northern hemisphere, showing long-wavelength gravity high centered on Iceland. The map is displayed using a polar Lambert azimuthal equal area projection. Gravity anomaly data from Sandwell and Smith (2009)

In the North Atlantic region, the dynamic support estimates from the gravity anomaly give reasonable agreement with that from the topography (Fig. 3.7). The dynamic support in Iceland is 1.8 km, while the surrounding continental margins are experiencing a support of 0.5–1 km. This support seems to be absent in the North Sea and southern England (Jones et al. 2002).

The proto-Iceland plume has also affected the Paleocene sedimentation of the North Atlantic margins, as evidenced by accelerated tectonic subsidence in the North Sea accompanied by uplift and erosion of the surrounding areas (Thompson 1974; Brodie and White 1995; Faleide et al. 2002). This event is synchronous with the deposition of Paleocene sandstone reservoirs along the Faeroe-Shetland basin (White and Lovell 1997; Naylor et al. 1999) and major magmatic events at 59 and 55 my (White and Lovell 1997; Ritchie et al. 1999). Geochemical studies of basalts from the British Cenozoic volcanic province indicate 70 % fractional crystallization (Thompson 1974), the residual of which should remain at depth. Geo-barometric studies indicate a pressure of 1 GPa, corresponding to a depth of 30 km (Thompson 1974; Brodie and White 1995), giving rise to magmatic underplating at the Moho. This is verified by wide angle seismic studies, indicating the presence of a high velocity zone near the Moho (Barton and White 1997).

A large amount of data on the Cenozoic erosion of Britain and Ireland is currently available. The data are derived from subsidence modeling, vitrinite reflectance, apatite fission-track and sonic velocity data. The amount of surface erosion is

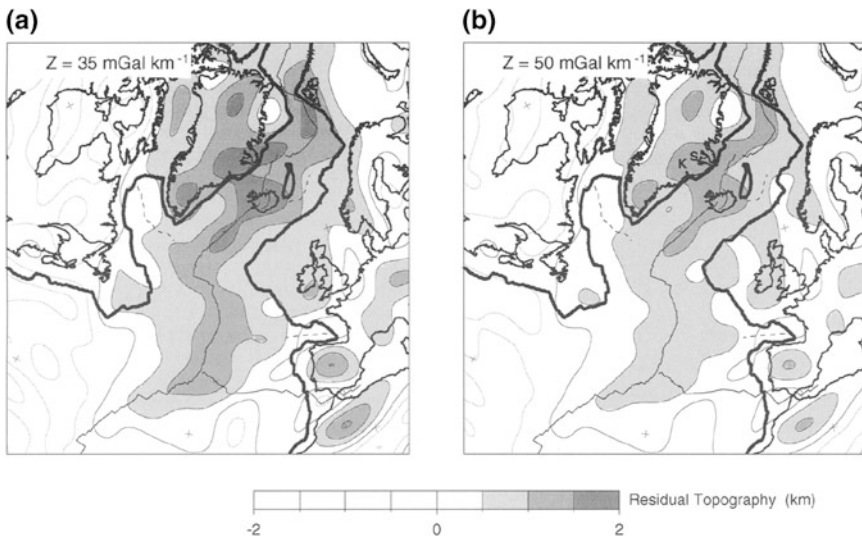


**Fig. 3.7** Estimates of present day dynamic support in the North Atlantic region, calculated by dividing the long wavelength free-air gravity anomaly by a constant admittance (Jones et al. 2002). *Bold continuous lines* indicate continent-ocean boundaries. **a** Dynamic support predicted using an admittance,  $Z$ , of  $35 \text{ mGal km}^{-1}$ . **b** dynamic support predicted using an admittance,  $Z$ , of  $50 \text{ mGal km}^{-1}$ . *K* Kangerlussuaq, *S* Scoresby Sund

mapped in the surrounding basins based on the above datasets (Fig. 3.8). It shows an erosional peak over north-west England amounting to 1–2.5 km, which gradually decreases towards the offshore (Jones et al. 2002). As the time between the beginning of the erosional event and that of the corresponding offshore sediment flux is less than 100 ka (Reading 1991; Burgess and Hovius 1998), an increase in sedimentation is directly correlatable with the surface uplift. Calculation of Paleogene sediment flux in the North Sea and Faroe-Shetland basins shows an increase during Paleocene, maximum at 59–58 my and then a gradual decrease over 10–20 my interval during Eocene (Reynolds 1994; Clarke 2002; Jones and White 2003), which is directly correlated with the epirogenic uplift by the proto-Iceland plume (Jones et al. 2002).

Forward modeling of paleo-topography can be carried out after correcting for magmatic underplating, which results in a permanent uplift, sea level changes and erosional correction (Jones and White 2003). The erosional correction is given by:

$$T_D = T_0 + E(\rho_a - \rho_s)/\rho_a \quad (3.14)$$

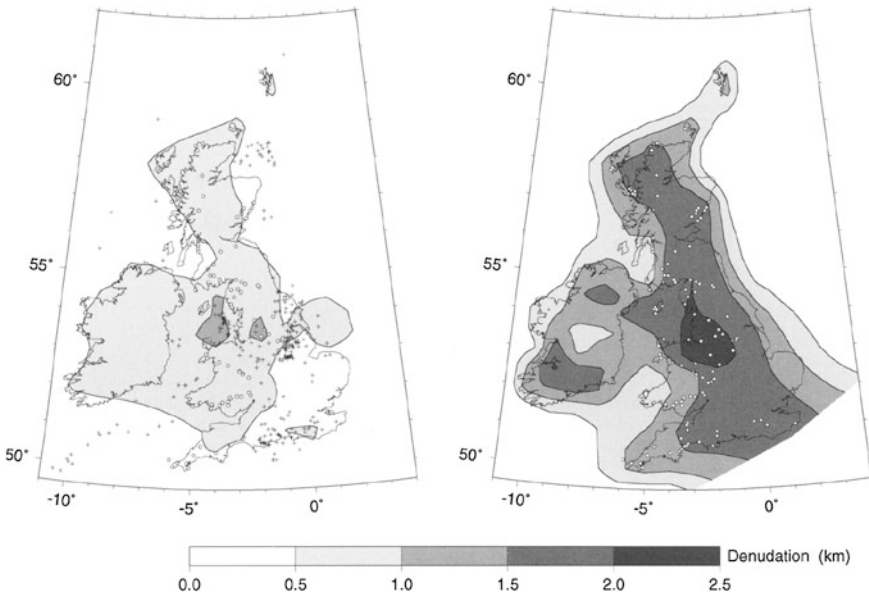


**Fig. 3.8** Estimates of Cenozoic denudation for Britain and Ireland based on modeling subsidence histories and apatite fission-track length distributions (Jones et al. 2002). + denotes locations of well section used for subsidence modeling. O denoted locations of apatite samples. **a** Minimum denudation estimate found by contouring results derived from subsidence analysis, the lower bounds of the Rowley (1998) denudation estimates derived from modeling apatite fission track length distributions, and the minimum denudation estimate for Ireland of Allen et al. (2002). **b** Maximum denudation estimate found by contouring the modes of the Rowley (1998) denudation estimates and the maximum denudation estimate for Ireland of Allen et al. (2002)

where  $T_D$  is the corrected topography,  $T_0$  is the starting topography,  $E$  is the erosion,  $\rho_a$  is the asthenospheric density, given usually as  $3.2 \text{ kg m}^{-3}$ , and  $\rho_s$  is the average density of the eroded sediments, represented by  $2.4 \text{ kg m}^{-3}$ .

After correction, the modeled coastline can be compared with that observed in seismic images, interpreted from deltaic progradations of the respective intervals. The best-fitting dynamic-support profile can be estimated by minimizing the misfit between the seismically-determined and modeled coastlines (Fig. 3.9).

The magnitude of the dynamic uplift can also be quantified from subsidence analysis (see Chap. 4). The process involves comparing the depth of post-rift marker horizons having well-constrained depth data, with expected post-rift subsidence, calculated from lithospheric stretching models. The difference, excluding permanent uplift, gives the dynamic support (Fig. 3.10a, b). Similar studies in oceanic crust look for anomalous subsidence by comparing the depth of the back-stripped basement at each age with a calculated subsidence curve. The method is fully described in Ito and Clift (1998). However, Clift (2005), by following the same procedure, had suggested no anomalous subsidence due to plumes. In general, the dynamic support estimates from paleo-topographic reconstructions are in reasonable agreement with those from subsidence anomalies. This verifies both the sets of calculations. The result of subsidence analysis shows a peak uplift of 0.5 km in north-west England, which decreases to zero towards south-east (Nadin et al. 1997; Jones 2000; Jones et al. 2001; Jones and White 2003) (Fig. 3.10c). A consequent

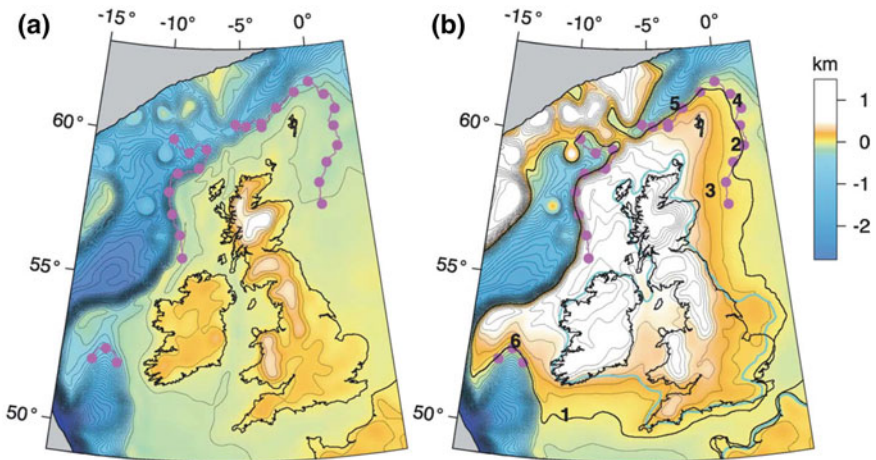


**Fig. 3.9** **a** Present topography (from ETOPO5), low-pass filtered at 50 km to leave isostatically compensated topography with contour interval of 100 m (Jones and White 2003). *Pink spots* latest Paleocene coastline recognized as break between delta topsets and foresets on seismic and well-log data; *grey* oceanic crust. Projection is stereographic. **b** Latest Paleocene topographic reconstruction calculated by applying three corrections to present topography: (i) global sea-level rise of 100 m, (ii) denudation correction, and (iii) best-fit dynamic-support profile required to match observed and predicted coastlines. *Black line* predicted coastline after applying all three corrections; *blue line* coastline predicted by applying sea-level and denudation corrections only

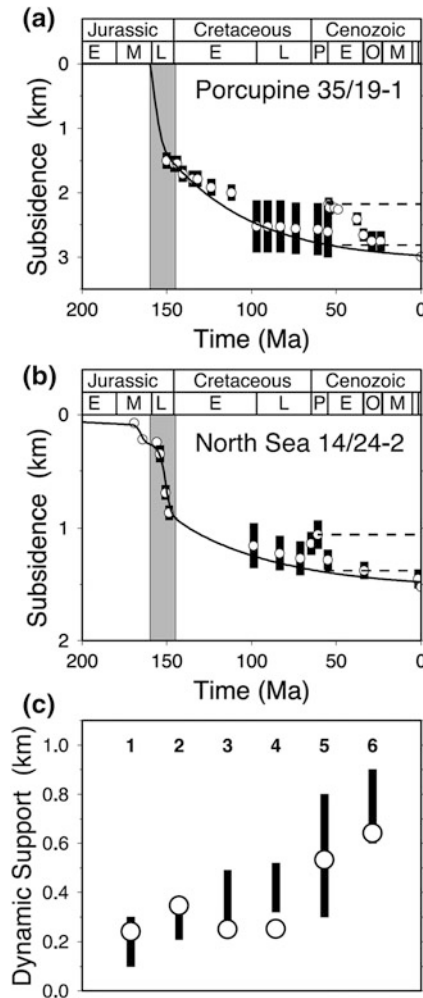


**Fig. 3.10** a, b 1D subsidence plots to demonstrate estimation of latest Paleocene peak dynamic support from stratigraphy of Porcupine Basin and the Outer Moray Firth, North Sea Basin (Jones and White 2003). Circles back-stripped stratigraphy, bars uncertainty in depositional water depth. Theoretical subsidence curve is fitted to syn-rift stratigraphy assuming lithospheric pure shear stretching. Post-rift curve forward modeled assuming no further stretching. Grey shading syn-rift period constrained by seismic reflection profiles. Dashed lines illustrate subsidence anomaly interpreted as a latest Paleocene peak in dynamic support. c Comparison of latest Paleocene dynamic support estimates from subsidence analysis with those from fitting coastlines. Black bars estimates from subsidence analysis at numbered locations marked on Fig. 3.9b (1 Fastnet Basin, 2 South Viking Graben, 3 Witch Ground Graben, 4 North Viking Graben, 5 Faroe-Shetland Basin, 6 Porcupine Basin). Values adjusted by including Cenozoic global sea-level fall of 100 m. Circles estimates from fitting coastlines at these locations

regression-transgression cycle is observed in the surrounding basins with peak regression corresponding to the Upper Flett Formation, deposited during earliest Eocene (Milton et al. 1990; Ebdon et al. 1995, Nadin et al. 1997; Jones et al. 2001).

Direct estimate of dynamic support can be obtained from the amount of erosion of a widespread sedimentary unit, as it is shown in the case of the Maokou Formation underlying the Emeishan flood basalts in south-west China (He et al. 2003). Systematic biostratigraphic correlation and examination of 67 sections of the Maokou Formation shows a progressive thinning towards the centre of the flood basalt province (Fig. 3.11), where only the lowermost of the three biostratigraphic zones is present. The contact between the basalts and the sedimentary unit is an unconformity, containing relict gravels and basal conglomerates from the uppermost biozone of the Maokou Formation, as well as karst relief and paleosols,

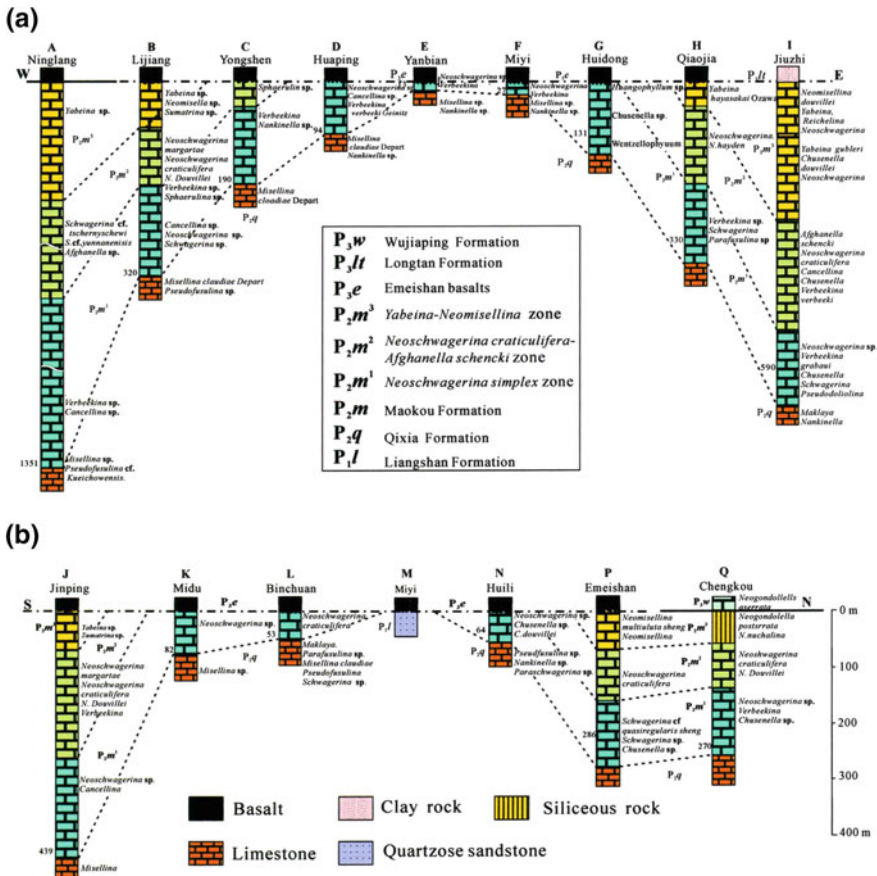


Fig. 3.11 Biostratigraphic correlation of the Maokou Formation in the Emeishan igneous province (He et al. 2003). **a** West-east oriented profile A–I cut through the Emeishan basaltic province. **b** Profile K–R, south-north oriented traverse across the province. The number near every section is the thickness of the Maokou Formation

indicating differential erosion due to regional uplift. Biostratigraphic and erosional analysis indicates a rapid crustal uplift in less than 3 my. The uplifted condition continues for 1.0–2.5 my, during which 300 m of Maokou limestone have been eroded in the center of the province. Based on maximum thickness of conglomerate layers and underlying basalts, and possible maximum thickness of the eroded strata, which is about 500 m, the total uplift is estimated to be over 1000 m, giving a plume head temperature of 1450–1500 °C (He et al. 2003).

## References

- Allen EA, Cunningham MJM, Bennett SD, 6 others (2002) The post-Variscan thermal and denudational history of Ireland. In: Dore AG, Cartwright JA, Stoker MS, Turner JP, White N (eds) Exhumation of the north atlantic margin: timing, mechanisms, and implications for petroleum exploration. Geological Society of London, Special Publications, London, pp 371–399
- Anell I, Thybo H, Artemieva IM (2009) Cenozoic uplift and subsidence in the North Atlantic region: geological evidence revisited. *Tectonophysics* 474:78–105
- Barton AJ, White RS (1997) Crustal structure of Edoras Bank continental margin and mantle thermal anomalies beneath the North Atlantic. *J Geophys Res* 102(B2):3109–3129
- Bauer SJ, Handin J (1983) Thermal expansion and cracking of three confined, water-saturated igneous rocks to 800 °C. *Rock Mech Rock Engg* 16:181–198
- Brodie J, White N (1995) The link between sedimentary basin inversion and igneous underplating. In: Buchanan JG, Buchanan PG (eds) Basin inversion. Geological Society of London, Special Publications 88, pp 21–38
- Burgess PM, Hovius N (1998) Rates of delta progradation during highstands; consequences for timing of deposition in deep-marine systems. *J Geol Soc London* 155(Part 2):217–222
- Burov E, Guillou-Frotier L (2005) The plume head-continental lithosphere interaction using a tectonically realistic formulation for the lithosphere. *Geophys J Int* 161:469–490
- Campbell IH (2006) Large igneous provinces and the mantle plume hypothesis. *Elements* 1:265–269
- Campbell IH, Griffiths RW (1990) Implications of mantle plume structure for the origin of flood basalts. *Earth Planet Sci Lett* 99:79–93
- Clarke BJ (2002) Early Cenozoic denudation of the British Isles: a quantitative stratigraphic approach. University of Cambridge, Cambridge
- Clift PD (2005) Sedimentary evidence for moderate mantle temperature anomalies associated with hotspot volcanism. In: Foulger GR, Natland JH, Presnall DC, Anderson DL (eds) Plates, plumes, and paradigms. Geological Society of America Special Paper 388, pp 279–287
- Cooper HW, Simmons G (1977) The effect of cracks on the thermal expansion of rocks. *Earth Planet Sci Lett* 36:404–412
- D'Acremont E, Leroy S, Burov EB (2003) Numerical modeling of a mantle plume: the plume head-lithosphere interaction in the formation of an oceanic large igneous province. *Earth and Planet Sci Lett* 206:379–396
- Davies GF (1994) Thermomechanical erosion of the lithosphere by mantle plumes. *J Geophys Res* 99(B8):15709–15722
- Ebdon CC, Granger PJ, Johnson HD, Evans AM (1995) Early Tertiary evolution and sequence stratigraphy of the Faeroe-Shetland Basin: implications for hydrocarbon prospectivity. In: Scrutton RA, Stoker MS, Shimmield GB, Tudhope AW (eds) the tectonics, sedimentation and palaeoceanography of the North Atlantic Region. Geological Society of London, Special Publications 90, pp 51–69

- Faleide JJ et al (2002) Tectonic impact on sedimentary processes during Cenozoic evolution of the northern North Sea and surrounding areas. In: Dore AG, Cartwright JA, Stoker MS, Turner JP, White N (eds) *Exhumation of the North Atlantic Margin: timing, mechanisms, and implications for petroleum exploration*. Geological Society of London, Special Publications, pp 235–269
- Gerbault M, Poliakov ANB, Daignières M (1998) Prediction of faulting from the theories of elasticity and plasticity; what are the limits? *J Struct Geol* 20:301–320
- Griffiths RW, Campbell IH (1990) Stirring and structure in mantle starting plumes. *Earth Planet Sci Lett* 99:66–78
- Griffiths RW, Gunris M, Eitelberg G (1989) Holographic measurements of surface topography in laboratory models of mantle hotspots. *Geophys J* 96:477–495
- Guillou-Frottier L, Burov E, Nehlig P, Wyns R (2007) Deciphering plume–lithosphere interactions beneath Europe from topographic signatures. *Glob Planet Change* 58:119–140
- He B, Xu Y-G, Chung S-L, Xiao L, Wang Y (2003) Sedimentary evidence for a rapid, kilometer-scale crustal doming prior to the eruption of the Emeishan flood basalts. *Earth Planet Sci Lett* 213:391–405
- Hill RI (1991) Starting plumes and continental break-up. *Earth Planet Sci Lett* 104:398–416
- Ito G, Clift PD (1998) Subsidence and growth of Pacific Cretaceous plateaus. *Earth Planet Sci Lett* 161:85–100
- Jones SM (2000) Influence of the Iceland Plume on Cenozoic sedimentation patterns. PhD dissertation, University of Cambridge
- Jones SM, White N (2003) Shape and size of the starting Iceland plume swell. *Earth Planet Sci Lett* 216:271–282
- Jones SM, White N, Lovell B (2001) Cenozoic and Cretaceous transient uplift in the Porcupine Basin and its relationship to a mantle plume. In: Shannon PM, Haughton PDW, Corcoran D (eds) *The petroleum exploration of Ireland's offshore basins*. Geological Society of London, Special Publications 188, pp 345–360
- Jones SM, White N, Clarke BJ, Rowley E, Gallagher K (2002) Present and past influence of the Iceland Plume on sedimentation. In: Dore AG, Cartwright JA, Stoker MS, Turner JP, White N (eds) *Exhumation of the North Atlantic Margin: timing, mechanisms, and implications for petroleum exploration*. Geological Society of London Special Publications, pp 13–25
- Laske G, Masters A (1997) A global digital map of sediment thickness. *EOS Transactions, American Geophysical Union* 78 (F483)
- Le Douaran S, Parsons B (1982) A note on the correction of ocean floor depths for sediment loading. *J Geophys Res* 87:4715–4722
- Loper DE, Stacey FD (1983) The dynamical and thermal structure of deep mantle plumes. *Phys Earth Planet Inter* 33:304–317
- Milton NJ, Bertram GT, Vann IR (1990) Early Paleogene tectonics and sedimentation in the central North Sea. In: Hardman RFP, Brooks J (eds) *Tectonic events responsible for Britain's oil and gas reserves*. Geol Soc Spec Publ, London, pp 339–351
- Monnereau M, Rabinowicz M, Arquis E (1993) Mechanical erosion and reheating of the lithosphere: a numerical model for hotspot swells. *J Geophys Res* 98:809–823
- Müller RD, Roest WR, Royet J-Y, Gahagan LM, Sclater JG (1997) Digital isochrons of the world's ocean floor. *J Geophys Res* 102:3211–3214
- Nadin PA, Kusznir NJ, Cheadle MJ (1997) Early tertiary plume uplift of the North Sea and Faeroe-Shetland basins. *Earth Plan Sci Lett* 148(1–2):109–127
- Naylor PH, Bell BR, Jolley DW, Dumall P, Fredsted R (1999) Palaeogene magmatism in the Faeroe-Shetland Basin; influences on uplift history and sedimentation. In: Fleet AJ, Boldy SAR (eds) *5th conference on petroleum geology of Northwest Europe*, London, pp 545–558
- Olson P, Nam IS (1986) Formation of seafloor swells by mantle plumes. *J Geophys Res* 91:7181–7191
- Parsons B, Sclater JG (1977) An analysis of the variation of ocean floor bathymetry and heat flow with age. *J Geophys Res* 82(5):803–827

- Reading HG (1991) The classification of deep-sea depositional systems by sediment calibre and feeder system. *J Geol Soc London* 148(3):427–430
- Reynolds T (1994) Quantitative analysis of submarine fans in the Tertiary of the North Sea Basin. *Mar Pet Geol* 11(2):202–207
- Ribe NM (1996) The dynamics of plume-ridge interaction, 2. off-ridge plumes. *J Geophys Res* 101:16195–16204
- Ribe NM, Christensen UR (1994) Three-dimensional modeling of plume-lithosphere interaction. *J Geophys Res B* 99:669–682
- Ritchie JD, Gatliff RW, Richards PC (1999) Early Tertiary magmatism in the offshore NW UK margin and surrounds. In: Fleet AJ, Boldy SAR (eds) 5th conference on petroleum geology of Northwest Europe, London, pp 573–584
- Rowley EJ (1998) Quantifying Cenozoic exhumation across the British Isles. PhD dissertation, University of Cambridge
- Sandwell DT, Smith WHF (2009) Global marine gravity from retracked Geosat and ERS-1 altimetry: ridge segmentation versus spreading rate. *J Geophys Res* 114(B0141)
- Stein CA, Stein S (1992) A model for the global variation in oceanic depth and heat flow with lithospheric age. *Nature* 359:123–129
- Thompson RN (1974) Primary basalts and magma genesis, I: Skye, Northwest Scotland. *Contrib Miner Petrol* 45:317–341
- Weinberg RF, Podladchikov Y (1994) Diapiric ascent of magmas through power law crust and mantle. *J Geophys Res* 99:9543–9559
- White N, Lovell B (1997) Measuring the pulse of a plume with the sedimentary record. *Nature* 387(6636):888–891
- Whitehead JA, Luther DS (1975) Dynamics of laboratory diapir and plume models. *J Geophys Res* 80:705–717

# Chapter 4

## Permanent Crustal Uplift Due to Plume Activity

### 4.1 Plume-Related Volcanism

Impingement of a mantle plume below the lithosphere results in a flood basalt province. Typically, the provinces has a short eruption time, less than 1 my, and high eruption rate, one to two orders of magnitude higher than the associated hotspot trail (Richards et al. 1989). This fits well with the premise that the flood basalts are the result of plume-head melting, while the hotspot track is produced by the plume tail (Campbell and Davies 2006). Plume-head melting occurs due to adiabatic decompression when the head reaches the base of the lithosphere, sometime after the time of the maximum dynamic uplift (Campbell and Griffiths 1990).

### 4.2 Permanent Uplift

Permanent uplift occurs due to isostatic uplift of the crust during emplacement of magmatic bodies (Brodie and White 1994, 1995; Clift 1997; White and Lovell 1997; Clift and Turner 1998). Basaltic melts have density values between those of lower crust and lithospheric mantle. This results in the uprise of the magma through the mantle and ponding at the base of the crust, giving rise to magmatic underplating. In the process, the melt displaces denser mantle material, resulting in isostatic uplift of the crust. Assuming Airy isostasy, the uplift is given by (Watts 2001):

$$\begin{aligned} u &= v(1 - \rho_x/\rho_a) && \text{(subaerial)} \\ \text{and } u &= v(\rho_a - \rho_x)/(\rho_a - \rho_w) && \text{(submarine)} \end{aligned} \quad (4.1)$$

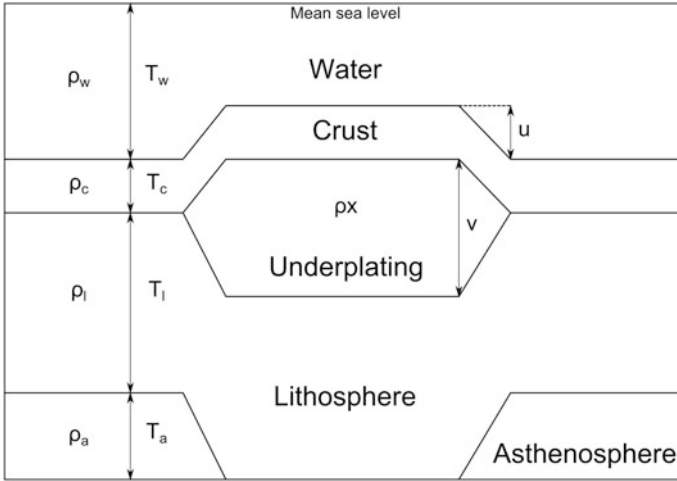


**Fig. 4.1** Crustal model showing magmatic underplating (modified from Watts 2001)

where  $u$  is the crustal uplift,  $v$  is the thickness of the underplated material, and  $\rho_x$ ,  $\rho_a$  and  $\rho_w$  are the densities of the underplated material, asthenosphere, and water, respectively (Fig. 4.1).

If we take into account the erosional removal of uplifted material, the thickness of underplating required to have a denudation,  $D$ , is given by (White and Lovell 1997):

$$v = (\rho_a - \rho_s) / (\rho_a - \rho_x) D + (\rho_a) / (\rho_a - \rho_x) T + (\rho_a - \rho_w) / (\rho_a - \rho_x) W \quad (4.2)$$

where  $T$  is the present day (residual) topography (equal to  $u$  for no erosion),  $\rho_s$  is the density of the eroded sediments, and  $W$  is the water depth before uplift.

The strength of the crust may produce a broad flexural uplift, instead of a local isostatic uplift, which is given by (Watts 2001):

$$U(k) = V(k) (\rho_a - \rho_x) / (\rho_a - \rho_w) \Phi_e(k) \quad (4.3)$$

where  $U(k)$  and  $V(k)$  are the discrete Fourier transforms of  $u$  and  $v$  in the wave-number,  $k$ , domain, and  $\Phi_e(k) = \{1 + Dk^4 / (\rho_a - \rho_w)g\}^{-1}$  (Eq. 1.16, with  $\rho_a$  and  $\rho_w$  instead of  $\rho_m$  and  $\rho_{\text{fill}}$ , respectively).

### 4.2.1 Factors for Permanent Uplift

From Eqs. 4.1–4.3, it can be observed that the amount of permanent uplift depends on the thickness of the underplated material, as well as on the densities of asthenosphere, water and underplated material. During the process, these densities are assumed to remain relatively constant ( $\rho_a = 3200$ ,  $\rho_x = 2900$ , basalt,  $\rho_s = 2600$  and  $\rho_w = 1030 \text{ kg m}^{-3}$ ), while the only factor that varies is the thickness of the underplated material.

### 4.2.2 Identification and Estimation of Permanent Uplift

Magmatic underplating can be identified independently from seismic (seismic reflection/refraction/velocity), geologic (subsidence analysis), or petrologic (magma evolution) studies. The magnitude of uplift and thickness of magmatic underplating are related to each other by isostatic Eqs. 4.1–4.3, where knowing one enables the calculation of the other.

Magmatic underplating is an important feature of large igneous provinces. Seismic data are consistently used to identify the presence of crustal thickening and high velocity layers at the base of the crust. These layers have velocities which are intermediate between those characterizing the crust and mantle, in the  $7\text{--}8 \text{ km s}^{-1}$  interval. These velocities are commonly interpreted as results of magmatic underplating (Kelemen and Holbrook 1995; Farnetani et al. 1996; Trumbull et al. 2002). Deep seismic reflection studies have been employed to identify the crustal thickness in the late Permian Emeishan large igneous province in south-west China (Xu and He 2007). It was observed that there is a gradual thinning of the crust from the centre to the periphery, varying from 55 to 64 km (average 61.5 km, with  $\sim 20$  km thick high velocity lower crust) in the centre to 38–54 km (average 45 km) in the eastern part. Beyond the igneous province, the crust is 35–45 km thick. Seismic studies indicate a heterogeneous crustal structure with the presence of three anomalous high velocity bodies (Fig. 4.2):

1. the upper crust one having velocity between  $6.0$  and  $6.6 \text{ km s}^{-1}$ ,
2. the crust mantle boundary one between  $7.1$  and  $7.8 \text{ km s}^{-1}$ , and
3. the upper mantle one between  $8.3$  and  $8.6 \text{ km s}^{-1}$ .

Similar velocity anomalies at the crust-mantle boundary and in the upper mantle are observed in different large igneous provinces around the world (e.g., Columbia plateau with  $8.4 \text{ km s}^{-1}$ , Catching and Mooney 1988; Rhine graben with  $8.3\text{--}8.4 \text{ km s}^{-1}$ , Zucca 1984; Ontong Java Plateau with  $8.6 \text{ km s}^{-1}$ , Furumoto et al. 1976).

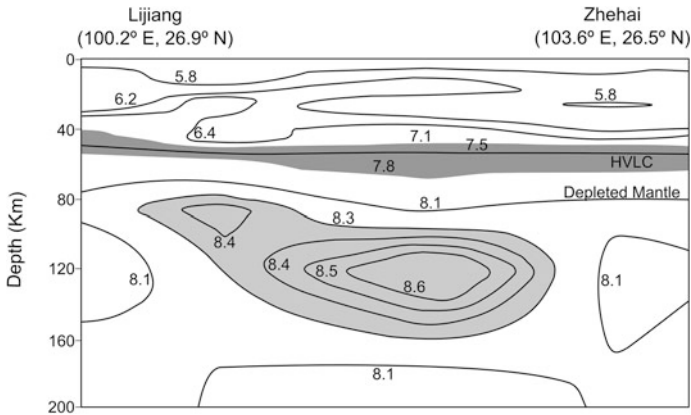


**Fig. 4.2** Seismic tomographic velocity structure of the crust and upper mantle beneath the Emeishan large igneous province between Lijiang to Zhehai (modified from Xu and He 2007)

Farnetani et al. (1996) suggested that the presence of a high velocity lower crust together with a high upper crustal velocity is diagnostic of deep melting and an essential part of plume emplacement. The high velocity lower crust is interpreted as a result of magmatic underplating produced from cumulates during fractional crystallization of an initial picritic melt, while the upper mantle anomaly represents the residuum after melt extraction from the plume head. Similar studies in the Mahanadi delta region of eastern India by Behera et al. (2004) suggest the presence of a 10 km thick high velocity ( $7.5 \text{ km s}^{-1}$ ) and high density layer ( $3.05 \text{ g cm}^{-3}$ ) at the base of the crust, presumably due to underplating.

Subsidence analysis can effectively be used to estimate the magnitude of permanent uplift in oceanic crust (e.g., Clift and Turner 1998; Ito and Clift 1998; Clift 2005). The method involves comparing tectonic subsidence curves estimated from well data with calculated subsidence curves. In a particular location, the deposition depth for each stratigraphic unit is obtained from biostratigraphic data. The tectonic subsidence of the basement is calculated at each time stage as corresponding to the time of deposition of each stratigraphic unit by the backstripping method of Sclater and Christie (1980). In this method the sediment load is subtracted at each stage, and the isostatically uplifted depth of the basement is noted, assuming either Airy or flexural isostasy, usually neglecting sea level fluctuations. The backstripped depth of the basement, using Airy isostasy, is given by (Steckler and Watts 1978)

$$Y = W_d + S^*(\rho_m - \rho_s)/(\rho_m - \rho_w) + \Delta_{sl}(\rho_m)/(\rho_m - \rho_w) \quad (4.4)$$

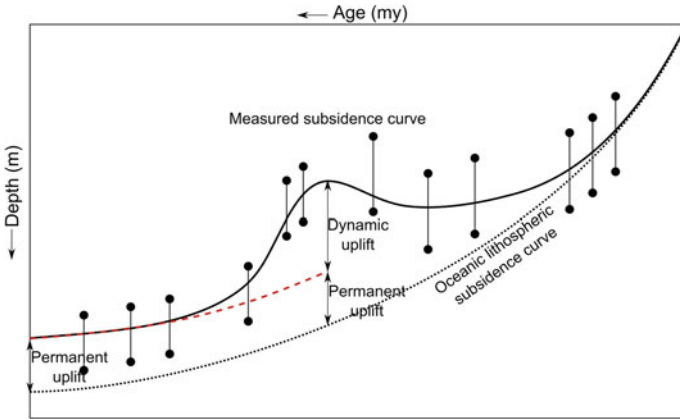


**Fig. 4.3** Age-depth relationship between a normal and a plume-affected oceanic crust

where  $W_d$  and  $\Delta_{sl}$  are the water depth and sea-level height, respectively, at a particular time,  $S^*$  is the total sediment thickness, and  $\rho_m$ ,  $\rho_s$  and  $\rho_w$  are the mantle, seawater and average sediment densities, respectively.

The resultant basement tectonic subsidence curve is compared with calculated seafloor subsidence curve (Parsons and Sclater 1977; Stein and Stein 1992). For past plume activity, the anomalous present-day depth values indicate permanent uplift, while anomalous past subsidence indicates the presence of dynamic uplift. The magnitudes of the respective uplifts can be directly estimated from the difference between the expected and observed depth values (Fig. 4.3). The method has been successfully used for the hotspot tracks around the world, particularly in the Pacific and North Atlantic (Ito and Clift 1998; Clift 2005; Fig. 4.4). Similar method has been used in case of continental regions (e.g., Clift and Turner 1998) using lithospheric stretching curves (McKenzie 1978; Jarvis and McKenzie 1980; Fig. 4.5).

In addition to these methods, geochemical analysis can be used to estimate the depth at which fractional crystallization of parent magma must occur to match the residual liquid forming the flood basalts (e.g., Thompson 1974; Farnetani et al. 1996; Xu and He 2007). P-wave velocity can be used to constrain the composition of the cumulate layer, and a petrologic program can be used to calculate magmatic evolution trends at different pressure (Table 4.1). Matching the result with the geochemical signature of surface basalts provides a genetic link with the observed

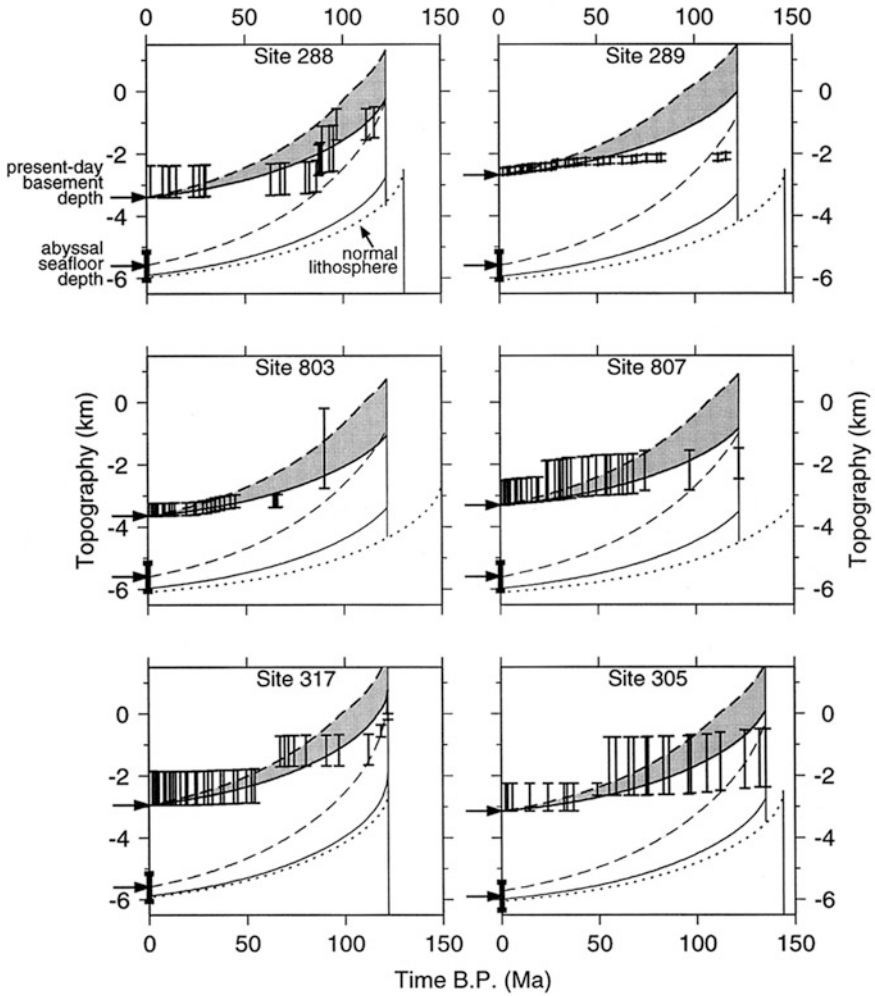


**Fig. 4.4** Thermal subsidence predictions compared with reconstructed basement depths (vertical bars) at different drill sites (288, 289, 803, 807—Ontong Java Plateau, 317—Manihiki Plateau, 305—Shatsky Rise) (Ito and Clift 1998)

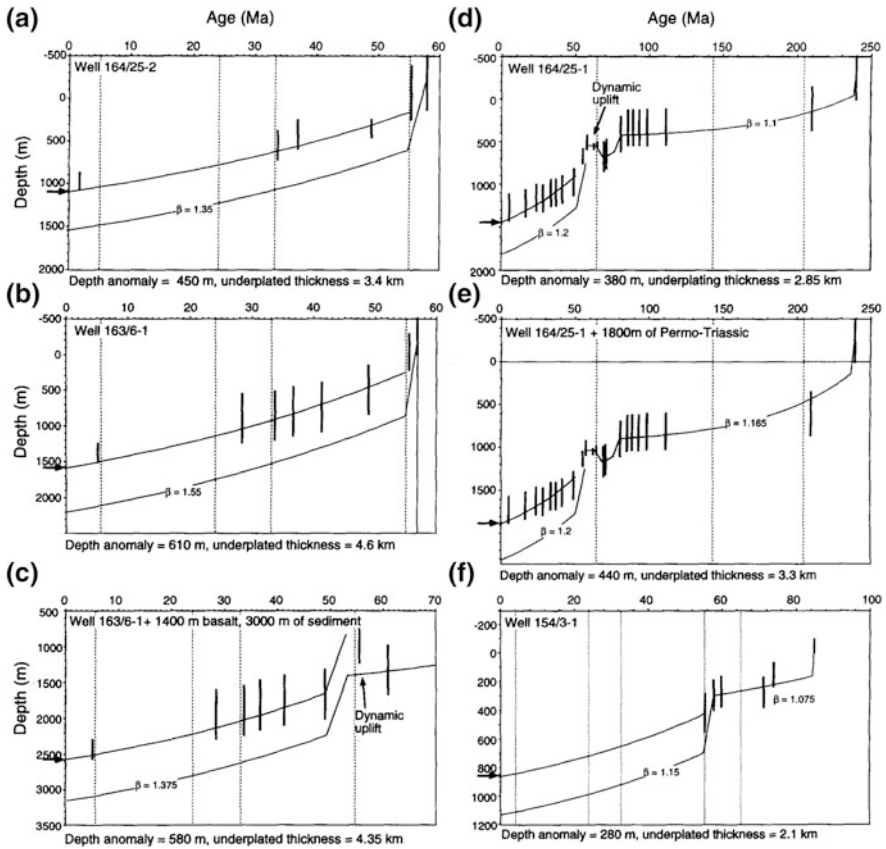


**Fig. 4.5** Reconstructed basement tectonic subsidence curves in the northern Rockall Trough, North Atlantic (Clift and Turner 1998)

velocity anomalies at depth. The MgO content of the basalt is particularly diagnostic, and can be used to estimate the pressure, and the depth, at which fractionation took place.

**Table 4.1** Calculated results of fractionation at different pressures (modified after Xu and He 2007)

	SiO <sub>2</sub>	TiO <sub>2</sub>	Al <sub>2</sub> O <sub>3</sub>	FeO	MgO	CaO	Na <sub>2</sub> O	K <sub>2</sub> O	Proportion of fractionated minerals				F	Calculated V <sub>p</sub> (km/s)
									Sp	Cpx	Opx	OI		
Parental melt	44.75	2.55	7.27	12.50	16.77	12.78	1.31	0.19						
Residual melt														
15 Kbar	39.98	4.53	9.56	17.23	13.01	11.10	2.41	0.40	2.5	93.7	2.4	1.5	54.0	7.5–7.8
10 Kbar	41.01	4.86	10.89	16.44	10.59	10.45	2.72	–	2.0	77.3	8.5	12.1	59.0	7.5–7.8
5 Kbar	43.13	4.67	11.58	14.40	9.35	10.92	2.70	0.89	2.5	70.3	–	27.2	56.3	7.6–7.9
3 Kbar	44.05	4.45	11.50	13.49	9.20	11.52	2.56	0.82	2.4	58.6	–	39.0	52.4	7.6–8.0
1 Kbar	44.76	4.22	11.23	12.80	9.30	12.30	2.40	0.36	2.5	53.0	–	44.5	48.2	7.8–8.0

Calculation performed using petrologic code MELTS by Ghiorsio and Sack (1995), with parental magma composition from Xu and Chung (2001)

## References

- Behera L, Sain K, Reddy PR (2004) Evidence of underplating from seismic and gravity studies in the Mahanadi delta of eastern India and its tectonic significance. *J Geophys Res* 109 (B12311)
- Brodie J, White N (1994) Sedimentary basin inversion caused by igneous underplating: Northwest European continental shelf. *Geology (Boulder)* 22(2):147–150
- Brodie J, White N (1995) The link between sedimentary basin inversion and igneous underplating. In: Buchanan JG, Buchanan PG (eds) *Basin inversion*. Geological Society Special Publications, London, pp 21–38
- Campbell IH, Davies GF (2006) Do mantle plumes exist? *Episodes* 29(3)
- Campbell IH, Griffiths RW (1990) Implications of mantle plume structure for the evolution of flood basalts. *Earth Planet Sci Lett* 99:79–93
- Catchings RD, Mooney WD (1988) Crustal structure of the Columbia Plateau: evidence for continental rifting. *J Geophys Res* 93:459–474
- Clift PD (1997) The thermal impact of Paleocene magmatic underplating in the Faeroe-Shetland-Rockall region. In: Fleet AJ, Boldy SAR (eds) *Petroleum geology of Northwest Europe*. Proceedings of the 5th conference, London, UK, pp 585–593
- Clift PD (2005) Sedimentary evidence for moderate mantle temperature anomalies associated with hotspot volcanism. In: Foulger GR, Natland JH, Presnall DC, Anderson DL (eds) *Plates, plumes, and paradigms*. Geological Society of America Special Paper 388, pp 279–287
- Clift PD, Turner J (1998) Paleogene igneous underplating and subsidence anomalies in the Rockall-Faeroe-Shetland area. *Mar Pet Geol* 15(3):223–243
- Fametani CG, Richards MA, Ghiorsio MS (1996) Petrological models of magma evolution and deep crustal structure beneath hotspots and flood basalts. *Earth Planet Sci Lett* 143:81–94
- Furumoto AS, Webb JP, Odegard ME, Husong DM (1976) Seismic studies on the Ontong lava Plateau. *Tectonophysics* 34:71–90
- Ghiorsio MS, Sack RO (1995) Chemical mass transfer in magmatic processes, IV. A revised and internally consistent thermodynamic model for the interpretation and extrapolation of liquid-solid equilibria in magmatic systems at elevated temperatures and pressure. *Contrib Mineral Petrol* 119:197–212
- Ito G, Clift PD (1998) Subsidence and growth of Pacific Cretaceous plateaus. *Earth Planet Sci Lett* 161:85–100
- Jarvis GT, McKenzie DP (1980) The development of basins with finite extension rates. *Earth Planet Sci Lett* 48:42–52
- Kelemen P, Holbrook S (1995) Origin of thick, high-velocity igneous crust along the U. S. East Coast margin. *J Geophys Res* 100:10077–10094
- McKenzie D (1978) Some remarks on the development of sedimentary basins. *Earth Planet Sci Lett* 40:25–32
- Parsons B, Sclater JG (1977) An analysis of the variation of ocean floor bathymetry and heat flow with age. *J Geophys Res* 82:803–827
- Richards MA, Duncan RA, Courtillot VE (1989) Flood basalts and hot-spot tracks: plume heads and tails. *Science* 246:103–107
- Sclater JG, Christie PAF (1980) Continental stretching: an explanation of the post Mid-Cretaceous subsidence of the central North Sea basin. *J Geophys Res* 85:3711–3739
- Steckler MS, Watts AB (1978) Subsidence of the Atlantic-type continental margin off New York. *Earth Planet Sci Lett* 41:1–13
- Stein CA, Stein S (1992) A model for the global variation in oceanic depth and heat flow with lithospheric age. *Nature* 359:123–129
- Thompson RN (1974) Primary basalts and magma genesis, I: Skye, Northwest Scotland. *Contrib Mineral Petrol* 45:317–341

- Trumbull RB, Sobolev SV, Bauer K (2002) Petrophysical modeling of high seismic velocity crust at the Namibian volcanic margin. In: Menzies MA, Klempner SL, Ebinger CJ, Baker J (eds) Volcanic rifted margins. Geological Society of America Special Paper 362, pp 225–234
- Watts AB (2001) Isostasy and flexure of the lithosphere. Cambridge University Press, New York, p 458
- White N, Lovell B (1997) Measuring the pulse of a plume with the sedimentary record. *Nature* 387 (6636):888–891
- Xu Y-G, Chung SL (2001) The Emeishan large igneous province: evidence for mantle plume activity and melting conditions. *Geochimica* 30:1–9
- Xu Y-G, He B (2007) Thick, high-velocity crust in the Emeishan large igneous province, southwestern China: evidence for crustal growth by magmatic underplating or intraplating. In: Foulger GR, Jurdy DM (eds) Plates, plumes and planetary processes. Geological Society of America Special Paper 430, pp 841–858
- Zucca JJ (1984) The crustal structure of the southern Rhinegraben from re-interpretation of seismic refraction data. *J Geophys* 55:13–22

# Chapter 5

## Effects of Plume-Related Thermal Anomaly

### 5.1 Plume Heat Flow

The rise of axisymmetric thermal plumes from the core-mantle boundary (CMB) in a compressible fluid can be modeled using equations for inelastic, compressible fluids with infinite Prandtl number convection (Jarvis and McKenzie 1980). In a simplified case, using boundary layer theory (Yuen and Schubert 1976), heat conduction in vertical direction is negligible when compared to heat advection by the plume, and can be neglected in the energy equations. The heat flux,  $Q$ , and buoyancy flux,  $B$ , of the plume can be defined as (Albers and Christensen 1996):

$$B = \alpha/c_p \cdot Q = 2\pi\rho\alpha \int_0^{r_{max}} r v_z \Delta T_{plume} dr \quad (5.1)$$

where  $\alpha$  is the depth-dependent coefficient of thermal expansion,  $c_p$  is the specific heat capacity (per unit mass) at constant pressure,  $\rho$ ,  $r$  and  $\Delta T$  are the depth-dependent density, radius, and excess temperature of the plume, and  $v_z$  is vertical component of velocity.

The influence of the individual model parameters is different. The plume related thermal anomaly,  $\Delta T$ , at the top is controlled only by the initial temperature anomaly at the CMB, the buoyancy flux,  $B$ , and the dissipation number (defined as  $D = \bar{\alpha}gh/c_p$ , where  $\bar{\alpha}$  is the depth averaged coefficient of thermal expansion,  $g$  is acceleration due to gravity and  $h$  is the height of the plume from the CMB). The excess temperature of the plume decreases with increasing height from its source (CMB), due to adiabatic cooling and heat diffusion. For plumes with high buoyancy flux, the temperature anomaly at the top is very high, which can be about 300 K for a starting anomaly of 500 K at the CMB and Newtonian rheology, while it is low for plumes with lower flux, reaching 100 K. A plot of the thermal anomaly as a function of buoyancy flux (Fig. 5.1) shows that at high flux, the thermal anomaly at the top exceeds half of the initial anomaly, mainly due to loss of heat by slightly

stronger adiabatic gradient in the plume compared to its surroundings, due to high temperature. The loss of heat becomes more important with decreasing buoyancy flux due to increasing heat diffusion. For the flux below  $1000 \text{ kg s}^{-1}$ , the thermal anomaly at the top is small, reaching  $150\text{--}200 \text{ K}$  for  $1000 \text{ kg s}^{-1}$  and less than  $100 \text{ K}$  for  $500 \text{ kg s}^{-1}$ , irrespective of the initial temperature difference. The dissipation number,  $D$ , controls the effects of adiabatic cooling and viscous dissipation. A high value reduces the temperature anomaly because of increasing adiabatic decompression over shear heating inside the plume (Zhao and Yuen 1987).

The heat flux of an upwelling plume can be directly calculated from Eq. 5.1 or its variations, using suitable reference values for the variables (e.g., Yoshida and Ogawa 2005). Indirect estimation of the plume heat flow can be obtained from the plume swell (Davies 1988; Richards et al. 1988; Sleep 1987, 1990), assuming that the excess topographic mass is balanced by the mass deficit of hot upwelling plumes (Yoshida and Ogawa 2005):

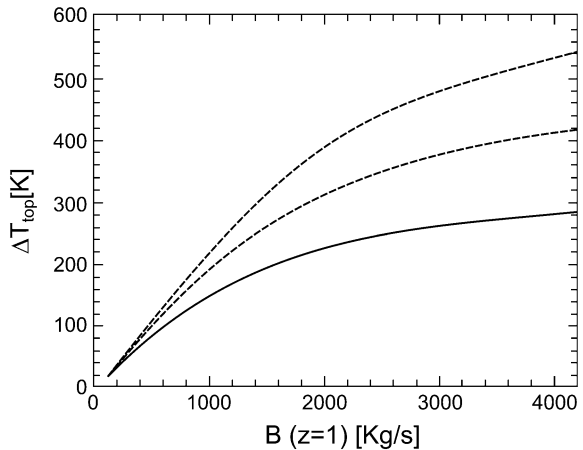
$$\Delta\rho_{\text{top}}v_{\text{plate}}\delta h_{\text{swell}}g = \Delta\rho_{\text{plume}}v_zS_{\text{plume}}g \quad (5.2)$$

where  $\Delta\rho_{\text{top}}$  is the density contrast at the top boundary layer between the mantle and oceanic water,  $v_{\text{plate}}$  is the velocity of the plate overlying the plume,  $\delta h_{\text{swell}}$  is the swell height computed from normal stress at the boundary layer,  $\Delta\rho_{\text{plume}}$  is the density difference between the plume and the surrounding mantle, and  $S_{\text{plume}}$  is the thickness of the plume (Davies 1999; Schubert et al. 2001; Turcotte and Schubert 2002).

For strictly thermal buoyancy,  $\Delta\rho_{\text{plume}}$  equals to  $\rho_m\alpha_0\Delta T_{\text{plume}}$ , where  $\rho_m$  is the density of the mantle and  $\alpha_0$  is the reference coefficient of thermal expansion of the mantle at the starting point, so the plume heat flow estimated from the swell topography,  $Q_s$ , is given as (Yoshida and Ogawa 2005):

$$Q_s = c_p/\alpha \cdot \Delta\rho_{\text{top}}v_{\text{plate}}\delta h_{\text{swell}} \cdot \quad (5.3)$$

**Fig. 5.1** Plot of temperature anomaly beneath the lithosphere ( $\Delta T_{\text{top}}$ ) versus buoyancy flux ( $B$ ) for initial temperature anomalies,  $\Delta T$ , of  $500 \text{ K}$  (solid line),  $750 \text{ K}$  (dot-dashed), and  $1000 \text{ K}$  (dashed line) (modified from Albers and Christensen 1996)



Thus, knowing the plate velocity and the swell height, the plume heat flow can be directly estimated. It should, however, be noted that the heat flow estimated from the swell height,  $Q_s$ , is only a few percent of the basal heat flow, and not more than 10 % of the actual heat flow (Fig. 5.2). This happens as the plume head spreads laterally beneath the moving plate at a velocity, which is a magnitude higher than the plate velocity, and as a result one underestimates the swell amplitude (Yoshida and Ogawa 2005).

Initial thermal anomaly—For plumes starting from the CMB, the initial temperature anomaly is dependent on the temperature difference between the core and the lower mantle. Assuming absence of compositional layering, Stacy and Loper (1983) calculated a temperature difference of about 860 °C across the D'' layer at the CMB. On this basis, the initial plume material would have a thermal anomaly of 700–800 °C, compared to the lower mantle. The anomaly will decrease if the lower part of the D'' layer is stabilized by compositional layering.

Potential temperature anomalies of at least 200 °C are delivered at the base of the crust by modern plumes, which give the lower bound of the temperature anomaly, which can thus be taken as 200–800 °C at the source (Griffiths and Campbell 1990).

Buoyancy and volume flux—Adopting commonly used values for physical properties of the mantle, Davies (1988) and Sleep (1990) had calculated the buoyancy and volume flux for a large number of the currently active hotspots. The buoyancy fluxes range from  $3 \times 10^3 \leq B \leq 8 \times 10^4 \text{ N s}^{-1}$ . The largest flux is that for the Hawaiian plume, which is almost three times larger than the one on the

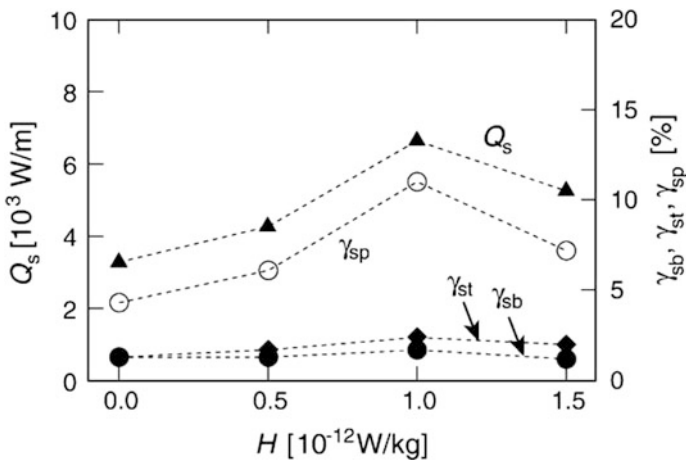


**Fig. 5.2** Plots of plume heat flow estimated from plume-swell for different internal heating rates (Yoshida and Ogawa 2005). The plume heat flow ( $Q_s$ , solid triangles), the ratio of the plume heat flow to the heat flow on the bottom boundary ( $\gamma_{sb}$ , solid circles), the ratio of the plume heat flow to the heat flow on the top boundary ( $\gamma_{st}$ , solid diamonds), and the ratio of the plume heat flow estimated from plume-swell ( $Q_s$ ) to the actual plume heat flow ( $Q_p$ ) ( $\gamma_{sp}$ , open circles) are plotted against internal heating rate  $H$  per unit volume

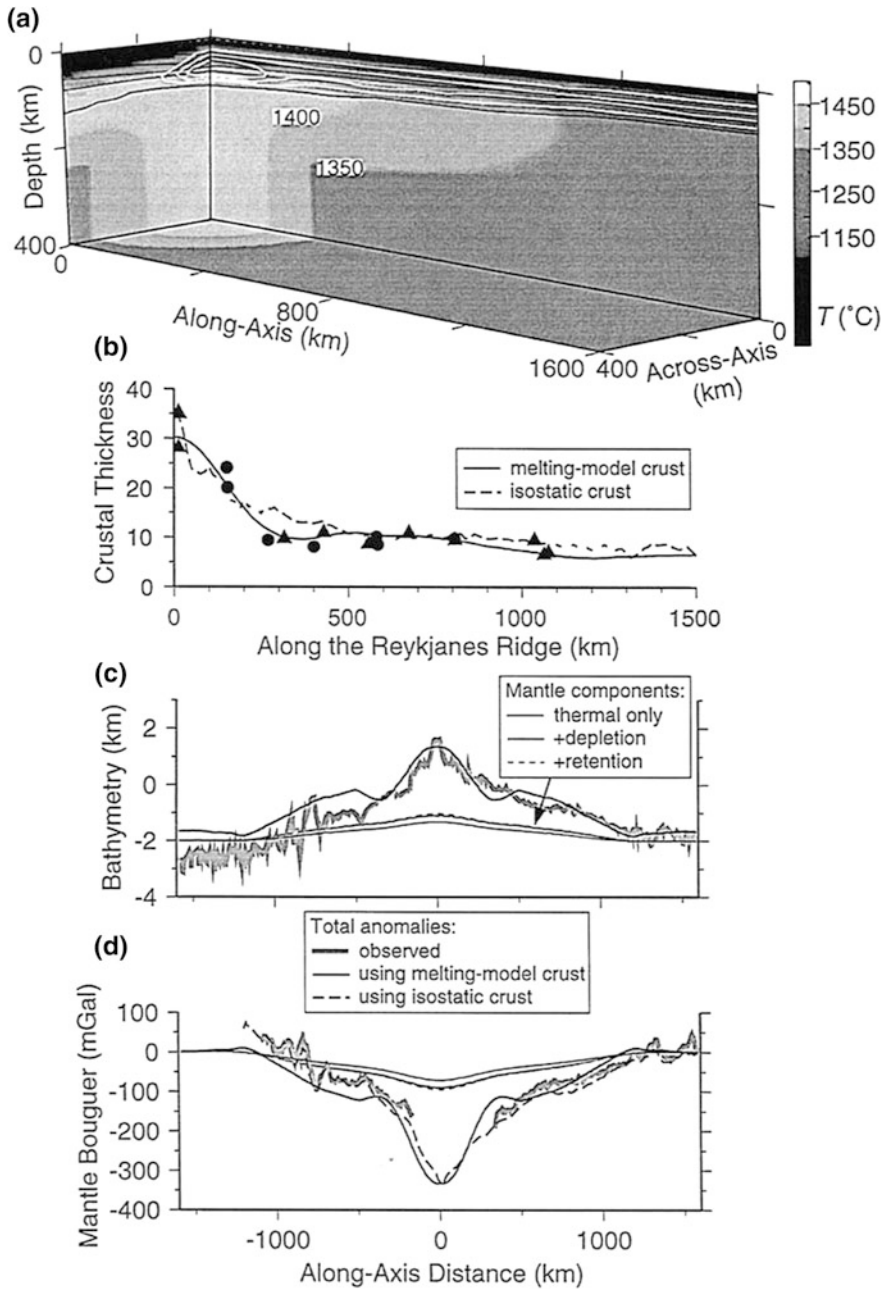


Fig 5.3 (continued)

◀ **Fig. 5.3** **a** Perspective diagram of a broad plume source model shaded according to temperature (Ito et al. 1996). Black contours are depletion and white contours are melting rates of 0.01, 0.03, and 0.05  $\text{my}^{-1}$  (contour interval is 5 %). **b** Comparison between melting-model crust (*solid*) and isostatic crust (*dashed*), and seismic-based crustal thickness measurements along the Reykjanes Ridge (*dots*) and at older seafloor near the continental margins (*triangles*) (Smallwood et al. 1995). **c**, **d** Comparison between the observed bathymetry (*thick gray curve* in **c**) and mantle Bouguer anomaly (*thick gray curve* in **d**) along the Mid Atlantic Ridge and predicted profiles using the melting model crust (*bold curves* in **c** and **d**) and isostatic crust (*thick dashed curved* in **d**). Predicted mantle components due to various mantle density sources are also shown

second place of the list, while the smallest ones are inferred from seafloor swells of only  $\sim 300$  m. The corresponding volume fluxes are  $20 \leq Q \leq 500 \text{ m}^3 \text{ s}^{-1}$  for  $\Delta T_{\text{plume}} = 200 \text{ }^\circ\text{C}$ , or  $5 \leq Q \leq 125 \text{ m}^3 \text{ s}^{-1}$  for  $\Delta T_{\text{plume}} = 800 \text{ }^\circ\text{C}$ .

Plumes having the largest volume flux and initial temperature difference (thermal buoyancy), ascend most rapidly and are least diluted by entrainment in the mantle. Plumes having buoyancy in the order of  $10^5 \text{ N s}^{-1}$  can ascend through the mantle in about 50 my. They are not deflected by flows in the mantle associated with plate motions and remain connected to the source by a stable feeder channel (Whitehead and Luther 1975; Richards and Griffiths 1988; Skilbeck and Whitehead 1978). These are likely to erupt generating flood basalt provinces. Weaker plumes with buoyancy flux less than  $10^4 \text{ N s}^{-1}$  require about 1000 my to reach the surface. They get deflected in the mantle easily, so that the plume head may get disconnected from the source (Whitehead and Luther 1975; Skilbeck and Whitehead 1978), and may break into a number of smaller diapirs rather than a large ascending head. Even smaller plumes are greatly cooled by entrainment in the mantle and never reach the lithosphere. The cut-off for reaching the lithosphere occurs at a buoyancy flux of about  $300 \text{ N s}^{-1}$ , as inferred from observed hotspots (Sleep 1990).

## 5.2 Thermal Uplift

The isostatic uplift of lithosphere due to an ascending mantle plume occurs due to contributions from both the mantle and crust. The mantle contribution gives rise to the dynamic uplift, supported by the flow in the plume head (see Chap. 3), and is ideally calculated from the normal stress at the base of the lithosphere (Ribe et al. 1995). The crustal contribution occurs due to thermal effects of the plume head and adds to the dynamic topography. Extra topography is added by static uplift, which occurs due to excess crustal thickness generated by magmatic underplating (see Chap. 4).

There are four thermal effects of a ponded mantle plume (Ito et al. 1996):

- (1) Thermal buoyancy depending on temperature anomaly and volume flux
- (2) Latent heat loss due to melting in the mantle
- (3) Depletion of Fe/Mg ratio in the residual mantle that reduces its density, and
- (4) Melt retention, reducing bulk density of the mantle

Numerical modeling of the Iceland Ridge done by Ito et al. (1996) shows that a broad plume source, with a radius of 300 km, thermal anomaly of 75 °C and volume flux of  $1.2 \times 10^7 \text{ km}^3 \text{ my}^{-1}$ , can successfully predict the along-axis variations in crustal thickness estimated from seismic (Smallwood et al. 1995) and the topography, while a narrow plume source, with a radius of 60 km, thermal anomaly of 170 °C and volume flux of  $2.1 \times 10^6 \text{ km}^3 \text{ my}^{-1}$ , better explains the total excess crustal production rate along the ridge. The predicted maximum upwelling rate is  $105 \text{ km my}^{-1}$  for the broad source, while it is  $283 \text{ km my}^{-1}$  for the narrow source, approximately 10–30 times faster than normal ridge upwelling rates.

Predicted topography from the broad plume model generates 70 % ( $\sim 2.5 \text{ km}$ ) of the total along-axis topographic anomaly of about 3.5 km by crustal melting and underplating (Fig. 5.3). The remaining 30 % ( $\sim 1 \text{ km}$ ) is caused by dynamic support at the mantle, obtained with a depletion density reduction coefficient of 0.024 (Oxburgh and Parmentier 1977; Sparks et al. 1993). The thermal buoyancy generates about 70 % of the mantle dynamic topography, while depletion and retention buoyancy generate the remaining 22 and 8 % respectively. The predicted total dynamic uplift is consistent with 0.5–1.5 km of Eocene uplift, as obtained from sediment analysis in well cores (Clift et al. 1995).

For the narrow plume source, the mantle contribution to topography becomes much larger than the crustal component of underplating. The mantle uplift is about 51 % (1.8 km), while the crust generates only 49 % of the total observed topographic anomaly (Fig. 5.4). The importance of melt related buoyancy increases significantly with thermal, depletion and retention buoyancy producing 47, 39 and 14 % of the mantle dynamic topography, respectively.

### 5.2.1 *Thermal Rejuvenation Model*

The thermal rejuvenation model was proposed by Detrick and Crough (1978), based on geoid and gravity signatures of the Hawaiian swell. In this model, as the plume gets ponded, the underside of the lithosphere gets heated, and the isotherm defining the lithospheric base is deflected upward. As a result, the lithosphere gets thinned, and lighter asthenospheric material replaces the lithosphere, resulting in isostatic uplift of the ocean floor, forming a broad swell. As the plate moves past the plume, it cools and the swell subsides following oceanic subsidence curves as in a newly-formed lithosphere (Parsons and Sclater 1977; Stein and Stein 1992; Fig. 5.5).

The uplift due to the hot plume can be expressed in terms of an apparent thermal rejuvenated age of the lithosphere, using the depth-age relationship of normal oceanic lithosphere (Sleep 1992):

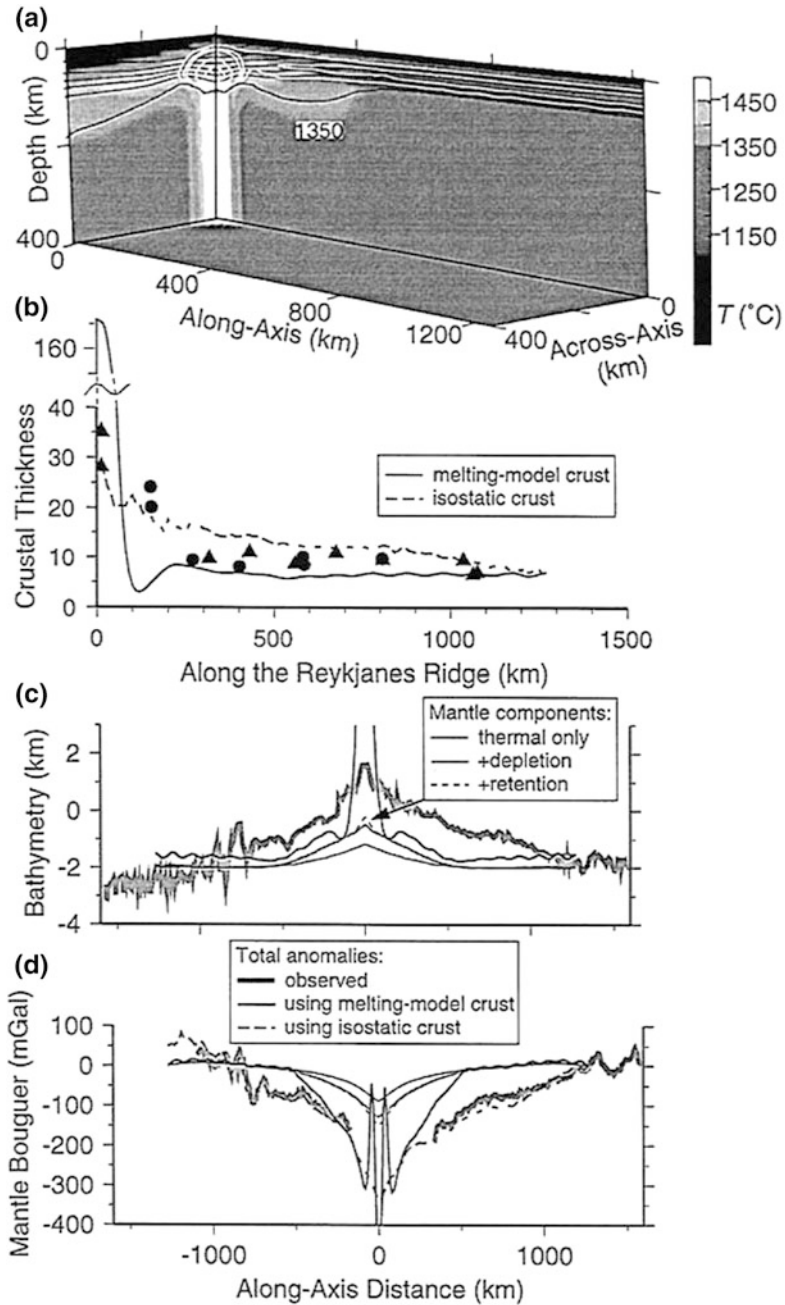


**Fig. 5.4** The same diagram as in Fig. 5.3, but done for narrow plume source model (Ito et al. 1996). Symbols as in Fig. 5.3 except melting rate contours in (a), which are 0.01, 0.03, 0.05, 0.2 and 0.4  $\text{my}^{-1}$

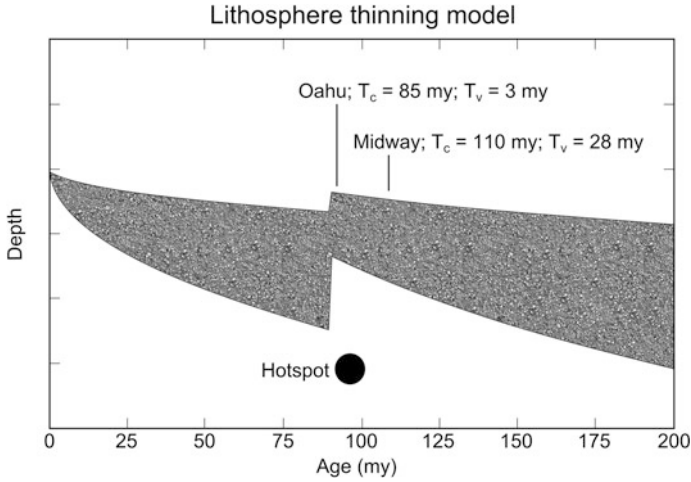


**Fig. 5.5** Schematic diagram of lithospheric thinning by thermal rejuvenation model for the formation of mid-plate hotspot swells (modified from Woods and Okal 1996). The ages of oceanic crust ( $T_c$ ) and volcanic edifices ( $T_v$ ) are shown for Oahu and Midway

$$D = D_0 + 350\sqrt{(\text{age}_c)} \quad (5.4)$$

where  $D$  and  $D_0$  are the depths of the normal oceanic lithosphere and that at the ridge in meters, respectively, and  $\text{age}_c$  is the age of the oceanic lithosphere in my. The rejuvenated depth of the swell,  $D_r$  is given as

$$D_r \equiv D_0 + 350\sqrt{(\text{age}_r)} \quad (5.5)$$

where  $\text{age}_r$  is the rejuvenation age in my, and the swell uplift is  $D - D_r$ .

In the case of the Hawaiian swell, a number of geophysical observations seem to match with the uplift predicted by the thermal rejuvenation model. Thus, its gravity and geoid signature (Crough 1978, 1983; Sandwell and Poehls 1980; Sandwell and Renkin 1988), shape and subsidence rate (Detrick and Crough 1978; Menard and McNutt 1982; Epp 1984) and its heat flow (Detrick et al. 1981; Von Herzen et al. 1982) has been used to support the model. The heat flow values are normal for the oceanic crustal age at Hawaii, but increases slightly towards Midway rather than decreasing, as the crust becomes older (Detrick et al. 1981) (Fig. 5.6). This observation supports the thermal rejuvenation model, as no other model of swell formation (see Crough 1983) can explain this inconsistency. Based on thinning estimates, the lithospheric thickness is predicted to be only about 40–50 km at the hotspot. However, the shear-velocity models suggest that the lithosphere is about 100 km thick, which is difficult to reconcile with the lower values predicted by the model (Woods and Okal 1996).

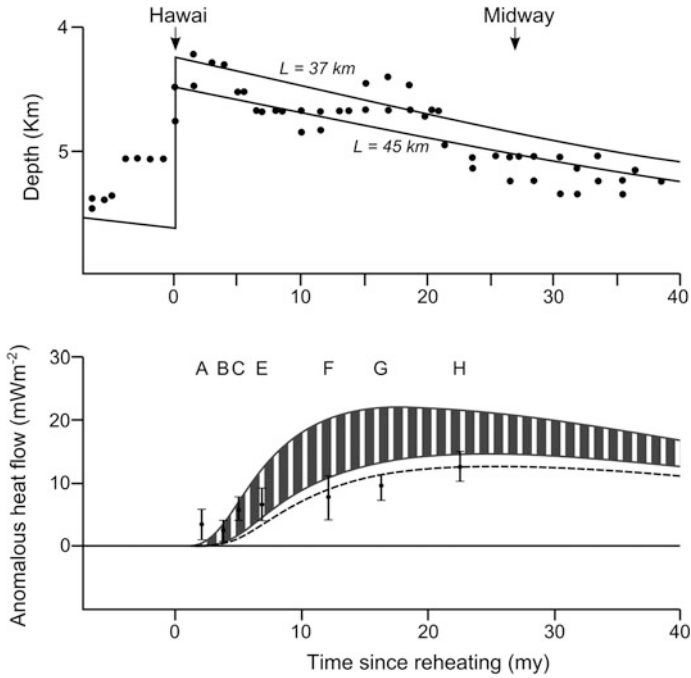


**Fig. 5.6** Minimum depth,  $1^\circ \times 1^\circ$  averages, and anomalous surface heat flow along the Hawaiian Swell in direction from the southeast of Hawaii towards northwest, to the Hawaiian-Emperor bend (modified from Detrick et al. 1981). Ages since lithospheric rejuvenation by the hotspot are given in my. *Solid lines* are the predictions for instantaneous reheating of the lower part of 90 my old lithosphere at Hawaii, followed by standard cooling. The *upper curve* in both plots is for a new lithospheric thickness ( $L$ ) of 37 km after reheating. The lower one is for 45 km. The *lower curve* is a better fit to both data sets (Crough 1983). The *dashed curve* considers the possible effect of an age offset across the Molokai fracture zone near Hawaii and is made for reheated 80 my-old lithosphere

### 5.3 Thermal Subsidence

The topographic swell due to thermal uplift depends on the balance between magma flux and thermal cooling. A typical thermal anomaly in the order of 100–350 °C produces an initial high as the plume approaches the lithosphere. Thermal cooling then begins as soon as the plume head begin spreading under the lithosphere, which tends to lower the topography created earlier. The maximum subsidence is expected at the centre of the uplift; however, the upwelling magma flux maintains the high at the centre, and the surrounding areas tend to subside faster due to removal of the dynamic support from below (Mège and Ernst 2001). Numerical models made by Olson (1994) suggest that the elevation of the area surrounding the plume conduit may increase for some 15 my after plume initiation and then decrease until the plume activity ceases. After 15 my, the subsidence continues in the plume centre,

while minor uplift occurs further outward. The subsidence propagates laterally outwards and most of the uplift has waned after a few tens of millions years.

## 5.4 Plume-Ridge Interactions

A large number of present day mantle plumes lies near divergent plate boundaries (mid-oceanic ridges), and quite a few coincide (or nearly coincide) with the ridge axes. Examples include Iceland, Azores, Afar, Jan Mayen, and Galapagos. The interaction between these plumes and the plate movement is a three-dimensional problem of fluid mechanics, the modelling of which requires an analysis of fluid flow in thin layers using lubrication theory, a 3D numerical convection model using temperature and pressure dependent rheology, or elaborate experimental apparatus.

### 5.4.1 Ridge-Centred Plumes

Ridge-centred plumes (plumes rising directly beneath a ridge) were first studied in laboratory experiments by Feignner and Richards (1995), and further developed by numerical analysis (Feighner et al. 1995; Ribe et al. 1995; Ito et al. 1996). Modelling studies have identified the dynamic interaction between mantle plumes and mid-oceanic ridges in terms of scaling laws for plume head waist-width,  $W$  (defined as the *length of along-axis spreading of the plume material, before being swept away from the ridge by diverging plate motion*), plume volume flux,  $Q$  and ridge half-spreading rate,  $U$ . For spreading of buoyant plume material from a *point source* below the lithosphere, the plume head thickness,  $S$ , is given by (Ribe et al. 1995):

$$S \sim (Q/\sigma)^{1/4} \equiv S_0 \quad (5.6)$$

and the plume head width normal to the spreading direction,  $L$ , as (Ribe et al. 1995):

$$L \sim Q^{3/4} U^{-1} d^{1/2} \sigma^{1/4} \equiv L_0 \quad (5.7)$$

where  $\sigma = g\Delta\rho/48\eta$  ( $\eta$  is the viscosity and  $\Delta\rho$  is the density anomaly of the plume).  $\sigma$  measures the relative strength of gravitational versus plate-driven spreading of the plume material,  $d$  is the ridge width, and  $L_0$  and  $S_0$  are the width and thickness of the plume material away from the ridge, respectively. At the ridge, however, the plume head width is given by scaling law for the waist width,  $W$ , as (Ribe et al. 1995):

$$W \sim (Q/U)^{1/2} \equiv L_s \quad (5.8)$$

for narrow gap case,  $S_0/d \gg 1$  ( $L_s$  in Eq. 5.8 and  $L_w$ , in Eq. 5.9 are special notations of  $L$  for ridge-centred plumes). For a wide gap case with  $S_0/d \ll 1$ , the waist width is given as:

$$W \sim Q^{3/8} U^{-1/2} d^{1/2} \sigma^{1/8} \equiv L_w. \quad (5.9)$$

For a more realistic situation, where the source has a *finite radius*, ‘narrow gap’, and waist width is calculated at a distance where the plume thickness is  $0.1 S_0$ ,  $W$  is given by (Ribe et al. 1995, but also see Ribe 1996, pp. 16, 198, Eq. 11):

$$W = 1.65(Q/U)^{1/2} \Pi_b^{0.053} \quad (5.10)$$

where  $\Pi_b$ , known as the buoyancy number, is given by  $\Pi_b = Q\sigma/U^2 \equiv (L_0/S_0)^2$ . The equation can be generalized to include a viscosity contrast between the plume and the surrounding mantle (for details see Ribe et al. 1995, p. 157). 3D numerical convection modelling gives a similar scaling law for the waist width as (Ribe et al. 1995):

$$W = 2.07(Q/U)^{1/2} \Pi_b^{0.052}. \quad (5.11)$$

Modelling results from both lubrication theory model and 3D convection models agree closely, pointing out that the essential dynamics of plume-ridge interactions are independent of whether the buoyancy of the plume is thermal or chemical. However, the dependency of the waist width on mantle-plume viscosity contrast remains unresolved, and is incorporated in an approximate way. Also, the models do not show any evidence of the waist width being affected by upslope movement of plume material towards the ridge along the base of the lithosphere.

### 5.4.2 Off-Ridge Plumes

Various observations suggest that plumes interact with ridges even if they are located as far as 1400 km away (Ribe 1996). The evidences include presence of aligned patterns of constructional volcanism near hotspots (e.g., Galapagos and Reunion, Morgan 1978), and systematic variation in bathymetry and basalt geochemistry along ridge segments near hotspots (Talwani et al. 1971; Schilling 1973, 1985). Off-ridge plume dynamics were studied in the laboratory by Kinkad et al. (1995a) and by 2D numerical modelling by Kinkad et al. (1995b) and Ribe (1996). For a source with a *finite radius* and waist width calculated at a distance where the plume thickness is  $0.1 S_0$ , the functional generalized scaling law is given by Ribe (1996) as:

$$W = W_0 F_1(\Pi_b) (1 + 1.77 \Pi_u \Pi_b^{-0.33}) \cdot F_3[x_p/W_0 F_2(\Pi_b) (1 - 0.34 \Pi_b^{0.30})] \quad (5.12)$$

where  $\Pi_u$  is the upslope number, defined as  $\Pi_u = Q^{1/8}U^{-1}\sigma^{3/8}\kappa^{1/2}$ ,  $\kappa$  is thermal diffusivity,  $x_p$  is the plume-ridge distance,  $W_0$  is the waist width at the ridge, and the functions F1-F3 are defined by the equations (Ribe 1996, also see Ito et al. 1997):

$$\log_{10}F_1 = 0.217 + 0.0569p + 0.0176p^2 + 0.00275p^3 \quad (5.13)$$

$$\log_{10}F_2 = 0.043p + 0.060p^2 - 0.0062p^2 \quad (5.14)$$

$$F_3(s) = (1 - 1.25s^2)^{1/2} \quad (5.15)$$

where  $p = \log_{10}\Pi_b$  and  $s$  is the functional argument.

The maximum plume-ridge interaction distance,  $x_{\max}$  is given as (Ribe 1996):

$$x_{\max} = 0.89W_0F_2(\Pi_b)(1 - 0.34\Pi_b^{0.30}). \quad (5.16)$$

Different mechanisms controlling the plume material distribution below the ridge are gravitational spreading, advection by corner flow, upslope flow towards the ridge along the sloping base of the lithosphere, incorporation into the lithosphere by freezing and plume-induced lithospheric thinning. Numerical modelling suggests that gravitational spreading and advection are dominant mechanisms, while the three others have minor effects. Because these three mechanisms require a lithosphere of finite thickness, while the dominant mechanism do not, it appears that models of plume-ridge interaction in an infinitely thin lithosphere (Feignner and Richards 1995; Ribe et al. 1995) are valid to first order.

### 5.4.3 Migrating Ridges

The case of ridges migrating away from the plume has been numerically modelled by Ito et al. (1997) and Ribe and Delattre (1998). For a thin lithosphere of uniform thickness ( $\Pi_u = 0$ ), the functional form of the complete scaling law giving the waist width,  $W$ , is (Ribe and Delattre (1998):

$$W = W_0AF_1(\Pi_b)F_3\left[\left\{\left(x'_p + B\right)/C\right\}/\left\{F_2(\Pi_b)\right\}\right] \quad (5.17)$$

where  $x'_p \equiv x_p/W_0$ , and  $A$ ,  $B$  and  $C$  are the scaling factors for the height, lateral shift and width, respectively, of a given waist width curve to fit it to that of a stationary ridge, defined as:

$$A = F_4(\Pi_m/F_5(\Pi_b))[1 + \Pi_mF_{11}(\Pi_b)F_{12}(\theta)] \quad (5.18)$$

$$B = F_6(\Pi_b)F_7(\Pi_m)[1 + F_{13}(\theta)] \quad (5.19)$$

$$C = [1 + F_8(\Pi_b)F_9(\Pi_m/F_{10}(\Pi_b))][1 + \Pi_m F_{14}(\Pi_b) F_{15}(\theta)] \quad (5.20)$$

where,  $\Pi_m (=U_m/U)$  is known as the migration number,  $U_m$  is the ridge migration speed,  $\theta$  is the azimuth of the migration velocity relative to the plate-spreading direction in radians, and  $F_4$ - $F_{15}$  are empirical functions (for function definitions see Ribe and Delattre 1998, p. 518).

Ridge migration increases the distance over which a plume interacts with the ridge. The single  $x_{\max}$  value for a stationary ridge bifurcates into a smaller  $x^-$  and a larger  $x^+$  value, which is applied depending on whether the ridge approaches the plume, or recedes away from it, respectively. This explains the observation that most plume-ridge interactions occur when the ridge migrates away from the plume (Schilling 1991).

The plume-ridge interaction exhibits three distinct stages (Fig. 5.7). In the first, pre-interaction stage, the ridge moves towards the plume, but no interaction has yet taken place, so  $W = 0$ . When the ridge reaches a critical distance  $|x_p| = x^-$  from the plume, the interaction begins, and  $W$  becomes non-zero. Finally, after the ridge has moved beyond the plume to a critical distance  $|x_p| = x^+$  from the ridge,  $W$  again becomes zero, and the ridge has effectively separated the plume head into two parts.

The numerical experiments also evaluate the role of lithospheric thickness variation in plume-ridge interactions. Ridge-ward flow of buoyant plume material along the slope of the oceanic lithosphere has been proposed by Kinkaid et al. (1995a, b), while Morgan (1978) and Schilling (1991) have suggested that the transport of the plume material towards the ridge is enhanced if the plume carves a channel at the base of the lithosphere. The effectiveness of these processes were found to be small, amounting of 20 % variation in the plume flux,  $Q$ , required to generate a given waist width (Ito et al. 1997; Ribe and Delattre 1998).

#### 5.4.4 Ridge Jump

Many places along the mid-oceanic ridge system show evidences of ridge jump towards the associated hotspot; examples include localities near Ascension, Conrad Rise, Discovery, Galapagos, Iceland, Ninety-East Ridge, Loiusville, Shatsky Rise, Shona and Tristan de Cunha (Hey 1977; Mammerickx and Sandwell 1986; Brozena and White 1990; Muller et al. 1993; Krishna et al. 1995; Small 1995; Hardarson et al. 1997; Nakanishi et al. 1999; Krishna and Rao 2000; Briais and Rabinowicz 2002). There are several mechanism promoting such jumps, including lithospheric tension induced by buoyant, convecting asthenosphere (Mittelstaedt and Ito 2005), thermo-mechanical thinning of the lithosphere by the ascending plume (Jurine et al. 2005) and reheating of the lithosphere due to magmatic penetration through the plate (Kendall et al. 2005). Numerical modelling of lithospheric reheating by Mittlestaedt et al. (2008) indicates that hotspot magmatic heating rate required to initiate a ridge jump increases non-linearly with increasing spreading rate and

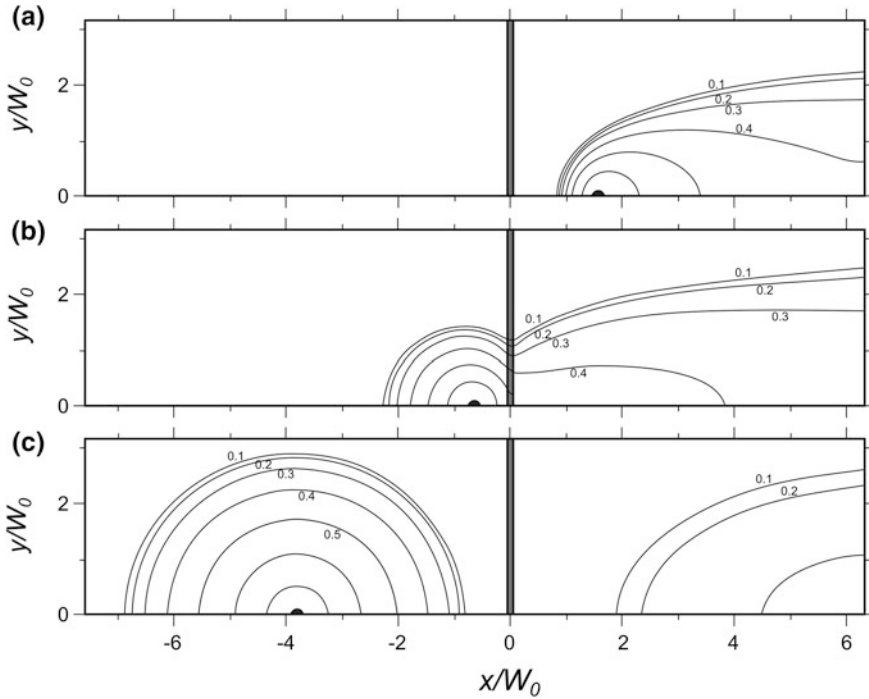


**Fig. 5.7** Thickness  $S(x, y)/S_0$  of a plume head interacting with a migrating ridge, at three different times (modified from Ribe and Delattre 1998). Diagram is in the frame of the ridge (*double vertical line*), with the plume stem (*solid semi-circle*) moving to the left at speed  $U_m = U$  ( $\Pi_m = 1$ ). The buoyancy number  $\Pi_b$  is 100, and  $\Pi_u = 0$  (uniform lithosphere.) **a** Pre-interaction stage, **b** interaction stage, and **c** post-interaction stage

sea-floor age. For a slow spreading ridge, and young oceanic lithosphere, such as that in Iceland, the magmatic heating is sufficient to initiate a ridge jump by itself, while at intermediate spreading centres, such as those in the Galapagos, the magmatic heating alone is insufficient to initiate ridge jump, in spite of the higher magma flux; the time required to initiate a ridge jump is of the order of 0.1–1 my (Mittlestaedt et al. 2008). Similar observations were also recorded by Brozena and White (1990) for the slow spreading Mid-Atlantic Ridge and the Ascension hotspot.

Examples of ridge jump from Iceland (Smallwood and White 2002) and Ascension hotspots (Brozena and White 1990) indicate repeated jumps towards the plume (eastward in both cases), so as to keep the ridge axis centred approximately above the plume head. Described ridge-jumps do not occur as instantaneous transfer of spreading from the old to the new centre, but cover a span of a few million years (4 my for the most recent ridge jump in Iceland) during which spreading remains distributed across both the old and new ridge (Smallwood and White 2002; Mittlestaedt et al. 2008) (Fig. 5.8). The propagating rifts move away from the hotspot, as reported from other areas as well. The cause for these

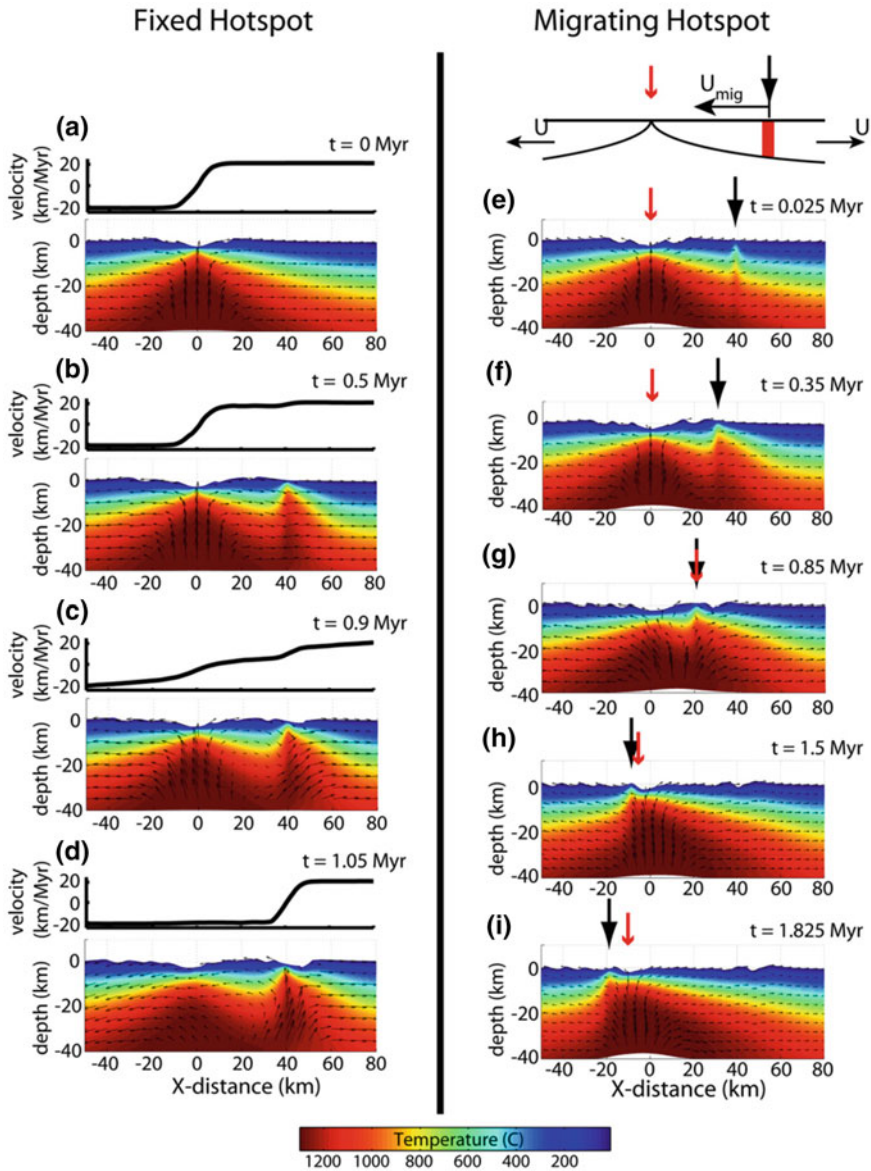


**Fig. 5.8** Thermal evolution of ridge jump for a hotspot that remains fixed with respect to the ridge and a hotspot migrating relative to the ridge at a rate of  $U_{mig} = 30$  km/my. The half spreading rate is  $U = 20$  km/my for both cases. Colors panels show cross-sections of temperature and mantle flow by arrows; profiles above show depth-averaged velocities within the upper 20 km of the model (Mittlestaedt et al. 2008). In the evolution of the migrating hot spot, migration of the hotspot (*large black arrow*) relative to the ridge is shown by large, *black arrow*, while the small, *red arrow* point the location of the spreading center

ridge-jumps on a slow-spreading ridge seems because of the disruption in the symmetric mantle flow below the ridge-axis due to an off-axis plume. The disruption in the melt focussing mechanism below the ridge, together with enhanced melt availability and thinner and weaker lithosphere near the plume causes a ridge jump towards the hotspot (Brozena and White 1990).

## References

- Albers M, Christensen UR (1996) The excess temperature of plumes rising from the core-mantle boundary. *Geophys Res Lett* 23(24):3567–3570
- Briais A, Rabinowicz M (2002) Temporal variations of the segmentation of slow to intermediate spreading mid-ocean ridges 1. synoptic observations based on satellite altimetry data. *J Geophys Res* 107(B5)
- Brozena JM, White RS (1990) Ridge jumps and propagations in the South Atlantic Ocean. *Nature* 348:149–152
- Clift PD, Turner J, ODP Leg 152 Scientific Party (1995) Dynamic support by the Iceland plume and its effect on the subsidence of the Northern Atlantic Margins. *J Geol Soc London* 152: 935–942
- Crough ST (1978) Thermal origin of mid-plate hot-spot swells. *Geophys J R Astr Soc* 55:451–469
- Crough ST (1983) Hotspot swells. *Ann Rev Earth Planet Sci* 11:165–193
- Davies GF (1988) Ocean bathymetry and mantle convection: 1. large-scale flow and hotspots. *J Geophys Res* 93:10467–10480
- Davies GF (1999) *Dynamic earth: plates, plumes and mantle convection*. Cambridge University Press, Cambridge, p 458
- Detrick RS, Crough ST (1978) Island subsidence, hot spots, and lithospheric thinning. *J Geophys Res* 83:1236–1244
- Detrick RS, von Herzen RP, Crough ST, Epp D, Fehn U (1981) Heat flow on the Hawaiian swell: a test of the lithospheric reheating model. *Nature* 292:142–143
- Epp D (1984) Implications of volcano and swell heights for thinning of the lithosphere by hotspots. *J Geophys Res* 89:9991–9996
- Feighner MA, Richards MA (1995) The fluid dynamics of plume-ridge and plume-plate interactions: an experimental investigation. *Earth Planet Sci Lett* 129:171–182
- Feighner MA, Kellogg LH, Travis BJ (1995) Numerical modeling of chemically buoyant mantle plumes at spreading ridges. *Geophys Res Lett* 22:715–718
- Griffiths RW, Campbell IH (1990) Stirring and structure in mantle starting plumes. *Earth Planet Sci Lett* 99:66–78
- Hardarson BS, Fitton JG, Ellam RM, Pringle MS (1997) Rift relocation—a geochemical and geochronological investigation of a paleo-rift in northwest Iceland. *Earth Planet Sci Lett* 153:181–196
- Hey RN (1977) Tectonic evolution of the Coco-Nazca spreading center. *Geol Soc Amer Bull* 88:1404–1420
- Ito G, Lin J, Gable C (1996) Dynamics of mantle flow and melting at a ridge-centered hotspot: Iceland and the Mid-Atlantic Ridge. *Earth Planet Sci Lett* 144:53–74
- Ito G, Lin J, Gable C (1997) Interaction of mantle plumes and migrating midocean ridge systems: implications for the Galapagos plume-ridge system. *J Geophys Res* 102:15403–15417
- Jarvis GT, McKenzie DP (1980) Convection in a compressible fluid with infinite Prandtl number. *J Fluid Mech* 96:515–583
- Jurine D, Jaupart C, Brandeis G, Tackley PJ (2005) Penetration of mantle plumes through depleted lithosphere. *J Geophys Res* 110(B10104)

- Kendall JM, Stuart GW, Ebinger CJ, Bastow ID, Keir D (2005) Magma-assisted rifting in Ethiopia. *Nature* 433:146–148
- Kincaid C, Ito G, Gable C (1995a) Laboratory investigation of the interaction of off-axis mantle plumes and spreading centres. *Nature* 376:758–761
- Kincaid C, Schilling J-G, Gable C (1995b) The dynamics of off-axis plume-ridge interaction in the uppermost mantle. *Earth Planet Sci Lett* 137:29–43
- Krishna KS, Rao DG (2000) Abandoned Paleocene spreading center in the northeastern Indian Ocean: evidence from magnetic and seismic reflection data. *Mar Geol* 162:215–224
- Krishna KS, Rao DG, Ramana MV, Subrahmanyam V, Sarma KVLNS, Pilipenko AI, Shcherbakov VS, Radhakrishna Murthy IV (1995) Tectonic model for the evolution of oceanic crust in the northeastern Indian Ocean from the Late Cretaceous to the early Tertiary. *J Geophys Res* 100(B10):20011–20024
- Mammerickx J, Sandwell DT (1986) Rifting of old oceanic lithosphere. *J Geophys Res* 91:1975–1988
- Mège D, Ernst RE (2001) Contractional effects of mantle plumes on Earth, Mars, and Venus. In: Ernst RE, Buchan KL (eds) *Mantle plumes: their identification through time*. Boulder, Colorado, Geological Society of America Special Paper 352, pp 103–140
- Menard HW, McNutt M (1982) Evidence for and consequences of thermal rejuvenation. *J Geophys Res* 87:8570–8580
- Mittelstaedt E, Ito G (2005) Plume–ridge interaction, lithospheric stresses, and the origin of near-ridge volcanic lineaments. *Geochem Geophys Geosys* 6(6)
- Mittelstaedt E, Ito G, Behn MD (2008) Mid-ocean ridge jumps associated with hotspot magmatism. *Earth Planet Sci Lett* 266:256–270
- Morgan WJ (1978) Rodriguez, Darwin, Amsterdam, ..., a second type of hotspot island. *J Geophys Res* 83:5355–5360
- Muller RD, Royer J, Lawver LA (1993) Revised plate motions relative to the hotspots from combined Atlantic and Indian Ocean hotspot tracks. *Geology* 21:275–278
- Nakanishi M, Sager WW, Klaus A (1999) Magnetic lineations within Shatsky Rise, northwest Pacific Ocean: implications for hotspot-triple junction interaction and oceanic plateau formation. *J Geophys Res* 104(B4):7539–7556
- Olson P (1994) Mechanics of flood basalt magmatism. In: Ryan MP (ed) *Magmatic systems*. Academic Press, San Diego, pp 1–18
- Oxburgh ER, Parmentier EM (1977) Compositional and density stratification in oceanic lithosphere-causes and consequences. *J Geol Soc London* 133:343–355
- Parsons B, Sclater JG (1977) An analysis of the variation of ocean floor bathymetry and heat flow with age. *J Geophys Res* 82:803–827
- Ribe NM (1996) The dynamics of plume-ridge interaction, 2. off-ridge plume. *J Geophys Res* 101:16195–16204
- Ribe NM, Delattre WL (1998) The dynamics of plume-ridge interaction, III: the effects of ridge migration. *Geophys J Int* 133:511–518
- Ribe NM, Christensen UR, Theissing J (1995) The dynamics of plume-ridge interaction, 1: ridge-centered plumes. *Earth Planet Sci Lett* 134:155–168
- Richards MA, Griffiths RW (1988) Deflection of plumes by mantle shear flow: experimental results and a simple theory. *Geophys J* 94:367–376
- Richards MA, Hager BH, Sleep NH (1988) Dynamically supported geoid highs over hotspots: observations and theory. *J Geophys Res* 93:7690–7708
- Sandwell DT, Poehls KA (1980) A compensation mechanism for the central Pacific. *J Geophys Res* 85:3751–3758
- Sandwell DT, Renkin ML (1988) Compensation of swells and plateaus in the north Pacific: no direct evidence for mantle convection. *J Geophys Res* 93:2775–2783
- Schilling J-G (1973) Iceland mantle plume: geochemical evidence of Reykjanes Ridge. *Nature* 242:565–571
- Schilling J-G (1985) Upper mantle heterogeneities and dynamics. *Nature* 314:62–67

- Schilling J-G (1991) Fluxes and excess temperatures of mantle plumes inferred from their interaction with migrating mid-ocean ridges. *Nature* 352:397–403
- Schubert G, Turcotte DL, Olson P (2001) *Mantle convection in the earth and planets*. Cambridge University Press, Cambridge, p 940
- Skilbeck JN, Whitehead JA (1978) Formation of discrete islands in linear chains. *Nature* 272:499–501
- Sleep NH (1987) Lithospheric heating by mantle plumes. *Geophys J Royal Astron Soc* 91:1–12
- Sleep NH (1990) Hotspots and mantle plumes: some phenomenology. *J Geophys Res* 95:6715–6736
- Sleep NH (1992) Hotspot volcanism and mantle plumes. *Ann Rev Earth Planet Sci* 20:19–43
- Small C (1995) Observations of ridge–hotspot interactions in the Southern Ocean. *J Geophys Res* 100:17931–17946
- Smallwood JR, White RS (2002) Ridge-plume interaction in the North Atlantic and its influence on continental breakup and seafloor spreading. In: Jolley DW, Bell BR (eds) *The North Atlantic igneous province; stratigraphy, tectonic, volcanic and magmatic processes*. Geological Society, London, Special Publications 197:15–37
- Smallwood JR, White RS, Minshull TA (1995) Seafloor spreading in the presence of the Iceland plume: the structure of the Reykjanes Ridge at 61°40'N. *J Geol Soc London* 152:1023–1029
- Sparks DW, Parmentier EM, Phipps Morgan J (1993) Three-dimensional mantle convection beneath a segmented spreading center: implications for along-axis variations in crustal thickness and gravity. *J Geophys Res* 98:21977–21995
- Stacey FD, Loper DE (1983) The thermal boundary-layer interpretation of D'' and its role as a plume source. *Phys Earth Planet Inter* 33:45–55
- Stein CA, Stein S (1992) A model for the global variation in oceanic depth and heat flow with lithospheric age. *Nature* 359:123–129
- Talwani M, Windisch CC, Langseth MG Jr (1971) Reykjanes ridge crest: a detailed geophysical study. *J Geophys Res* 76:473–517
- Turcotte DL, Schubert G (2002) *Geodynamics*, 2nd edn. Cambridge University Press, Cambridge, p 456
- von Herzen RP, Detrick RS, Crough ST, Epp D, Fehn U (1982) Thermal origin of the Hawaiian swell: heat flow evidence and thermal models. *J Geophys Res* 87:6711–6723
- Whitehead JA, Luther DS (1975) Dynamics of laboratory diapir and plume models. *J Geophys Res* 80:705–717
- Woods MT, Okal EA (1996) Rayleigh-wave dispersion along the Hawaiian swell: a test of lithospheric thinning by thermal rejuvenation at a hotspot. *Geophys J Int* 125:325–339
- Yoshida M, Ogawa M (2005) Plume heat flow in a numerical model of mantle convection with moving plates. *Earth Planet Sci Lett* 239:276–285
- Yuen DA, Schubert G (1976) Mantle plumes: a boundary layer approach for Newtonian and non-Newtonian temperature-dependant rheologies. *J Geophys Res* 81:2499–2510
- Zhao W, Yuen DA (1987) The effects of adiabatic and viscous heatings on plumes. *Geophys Res Lett* 14:1223–1226

# Chapter 6

## Morphology of Hotspots

### 6.1 Growth of Submarine Volcanoes

Oceanic volcanoes are composed of basaltic lava flows from shallow magma chambers. The process of volcano build-up is poorly understood. In general, smooth rounded shapes are produced by summit eruptions, while complex ridges are produced by flank eruptions. The time taken for a seamount to grow is relatively short. An example from Hawaii documents an eruption rate of  $0.05 \text{ km}^3 \text{ yr}^{-1}$ , indicating a time of  $\sim 2.3 \text{ my}$  to form the island (total volume above and below sea level is  $1.13 \times 10^5 \text{ km}^3$ ) (Watts 2001). The basalts building up the volcanic edifice represent a load on the oceanic crust, which subsides under its weight. As the subsided region gets infilled, the volume of volcanic material required to build up the edifice is larger than the volume that stands above the surrounding ocean floor. Menard (1986) estimated that a seamount standing 3 km above the surrounding seafloor would have to grow about 9 km in height, as almost 6 km of its base gets subsided.

A model-based growth of a sea mount is shown in Fig. 6.1, assuming a visco-elastic plate model, 5 km of water depth, summit eruption building up the volcano, and 1 my time for the volcano to reach the sea level (Watts 2001). Initially the plate remains rigid, and the volcano builds up rapidly, reaching 50 % of its final height above the sea floor by 130 ky. As the load widens, the visco-elastic plate weakens, subsidence increases, and a further 870 ky for required by the seamount to reach the final height (see Chap. 1 on Elastic properties of the lithosphere, for the governing equations).

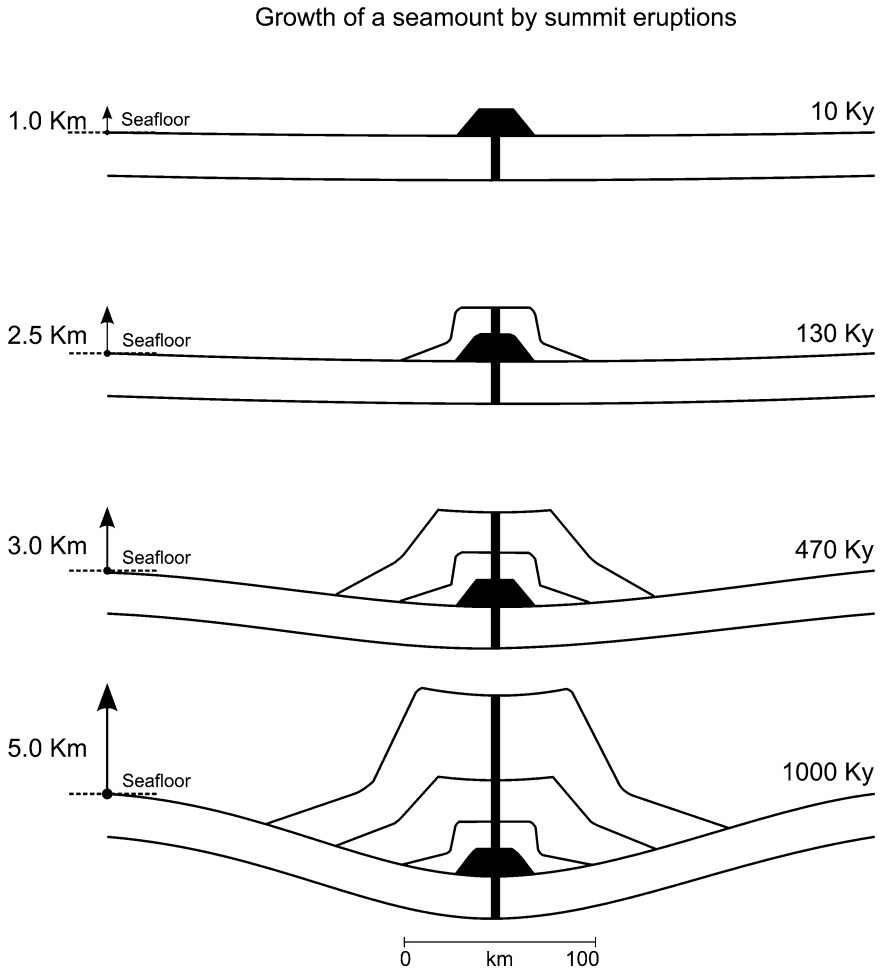


**Fig. 6.1** Simplistic model for the growth of a seamount on the seafloor by summit eruption (modified from Watts 2001). Ages are based on eruption rates and time scale of stress relaxation in the oceanic plate

## 6.2 Morphogenesis of Eruption Centers

Mid-oceanic ridge volcanoes show a variety of forms, ranging from small, round, truncated cones with a central crater or caldera (Hollister et al. 1978; Fig. 6.2), to large complex patterns. Larger seamounts, guyots and ocean islands generally show multiple volcanic centers with radiating ridges (volcanic rift zones) and embayments associated with debris avalanche lobes in the volcanic flanks (Vogt and Smoot 1984; Fig. 6.3). There is a general progression towards complex shapes (Fig. 6.4) during the evolutionary phase of a seamount, as observed in Geisha

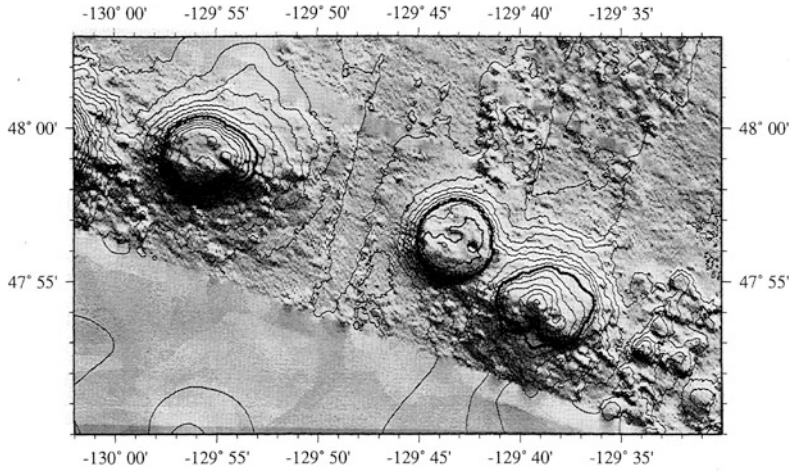


**Fig. 6.2** A small chain of mid-ocean ridge volcanoes (Mitchell 2001). Contours are at every 100 m

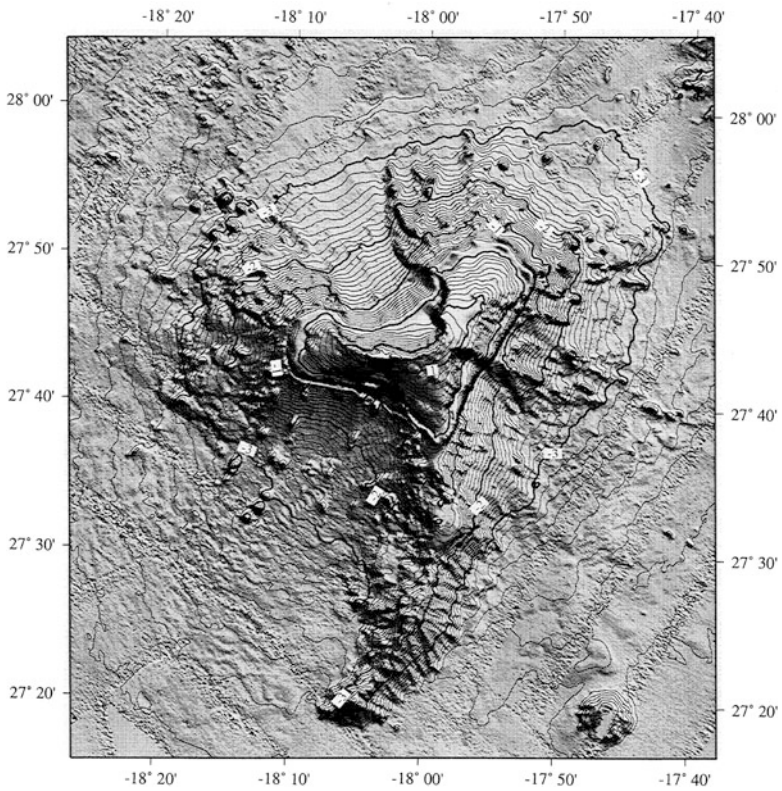


**Fig. 6.3** Multibeam bathymetry map of El Hierro island of the Canaries showing embayments due to landslides and radiating volcanic ridge (Mitchell 2001)

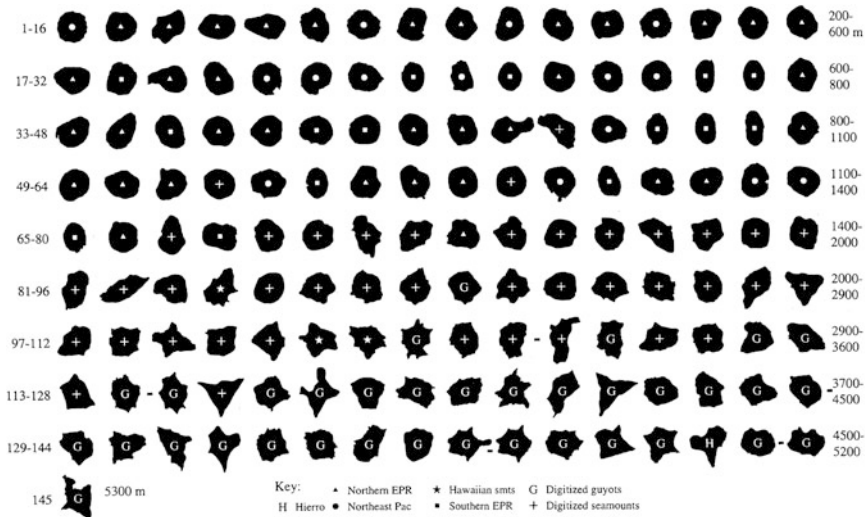


**Fig. 6.4** Compilation of midheight contours of seamounts arranged in order of increasing full height (given to the *right* of each row) and shown with scales normalized by dividing their dimensions by square root of area so that shapes of small and large seamounts can be compared (Mitchell 2001)

Guyots by Vogt and Smoot (1984). They proposed that the variation represents multiple stages of volcanic activity and mass wasting building up the volcanic edifice in case of the larger, stellate seamounts.

Small (<1 km high), mid-ocean ridge volcanoes are distinctly circular with a flat top. Various arguments suggest that the magma chambers beneath these volcanoes are probably shallow (Mitchell 2001). The circular shape and the flat top is explained by eruptions from ring dykes filling up the encircled region (e.g., McBirney and Williams 1969; Simkin 1972; Batiza and Vanko 1983). Involvement of cone sheets, rather than ring dykes have been proposed by various authors (e.g., Walker 1984; Mitchell 2001). The truncated cone form is explained by rising magma bodies stalling in the upper oceanic crust at the horizon of neutral buoyancy, producing ephemeral laccoliths. Inflation of these laccoliths produces cone sheets in the overlying crust, which are fed from the laccolith itself (Fig. 6.5a). The steep outer slope (~30°) is produced by disintegration of materials from the outermost cone sheets. The variable flatness of the summit (Smith 1996) is explained by variable laccolith depth, with deeper laccoliths producing flatter volcanoes, and sharp cones being produced by magma being erupted directly at the surface.

Clague et al. (2000) suggested that the volcanic cones grow by repeated caldera collapse and infill. Larger calderas grow in the early stages, which are filled and overflowed with lava, producing the edifice. Later calderas have a smaller diameter. Their repeated collapse and infill creates the circular shape with a flat top. Sagging

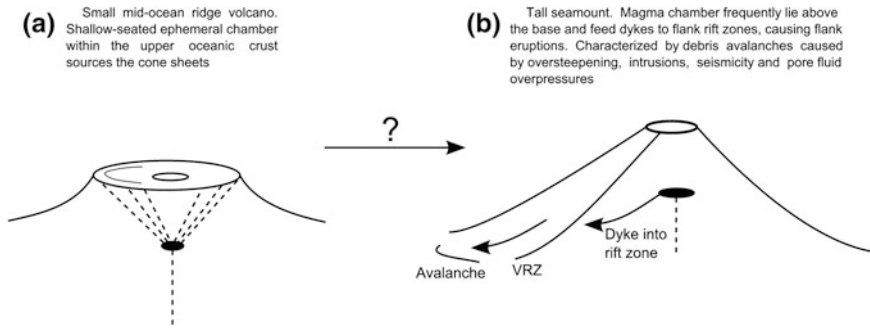


**Fig. 6.5** Speculative origin of seamount morphological end members (modified from Mitchell 2001). **a** Small mid-ocean ridge volcano, **b** Tall seamount. VRZ = Volcanic rift zones

and/or collapse during later eruptions can produce summit caldera/crater pits (Batiza and Vanko 1984; Fornari et al. 1984; Smith and Batiza 1989), and this mechanism is not incompatible with cone sheet intrusions.

Other proposed volcanic cone origins include doming over shallow sills and laccoliths (McBirney and Williams 1969; Cullen et al. 1987), and the magnitude of magma chamber pressure available during the eruption (Barone and Ryan 1990).

Change from a rounded to a stellate form depends on several factors. The edifice height is one of the most important ones to consider. An edifice height of  $\sim 3$  km, with a range from 2 to 4 km, is required for transition to the stellate form (Mitchell 2001; Fig. 6.5b), which coincides with the magma chamber top depths in Hawaii, Reunion and Krafla volcano (Ryan 1987; Necessian et al. 1996). The morphological complexity arises due to the magma chamber being situated above the edifice base (oceanic basement) (Head and Wilson 1992), with the position of the chamber rising with the horizon of neutral buoyancy. Ryan (1987) and Walker (1989) defined the horizon of neutral buoyancy as *the surface where the magma density equals the surrounding bulk rock density*. Below this horizon, the magma body is lighter than the surrounding bulk rock, and rises buoyantly to stall at the boundary. With the growth of the edifice, crack closure and dyke intrusion causes the horizon of neutral buoyancy to rise, and the magma chamber ponds at successively higher levels. Such shallow-seated magma chambers feed radiating flank ridges more efficiently than deep-seated magma chambers. Lateral dykes from shallow magma chambers escape along the horizon of neutral buoyancy (Lister and Kerr 1991). Dykes that overshoot the horizon of neutral buoyancy to meet the edifice surface, cause flank eruptions due to pressure differential between the seawater and magma chamber (Fig. 6.6), producing radiating volcanic ridges. The intrusions promote flank collapse by groundwater heating or slope oversteepening. Submarine slopes are steeper than subaerial slopes of the same volcano due to lower pressure difference available to drive a flank eruption (Lonsdale 1989; Fialko and Rubin 1999). In contrast, eruption from deep-seated magma chambers by vertical feeder dykes is less efficient (Lister and Kerr 1991) because of the longer path, work

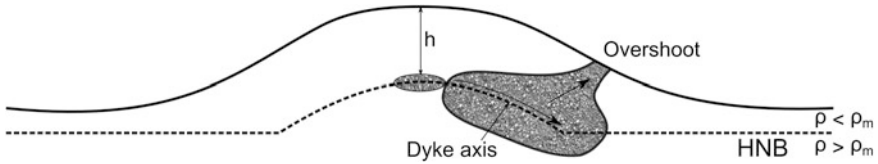


**Fig. 6.6** Magma bodies lying close to the horizon of neutral buoyancy (HNB) have lateral dykes escaping along the HNB (Lister and Kerr 1991). Where dykes overshoot the HNB to the edifice surface, a pressure difference between the magma source and seawater is available to drive flank eruptions (modified from Mitchell 2001)

against gravity, as well as volatile exsolution and density reduction, causing further ascent and eruption rather than lateral intrusion.

It should be noted that most of the small seamounts are probably monogenetic, while larger seamounts that grow over long period of time have a complex eruption and deformation history (Batiza and Vanko 1983; Fornari et al. 1987). Smaller seamounts (<1400 m) are almost all younger than 5 my, while larger edifices show a range of ages (Mitchell 2001), so that the complexity in form may also be a result of different edifice age. Numerous larger seamounts consist of more than one volcano, which adds to their irregular outline. Volcanic ridges (rift zones) in larger seamounts are independent of basement structures (Fiske and Jackson 1972). However, Wyss (1980) claims that volcanic rift zones in large edifices grow in response to tangential stretching over buoyant mantle plumes. In contrast, smaller volcanoes show features aligned with basement fabric (Batiza and Vanko 1983; Fornari et al. 1987).

### 6.3 Hotspot Volcano Spacing

Each hotspot trace is defined by a series of discrete volcanoes with a semi-regular spacing. The most studied example comes from the Hawaiian chain, where individual volcanic centers are spaced about 70 km apart. They seem to be arranged along parallel sigmoidal fractures subparallel to the chain (Jackson et al. 1972). The major hypotheses explaining such regular spacing of the hotspot volcanic cones are discussed below.

Vogt (1974) has proposed that the volcanoes form at intersection of fractures, the spacing of which is approximately equal to the thickness of the lithospheric plate. This is supported by fracture/volcano spacing in the older lithosphere being larger than that in the younger oceanic lithosphere. The plate above the hotspot acts like an extended object that fractures in the form of equidimensional blocks, producing the characteristic 40–100 km separation between hotspot volcanoes. Vogt (1974) also suggested that a volcanic conduit taps all magma within a given radius, so that neighboring volcanoes are rarely 10–20 km apart. Volcanoes form at any fracture-controlled site more than  $2h \tan \theta$  from the nearest volcano, where  $h$  is the

thickness of the lithosphere, and  $\theta$  is the dip of an upward narrowing cone, equal to  $25^\circ$ .

ten Brink (1991) has suggested that the spacing of hotspot volcanic cones is dependent on the flexural stress of the lithosphere controlled by the load of adjacent volcanoes (ten Brink and Brocher 1987). An elastic lithospheric plate, under stress from a point volcanic load, exhibits in-plane compressive radial stress in its upper part in the vicinity of the volcano, and tensional away from it (Fig. 6.7). At the inflection point between these stresses, the radial component becomes zero, although the tangential component remains. This stress reduction is sufficient to generate a path of hydraulic fracturing in the lithosphere that acts as a conduit to the volcano (Weertman 1971). The minimum distance between two adjacent volcanoes,  $r$ , is thus the inflection point of the radial stress component, which is given by (ten Brink 1991):

$$r = k.T_e^{3/4} \quad (6.1)$$

where  $T_e$  is the elastic thickness of the lithosphere, and  $k$  is a constant whose value depends on the Young's modulus of the lithosphere and the density difference between upper mantle and the moat fill. Observed hotspot volcano spacing, except large overlapping volcanoes, can be fit by the equation with a value of  $k$  between 4.76 and 6.06 for  $r$  and  $T_e$  in kilometers (Fig. 6.8). As the elastic thickness of the oceanic plate depends on its age during loading (Watts 1978), Eq. 6.1 can be modified as:

$$r = k.c^{3/4}t^{3/8} \quad (6.2)$$

where  $t$  is the age of the seafloor at the time of volcanic emplacement in million years, and  $c$  is a constant whose value is 4.2 (McNutt 1984) or 2.7 (Calmant et al. 1990). The relationship suggests that the distribution and spacing between volcanoes is influenced by the seafloor age during eruption.

Hieronymus and Bercovici (2001) have performed a parameter study of ten Brink's (1991) model, adding effects of stress change during magma transport through dykes. The dynamics of crack propagation in an elastic medium (see Turcotte 1982, 1981; Spence et al. 1987; Lister 1990; Lister and Kerr 1991) shows that fractures propagate through the lithosphere due to magma buoyancy. Solidification along the fracture walls may shut down the flow, until a new fracture forms. However, fractures over a critical width remain either open or may grow in width as long as a positive magmatic pressure remains (Bruce and Huppert 1990; Lister and Dellar 1996). The process involves melt-back and other erosional mechanism acting on the conduit wall, and can generate hotspot traces either as a continuous ridge or as discrete volcanoes (Hieronymus and Bercovici 1999). The amplitude of the plume stress vis-à-vis compressive flexural stresses produced by older volcanoes determines the volcano spacing. Once the first volcano is generated, it impedes further eruption in the vicinity due to growing flexural stresses. The next volcano only erupts when the plume has reached a position where the sum of

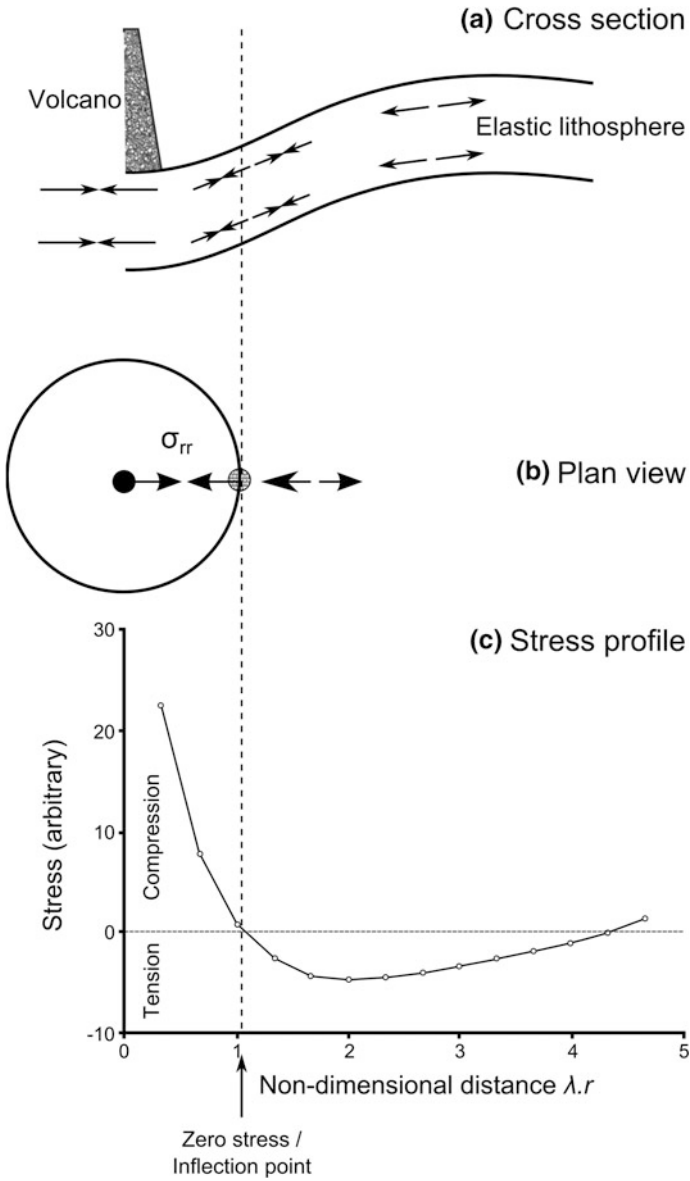


**Fig. 6.7** **a** Horizontal deviatoric stresses that accompany flexure of a thin elastic plate due to volcanic loading. **b** Distribution of radial stresses in the upper part of the plate due to volcano (solid circle). Large circle shows radius to inflection point where the radial stress changes become zero. **c** Profile of radial flexural stress due to point load on a thin elastic plate over a fluid substratum, as function of radial distance. Inflection point is at  $1.06\lambda$ , where  $\lambda$  is the flexural parameter, proportional to  $T_c^{3/4}$  (modified from ten Brink 1991)

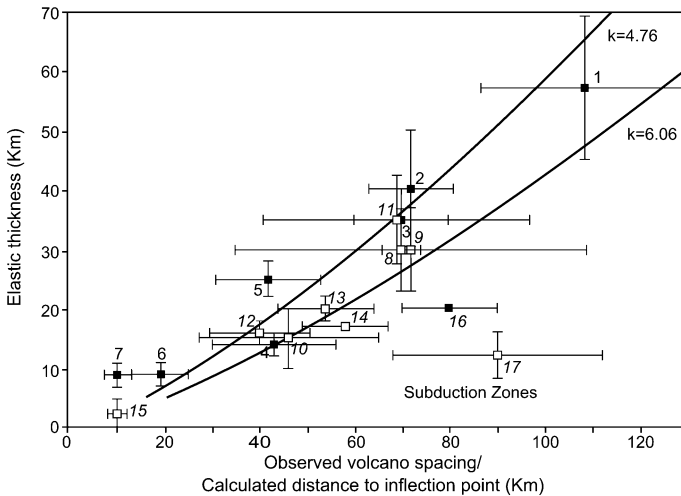


**Fig. 6.8** Comparison between measured volcano spacing data and modeled distance to inflection point (modified from ten Brink 1991). Numbered squares with error bars are volcano spacing in groups of volcanoes in East Africa (solid) and in oceanic hotspots (open) plotted against elastic thicknesses in these areas (numbers correspond to Table 1 of ten Brink 1991). The two curves show the calculated distance to inflection point (zero radial stress) for point-load model as a function of elastic thickness of the plate, corresponding to bracket values of  $k$  between 4.76 and 6.06

the stresses is barely balanced. For large enough plume stress, the distance decreases until it becomes zero, and a continuous ridge forms, overcoming flexural stresses near the center of the adjacent volcano. The model is more general than that of ten Brink (1991) and contains it as a subset. In this model, the volcano spacing varies depending on the volcano size, and the formation of a volcanic cone depends on a complex interplay of different variables instead of the simple flexural rigidity of ten Brink’s model. It thereby prevents deducing a functional relationship. Also the distance between the load and point of zero flexural stress is larger due to flexural effects from all volcanic loads, which predicts greater spacing (1.72, instead of 1.06 $\lambda$ ).

### 6.4 Magma Flux Variation

The variability of hotspot volcanism with time can be expressed in terms of the magma volume flux as determined (indirectly) either from the volume of volcanic material erupted, measured from the volume of the volcanic edifices and their roots, or from the plume-related uplift (swell). Geochemical evidences (e.g., La/Nb and Sr/Nb ratio) for the Hawaiian plume suggest that it is zoned in terms of temperature and melting rate (DePaolo et al. 2001). Each shield may have been formed from a

compositionally different source (Putrika 1999), reflecting differences in mantle upwelling processes (Frey et al. 1994). Consequently, the plume temperature anomaly is not constant throughout the hotspot history, and temporal variations in plume volume flux cannot be directly calculated (Vidal and Bonneville 2004).

There are three different approaches to the problem, depending on whether one chooses the buoyancy (or mass) flux of the plume (e.g., Davies 1988, 1992; Sleep 1990), the plume volume flux (e.g., Sleep 1990; Ribe and Christensen 1994), or the igneous volume flux produced by hotspot melting as the determining parameter. The last method is commonly used to calculate the magma volume flux with time, as measured from the erupted volcanic materials determined from bathymetric and/or gravity anomaly (e.g., Bargar and Jackson 1974; White 1993; Van Arc and Lin 2004; Vidal and Bonneville 2004). The Hawaii-Emperor chain is the test bench for these studies, as it is the longest, intra-plate hotspot track in the world, devoid of ridge interactions, and offers a continuous record of hotspot flux variations for about the last 70 million years (Fig. 6.9).

Van Arc and Lin (2004) prepared a volume per unit time plot along the Hawaiian hotspot track, using a crustal thickness map derived from gravity anomaly inversion, a reference oceanic crust thickness of 6 km, and plate velocities for the Hawaiian (8.3 cm yr<sup>-1</sup>, Gordon and Jurdy 1986) and Emperor Chains (5.77 ± 1.92 cm yr<sup>-1</sup>, Tarduno et al. 2003), which they used as a proxy for igneous production over time. Their results for the Hawaiian chain indicate a low volcanic production rate of less than 4 m<sup>3</sup> s<sup>-1</sup> between 25 and 40 my, increasing to about 8 m<sup>3</sup> s<sup>-1</sup> at 20 my, a low rate of 4 m<sup>3</sup> s<sup>-1</sup> between 8 and 18 my, and an increase again to 8 m<sup>3</sup> s<sup>-1</sup> in recent time (Fig. 6.10). The Emperor Chain shows an overall low volcanic production rate

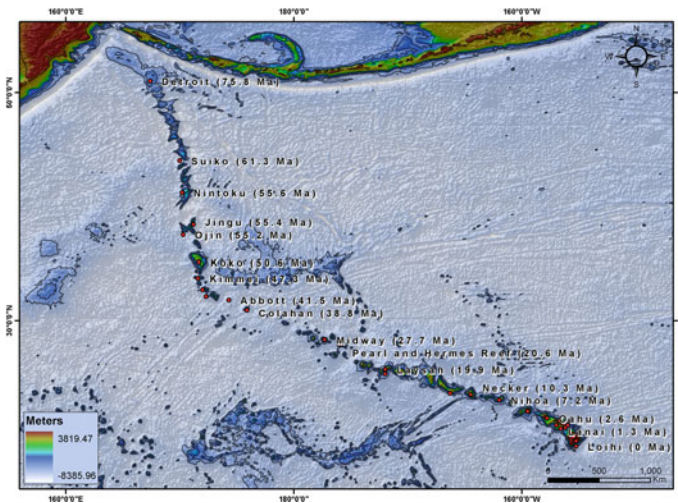


**Fig. 6.9** Map of the Hawaii-Emperor chain with ages of seamounts and islands (redrawn after Molnar and Stock 1987). Red dots show the approximate position of the Hawaiian hotspot at that time

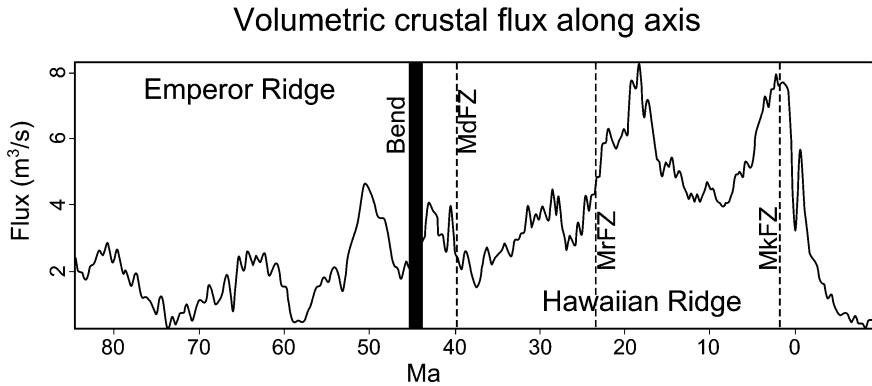


**Fig. 6.10** Igneous volume flux for the Hawaii-Emperor hotspot track (modified after Arc and Lin 2004). The *thick black line* shows the location of the bend in the hot spot chain, and the *dashed lines* show the location of major fracture zones in the Pacific (MkFZ, Molokai fracture zone, MrfZ, Murray fracture zone, MdFZ, Mendocino fracture zone)

with two minima at about 58 and 74 my. Overall, the low flux periods at 25–48, 58 and 74 my correlate with the noticeably smaller height and size of the seamounts as compared to those of high-flux periods. Grossly similar results were obtained by White (1993) and Vidal and Bonneville (2004), both of which show a high magmatic production between 0 and  $\sim 25$  my, with a minima at  $\sim 10$  my, for the Hawaiian chain, and a much lower flux in the Emperor Chain. The present-day magma production rate of more than  $12 \text{ m}^3 \text{ s}^{-1}$  given by Vidal and Bonneville (2004) is much greater than that of Van Arc and Lin (2004), which may be due to lack of gravity data over the Hawaiian island.

The wide variation in the magma production rate in the Hawaii-Emperor chain led Phipps Morgan et al. (1995) to hypothesize that the observed variations in igneous flux are due to the changes in the lithosphere as the Pacific fracture zones cross the stationary mantle plume. The model envisages a younger, warmer lithosphere in the Hawaiian chain enabling the plume to rise higher, melting a larger fraction. However, it fails to account for the variations in the Emperor Chain lacking fracture zones, and the flux reduction at  $\sim 10$  my within the Hawaiian chain. Short-term variations in the magma flux may be due to tilt in the plume conduit (Steinberger and O’Connell 1998; Steinberger 2000) as the plume adjusts to changes in absolute plate motions, caused by changes in large-scale mantle convection. Presence of solitary waves (Scott et al. 1986; Olson and Christensen 1986; Whitehead 1987; Olson 1990) caused by variable melt entering the plume conduit from the lower mantle boundary layer (Sleep 1992) may lead to hotspot flux variations, and have been used to explain V-shaped ridges near the Iceland and Azores hotspot (Escartin et al. 2001; Ito 2001). Geochemical analysis of the volcanic rocks (e.g., Regelous et al. 2003) may be combined with the geophysical studies to distinguish between these various mechanisms of plume flux variations.

## 6.5 Heat Flow and Hydrothermal Circulation

Discrepancy between heatflow values predicted by thermal models of cooling lithosphere (e.g., Parsons and Sclater model, PSM, and global depth and heat flow model, GDH1, Parsons and Sclater 1977, Stein and Stein 1992) and lower values measured for the 0–70 my old seafloor, is generally interpreted to reflect significant amount of heat transport and cooling by circulating seawater (Lister 1972; Williams et al. 1974; Anderson and Hobart 1976), rather than conductive cooling assumed in the models. The circulation is divided into two mechanisms (Lister 1982; Fehn and Cathles 1986): an active circulation near the ridges, in which water cools and cracks the rocks with rapid extraction of heat by high-temperature water flow (Paterson and Lowell 1982; Fehn et al. 1983), and a passive circulation transporting lower-temperature water on the ridge flanks. The magnitude of this heat flow discrepancy is the primary factor used to estimate the volume and age distribution of the hydrothermal water flux (Wolery and Sleep 1976; Sleep and Wolery 1978; Anderson and Skilbeck 1981). As this difference is highest at the ridge and decreases with age, it indicates a similar decrease in hydrothermal activity with age, until the “sealing” age, whereby all hydrothermal activity ceases (Stain and Stain 1994) (Fig. 6.11).

Using the GDH1 model as reference, Stain and Stain (1994) estimated that about 34 %, or  $11 \times 10^{12}$  W, of the predicted global oceanic heat flux of  $32 \times 10^{12}$  W occurs by hydrothermal flow, which is in good agreement with  $10 \times 10^{12}$  W value obtained by Sclater et al. (1980). Cumulative hydrothermal heat flux for crustal ages of 1, 2 and 4 my gives values of 3.2, 4.2, and  $5.4 \times 10^{12}$  W respectively, corresponding to 29, 38 and 49 % of the total hydrothermal heat flux (Table 6.1), indicating that about 30 % of the hydrothermal heat flux occurs in oceanic crust younger than 1 my (Fig. 6.12). The sealing ages for the different oceans are consistent, corresponding to a value of  $65 \pm 10$  my, in contrast to lower sealing ages ( $\sim 20$  my) obtained in earlier studies (e.g., Wolery and Sleep 1976; Sleep and Wolery 1978). The factors contributing to the decrease in hydrothermal heat flux with age seem to be the sediment cover and lithospheric age. Anderson and Hobart (1976) proposed a sediment cover of 150–200 m isolating the crustal convective system from the ocean, while Anderson et al. (1977) showed a decrease in crustal (oceanic layer 2A) permeability with age due to mineral deposition. Subsequent authors (e.g., Anderson and Skilbeck 1981; Jacobson 1992) often combined the two effects to explain the flux decrease. Stain and Stain (1994) showed that even the least sedimented areas show a decrease in hydrothermal heat flow with age, while the heat flow discrepancy exists even at heavily sedimented locations for ages up to 50 my, concluding that lithospheric age has the primary control on the fraction of heat transport by hydrothermal flow, with sedimentation having a lesser effect.

In volcanic islands and the associated sedimentary aprons, a complex fluid flow pattern evolves as an effect of interaction between compaction-driven flow and convective hydrothermal circulation. Finite element modeling of fluid flow and pore pressure distribution during the growth of a volcanic edifice and the associated mass

**Fig. 6.11** Heat flow anomaly due to hydrothermal flux compared to the global depth and heat flow (GDH1) cooling model for oceanic crust of different ages (Stein and Stein 1994). The data is represented in the raw form (*top*) as well as fraction of the predicted heat flow (*bottom*)

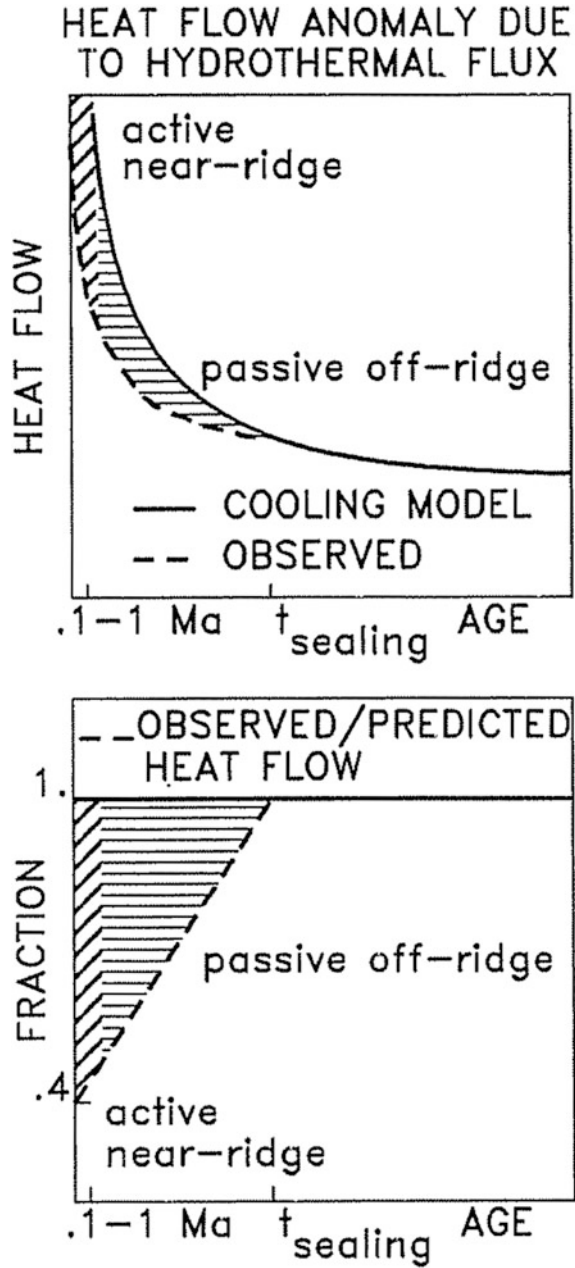
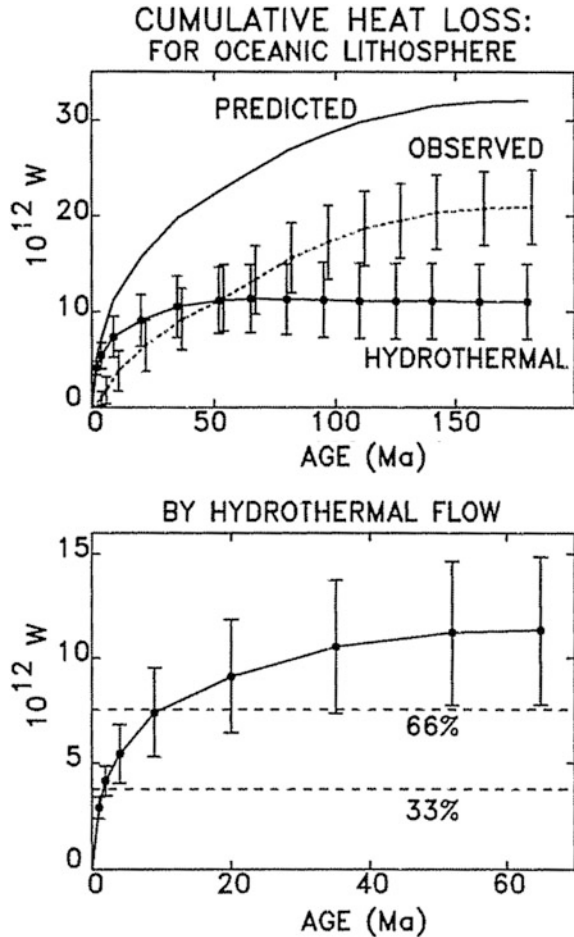


**Table 6.1** Predicted and observed average heat flow (top) and cumulative heat flux (bottom) for oceanic crust of different ages (Stein and Stein 1994)

Age (Ma)	Area ( $10^6 \text{ km}^2$ )	Average heat flow ( $\text{mW m}^{-2}$ )	
		Predicted	Observed
0–1	3.5	1020	$131 \pm 93$
0–2	7.1	721	$136 \pm 99$
0–4	14.2	510	$128 \pm 98$
4–9	19.7	204	$103 \pm 80$
9–20	31.8	136	$82 \pm 52$
20–35	42.6	98	$64 \pm 40$
35–52	37.0	77	$60 \pm 34$
52–65	29.7	6	$62 \pm 26$
65–80	37.3	60	$61 \pm 27$
80–95	27.9	56	$59 \pm 43$
95–110	24.8	53	$57 \pm 20$
110–125	15.2	51	$53 \pm 13$
125–140	16.7	50	$52 \pm 20$
10–160	8.3	49	$51 \pm 14$
160–180	3.4	48	$52 \pm 10$
Age (Ma)	Cumulative heat flux ( $10^{12} \text{ W}$ )		
	Predicted	Observed	Hydrothermal
1	3.6	$0.4 \pm 0.3$	$3.2 \pm 0.3$
2	5.1	$1.0 \pm 0.7$	$4.1 \pm 0.7$
4	7.2	$1.8 \pm 1.4$	$5.4 \pm 1.4$
9	11.3	$3.8 \pm 2.1$	$7.4 \pm 2.1$
20	15.6	$6.5 \pm 2.7$	$9.1 \pm 2.7$
35	19.8	$9.2 \pm 3.2$	$10.5 \pm 3.2$
52	22.7	$11.5 \pm 3.4$	$11.2 \pm 3.4$
65	24.6	$13.3 \pm 3.5$	$11.3 \pm 3.5$
80	26.9	$15.6 \pm 3.7$	$11.3 \pm 3.7$
95	28.5	$17.3 \pm 3.9$	$11.2 \pm 3.9$
110	29.8	$18.7 \pm 3.9$	$11.1 \pm 3.9$
125	30.6	$19.5 \pm 3.9$	$11.1 \pm 3.9$
140	31.5	$20.4 \pm 3.9$	$11.1 \pm 3.9$
160	31.9	$20.8 \pm 3.9$	$11.1 \pm 3.9$
180	32.0	$21.0 \pm 3.9$	$11.0 \pm 3.9$

wasting events indicates that the fluid flow regimes comprise of two stages (Christiansen and Garven 2004a, b). In the early phase of volcanic construction, compaction-driven flow dominates the regime with minor buoyancy-driven circulation. Fluid is expelled from the sediments and crust below the edifice towards the flexural arch along the permeable upper part of the oceanic crust. As the edifice grows, a convective circulation pattern develops below it, and becomes more vigorous with continued volcanic growth. Accordingly, the flow pattern is

**Fig. 6.12** Cumulative heat loss from oceanic crust of different ages due to hydrothermal circulation (Stein and Stein 1994). The predicted, observed and inferred hydrothermal heat fluxes are shown, with error bars of one standard deviation. Data come from Table 6.1. The lower picture shows the percentile values of the cumulative hydrothermal heat flux



controlled both by the compaction and convective circulation. As rapid sedimentation decreases, compaction-driven flow diminishes and convective flow dominates the remainder of the seamount evolution, with a change in fluid flow direction towards the edifice (Fig. 6.13). The compaction-driven circulation is primarily controlled by the pre-volcanic sediment thickness, sedimentation rate and mass of the volcanic edifice, while the hydrothermal system is driven by the edifice height and lithospheric flexure (Christiansen and Garven 2004b). Excess pressure develops in the pelagic sediments and upper crust below the edifice during the initial phases of volcanic growth that dissipates with decreasing sedimentation. The fluid velocities in this system are small ( $<0.5 \text{ cm yr}^{-1}$ ), but have important implications for slope stability. Under certain conditions, the pore pressure may exceed the lithostatic pressure, leading to unstable edifice conditions. The sedimentation causes a decrease in surface heat flow, by as much as  $20 \text{ mW m}^{-2}$  for Hawaii (Fig. 6.14)

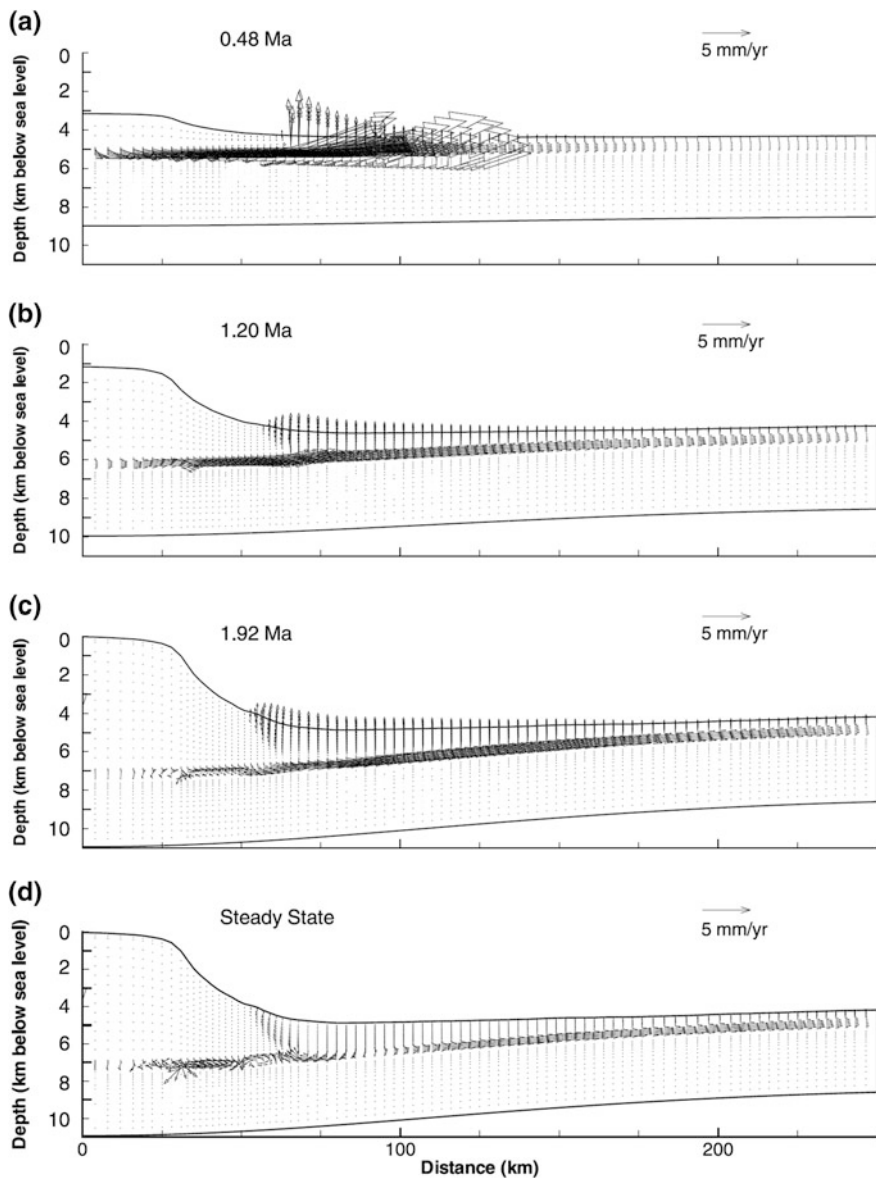


**Fig. 6.13** Fluid flow vectors from Hawaiian simulation (Christiansen and Garven 2004a). Time steps shown are 0.48, 1.20 and 1.92 my after beginning of volcanism, and after the system attains steady state (at 5.80 my). Arrowhead size is proportional to the length of the vector

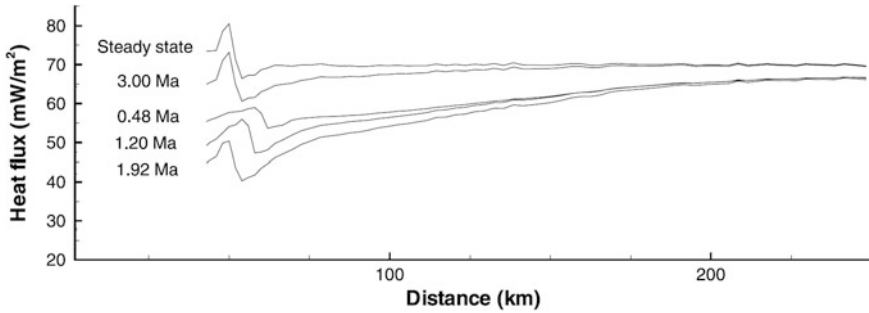


**Fig. 6.14** Heat flux values across the volcanic edifice slope and the sedimentary apron (Christiansen and Garven 2004a). The time steps at 0.48, 1.20, 1.92, 3.00 my and at the steady state corresponds to the simulation steps in Fig. 7.15

due to addition of cold ( $\sim 0$  °C) sediments. The effect is most pronounced over the flexural moat where the sedimentation rate and thickness are highest. Once sedimentation ceases, the surface heat flux rebounds to the approximate initial values, with small variations near the edifice due to variation in thermal conductivity and convective fluid circulation (Christiansen and Garven 2004a, b).

Based on the swell height and the thermal reheating model (Crough 1978, 1983), a maximum thermal anomaly of  $\sim 25$   $\text{mW m}^{-2}$  is predicted within 15–20 my of reheating for the Hawaiian hotspot. The small measured heatflow (Von Herzen et al. 1989; Stein and Stein 1993) indicates that the swell may be formed due to dynamic uplift, with heat conduction from the base of the lithosphere taking tens of millions of years to reach the surface (implying an anomaly of less than  $1$   $\text{mW m}^{-2}$ , Ribe and Christensen 1994). Hydrothermal circulation suppressing heat flow to the surface have been put forward (Harris et al. 2000a, b) to explain the lack of high heat flow at hotspot location. Heat flow measurements from five oceanic hotspots, Hawaii, Reunion, Crozet, Cape Verde and Bermuda, show heat flow anomaly values of 5–10, 6, 14, 9 and 8  $\text{mW m}^{-2}$ , respectively (Stein and Von Herzen 2007), measured with respect to the GDH1 model. The small anomalies, together with the lack of any Gaussian distribution of anomaly values (Von Herzen et al. 1989; Stein and Stein 1993; DeLaughter et al. 2005) indicate the absence of significant lithospheric reheating, and smaller (than the suggested 300 km diameter, in Crough 1978) thermal imprint of the plume materials. The measured anomalies can adequately be explained based on total heat contribution from a cooling magma and conductive cooling of an underplated sill complex, together with thermal blanketing by sediments (Fig. 6.15). Stein and Von Herzen (2007) concluded that hydrothermal circulation may redistribute heat within  $\sim 200$  km of the swell axis, but cannot mask the large, broad heatflow anomaly arising from reheating of the lower lithosphere. An additional factor against hydrothermal removal of heat from the hotspots is the low permeability of sediments preventing vertical flow of water (e.g., Spinelli et al. 2004), and consequent ineffective advective heat transfer;

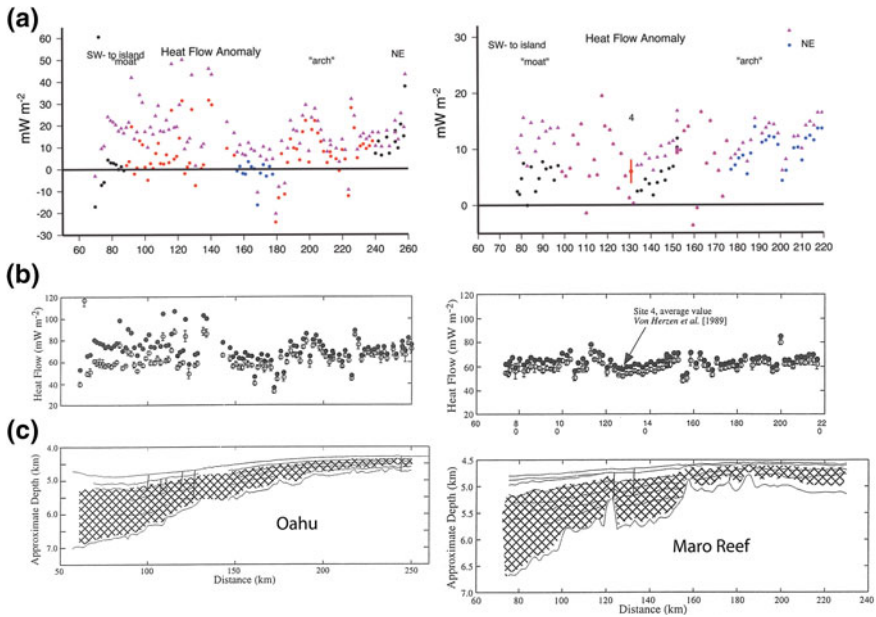


**Fig. 6.15** **a** Heatflow anomalies, **b** measured and sediment-corrected heatflow, and **c** depth-converted seismic reflection profiles for Oahu and Maro Reef, Hawaii (Stein and Von Herzen 2007). The *top panels* show the heatflow anomalies for the measured (*solid circles*) and sediment-corrected (*purple triangles*) heatflow. *Blue circles*—no hydrothermal circulation inferred; *red circles*—hydrothermal circulation inferred; *black circles*—no determination of circulation. The middle panel shows the measured (*open circles*) and sediment-corrected (*solid circles*) heatflow values. The *middle and lower panels* are from Harris et al. (2000a)

however slow horizontal flows are possible. Interpretation of 58 heat flow surveys (Von Herzen 2004) indicates only 27 % having probable convective heat flow, mostly within 200 km of the swell axis.

## 6.6 Flexural Moat and Arch—Spatial and Temporal Development

Flexure at seamounts is caused by distributed load in the interior of an oceanic plate. Flexural moats are trough-like depressions that form around large seamounts due to lithospheric flexure of the increasing volcanic load (Menard 1964). Away from the central load, the isostatic upwelling results in a broad, peripheral swell of the seafloor, termed as flexural bulge (arch) (Fig. 6.16). The geometry of the moat depends on the size of the volcanic load and strength of the underlying lithosphere, represented by its elastic thickness. Once formed, the moat gets filled with volcano-clastic and mass-wasting deposits from the adjacent volcano.

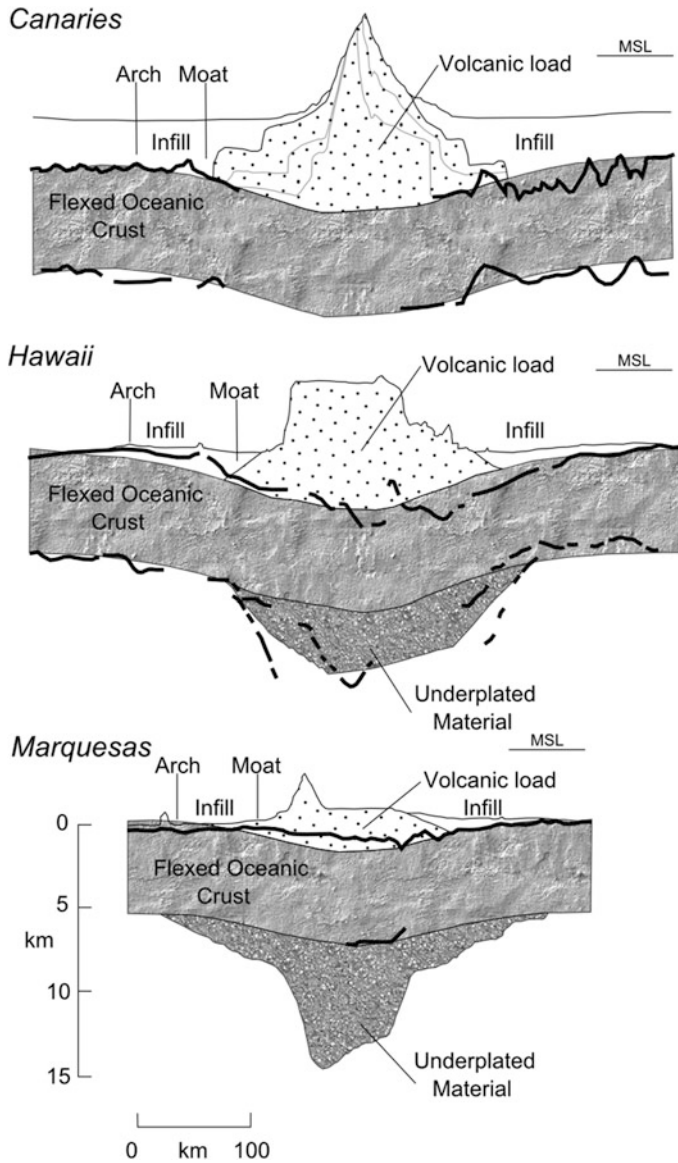


**Fig. 6.16** Transects across Canary Islands, Hawaii Islands and Marquesas, showing the development of the flexural moat and arch (modified from Watts et al. 1997)

The best known example comes from Hawaii, where the flexural moat, known as the Hawaiian Deep (Hamilton 1957; Menard 1964), parallels the Hawaiian ridge and forms a trough with a radius of 140 km at the south-eastern end of the Island chain. The flexural bulge, known as the Hawaiian Arch (Menard 1964), is located at

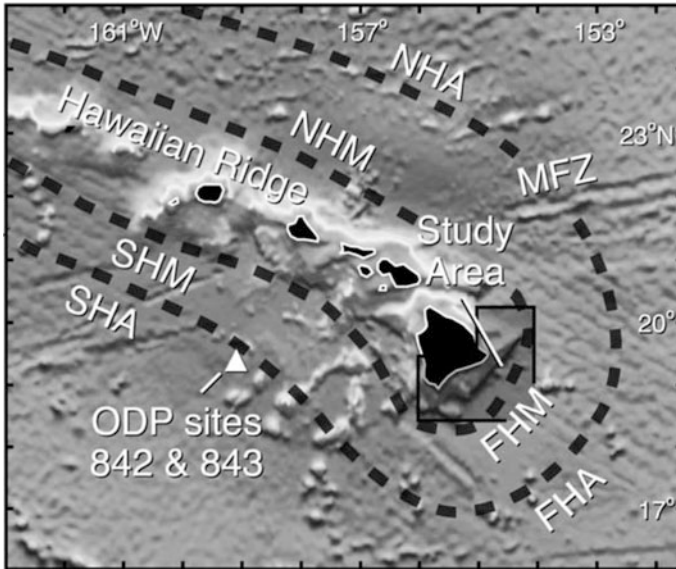


**Fig. 6.17** Shaded-relief bathymetric map of the Hawaiian Ridge and surrounding flexural moat and arch (Leslie et al. 2002). Refer Fig. 2.10b for further details

~250 km seaward from the islands. The moat and the bulge have flanking segments (North/South Hawaiian Moat/Arch) and frontal regions (Frontal Hawaiian Moat/Arch), based on their location with respect to orientation of the island chain (Fig. 6.17). The frontal structures, in the direction of the volcanic ridge development, are short-lived features, which migrate with successive volcanic loads, the older ones being eventually covered by the growing Hawaiian ridge as the Pacific plate drifts over the Hawaiian hotspot. In contrast, the flanking segments are essentially permanent features that fill with sediments over time. Moat to arch relief within the flanking segment can be >1 km, while it is ~200–450 m in the frontal moat, indicating less subsidence of oceanic crust in the frontal regions (Leslie et al. 2002).

Immediately after the emplacement of the volcanic load, rapid ( $10^4$ – $10^5$  year) thinning of the mechanically strong part of the oceanic lithosphere occurs by thermally activated creep, reducing it to its long-term elastic thickness. Within the first ~1 my, the moat deepens, and the peripheral bulge migrates towards the load (Bodine et al. 1981). The flexural effects of a migrating load, such as the island of Hawaii, had been studied in detail by Watts and ten Brink (1989). In their study, the oceanic plate has been assumed to have a constant rigidity (elastic plate) and the stratigraphic thicknesses were computed along the axial, across, and flank parts of the volcanic load. The thicknesses were calculated after computing the flexure caused by each new load as the volcanoes migrate, and superposing that on the flexures associated with the pre-existing loads (Fig. 6.18). Calculations show that the plate gets depressed by about 4–5 km by the addition of new volcanoes

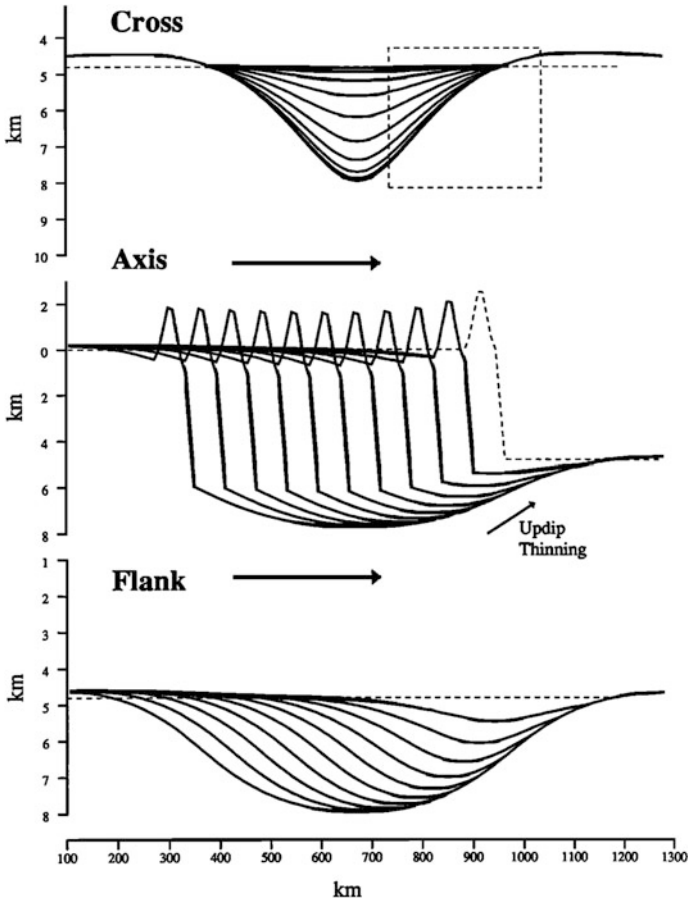


**Fig. 6.18** Calculated flexural curves along the moat, island axis and across a migrating volcanic load, assuming a constant migration and sedimentation rate, a constant rigidity of the plate and a circular load approximately the size of Hawaii (Watts and ten Brink 1989)

upstream, which also caused the flanking uplifts to rise by several hundred meters. As a result of this cumulative flexure, 5 km high islands get depressed by about 2.5 km, and downstream islands get tilted towards the new load. The horizontal sediments infilling the moat also get tilted by about  $2^\circ$ , generating a striking pattern of stratigraphic offlap and onlap, in the direction of load migration (Fig. 6.19).

### 6.6.1 Deposition in Flexural Moat

The depositional history in flexural moats surrounding large oceanic islands is a record of short-term ( $<10^6$  year) changes in lithospheric strength, generating a

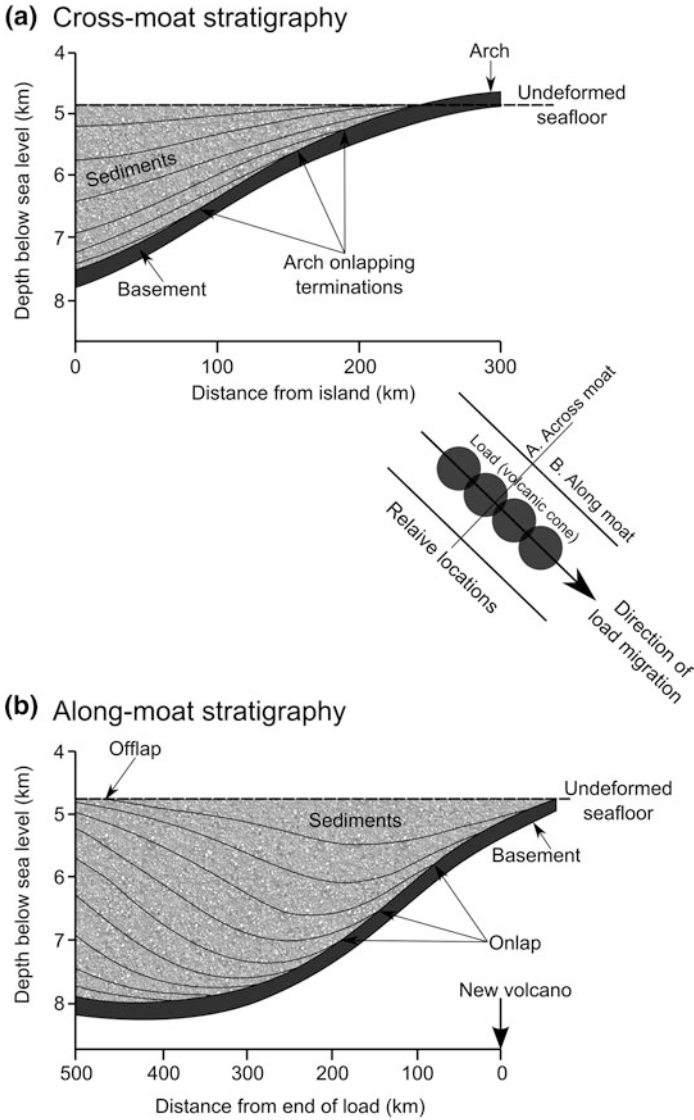


**Fig. 6.19** Synthetic seismic stratigraphy of sediments in the Hawaiian flexural moat predicted by modeling the effect of a circular load on the surface of an elastic plate, assuming a constant sedimentation rate (modified from Rees et al. 1993)

distinctive pattern of stratigraphic onlap and offlap on cross-moat profiles (ten Brink and Watts 1985; Fig. 6.19). The offlap patterns are characterized by downdip thickening and increase in dip, while the onlap patterns show updip thinning, closely resembling clinofoms in deltaic sequences (Watts and ten Brink 1989).

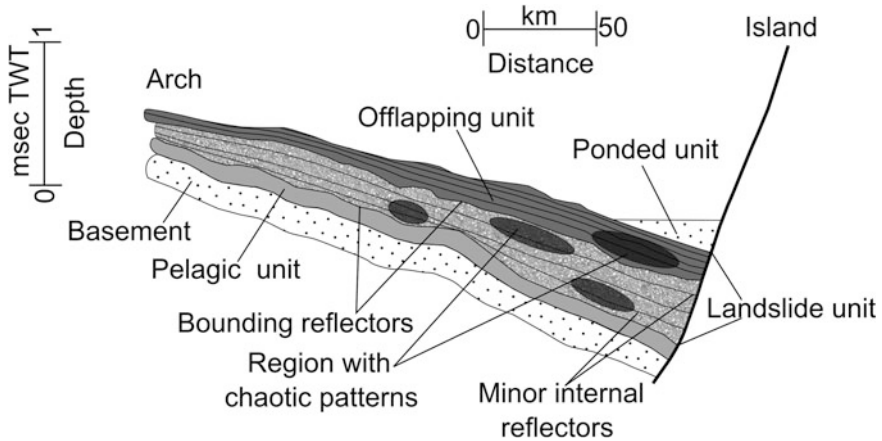


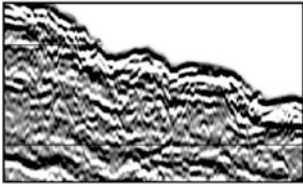
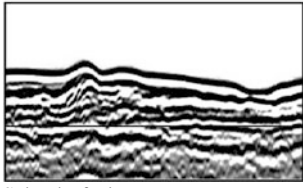
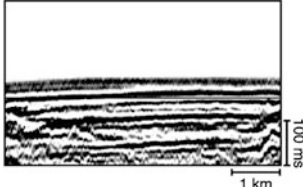
**Fig. 6.20** Idealized stratigraphy of the Hawaiian moat (modified from Rees et al. 1993)

Large-scale mass wasting is the primary source of sedimentation in the moat, as documented along the Hawaiian ridge (Moore et al. 1989). There are two distinct types of mass wasting features identified from sonar images; slumps and debris avalanches. The slumps are broad, coherent slope failures, having a steep scarp at their toe. They are thought to move slowly or intermittently downslope (Vernes 1978). In contrast, the debris avalanches are narrower and longer mass wasting features that extend hundreds of kilometers from their source region (Moore et al. 1994), resulting in a broad apron of hummocky terrain in the distal part. They represent single episodes of rapid failure (Moore et al. 1989). Voluminous, submarine lava flows are also present in the Hawaiian deep (Holcomb et al. 1988).

Reflection seismic surveys around the Hawaiian ridge have been used by various authors (Watts et al. 1985; ten Brink and Watts 1985; Lindwall 1988; Rees et al. 1993) to characterize the seismic stratigraphy of the flanking segments of the Hawaiian moat. An extensive study by Rees et al. (1993) defined four stratigraphic units infilling the northern Hawaiian moat: (1) a basal pelagic unit of constant thickness, (2) a thick wedge of landslide units onlapping the Hawaiian Arch, (3) a highly reflective, continuous unit offlapping the arch, and (4) a ponded unit of near-horizontal unit in the deepest part of the moat (Fig. 6.20).

1. **Basal unit:** The lowermost unit over the basement has approximately uniform thickness. It drapes over and infills the rough topography. The layer is laterally extensive, weakly reflective, and has a thickness of typically less than 200 m (Winterer 1989; ~80–100 m according to Leslie et al. 2002). It is interpreted to be formed by pelagic sediments predating the moat (Rees et al. 1993).
2. **Landslide unit:** Overlying the basal layer is a thick wedge of sediments that thickens towards the island and progressively onlaps the flexural arch on the other side. It constitutes the bulk of the moat deposits, and comprises of a series of lens-shaped sub-units, each with a central zone with chaotic reflection pattern,

**Table 6.2** Seismic reflection facies identified within the landslide unit in the Hawaiian moat (Leslie et al. 2002)

Seismic facies	Characteristics	Geological interpretation
 <p>Seismic facies A</p>	Highly chaotic/incoherent areas containing few internal reflections, often bordered by continuous reflections	Proximal debris avalanche or lower slump deposits
 <p>Seismic facies B</p>	Hummocky and/or chaotic sequences of reflections that thin with distance from the island edifice and onlap or downlap underlying reflections	Distal debris avalanche or debris flow deposits
 <p>Seismic facies C</p>	Sequences of continuous, parallel, generally flat-lying reflections that 'pond' in low areas and onlap underlying reflections	Turbidites

and relatively thin, highly reflective continuous horizons to the top, below and extending away from it, often exhibiting landward diverging reflection geometry (Leslie et al. 2002). Its thickness is greatest ( $\sim 700$  m) adjacent to large erosional features alongside seamounts (Rees et al. 1993), and thins rapidly away from it. Its sediments are interpreted to be volcano-clastic debris avalanche and debris-flow deposits derived from the volcanic slope failure (Rees et al. 1993; Leslie et al. 2002). Three distinct seismic facies can be identified within the landslide unit (Leslie et al. 2002), as described below (Table 6.2):

- a. **Facies A (Proximal debris avalanches and slumps)** – These are thick sequences with chaotic and incoherent reflection patterns and irregular blocks adjacent to steep ( $> 5^\circ$ ) volcanic slopes. They are present within a wedge or slope apron flanking the lower slopes of submarine volcanoes, and represent locally-derived poorly sorted volcano-clastic debris (Fig. 6.21).
- b. **Facies B (Distal debris avalanches and debris flows)** – These are characterized by hummocky and/or chaotic lensoidal reflection patterns onlapping the frontal arch, occurring as thick sequences at or near the boundary between the lowermost volcanic slopes and the abyssal plains. These become

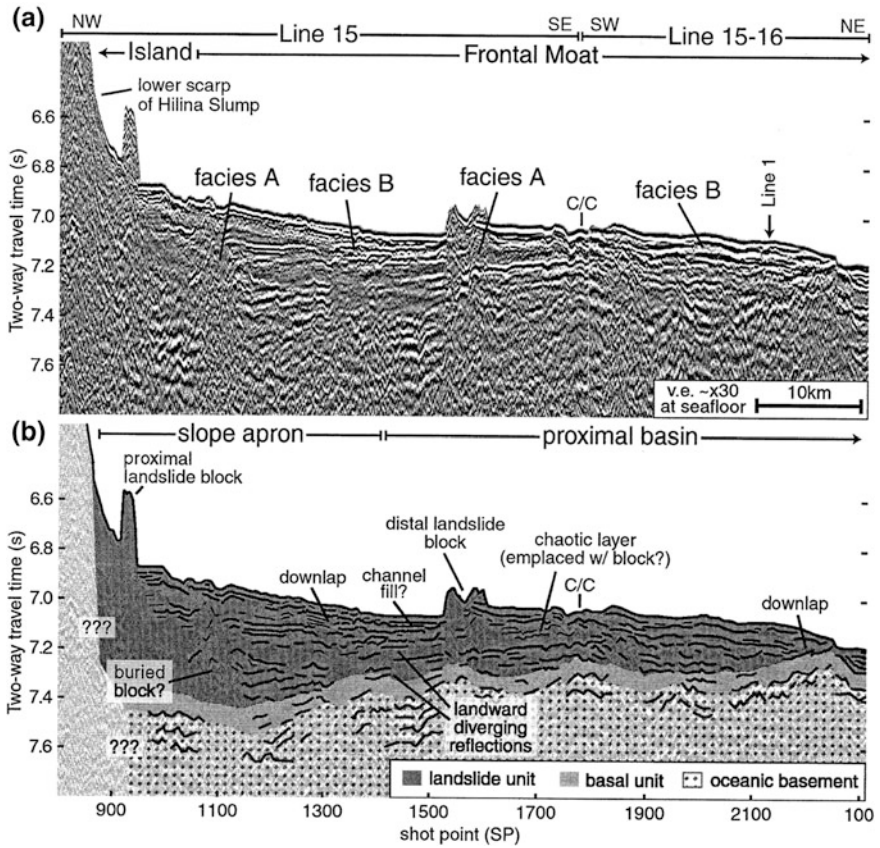


**Fig. 6.21** Seismic reflection profile across the Frontal Hawaiian Moat (a) and its interpretation (b) (Leslie et al. 2002)

thinner towards the arch, and eventually merge with facies C units. These are interpreted as chaotic debris flow and avalanches from the nearby volcanic slopes (Fig. 6.21).

c. **Facies C (Turbidites)** – These are recognized a high amplitude, high frequency continuous and parallel reflection patterns that overlie and onlap the pelagic deposits in the distal parts of the moat. Individual reflections dip gently towards the Hawaiian ridge. The deposits have a strong basement control in their distribution, indicating influence of current-controlled depositional processes. They are interpreted as turbidite deposits from mass-wasting events (Fig. 6.21).

3. **Offlapping unit:** These are a sequence of highly reflective, continuous horizons that are present overlying (and sometimes interbedded with) the landslide units. They offlap towards the arch and thicken towards the moat. The sequence is

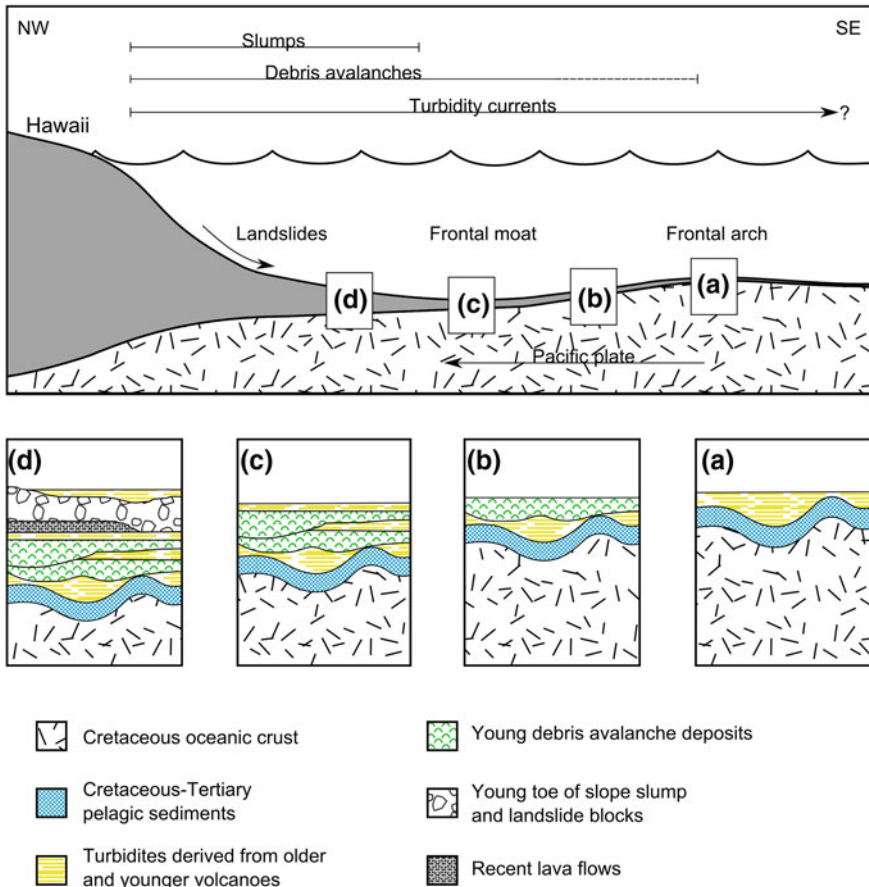


**Fig. 6.22** Schematic depiction of the predicted stratigraphy of the Hawaiian Moat and Arch (modified from Leslie et al. 2002). **a** Turbidites and pelagic sediments on the Hawaiian Arch. **b** Gradually thicker volcano-clastic deposits approaching the Frontal Hawaiian Moat. **c** Debris avalanche and turbidity current deposits dominating along the axis of the moat. **d** Thickest accumulation of sediments overlain by slump deposits predicted at the toe of the volcanic edifice

thickest in basins between major mass-wasting deposits, and is interpreted either as distal landslide facies (in that respect the same as facies C of Leslie et al. 2002) or turbidites associated with smaller-scale slope failures during the continued subsidence of the moat (Rees et al. 1993).

4. **Ponded unit:** These units, imaged as strong coherent reflection patterns, are present in the deepest parts of the moat. The deposits have a strong discordant relationship with the underlying (mostly offlapping) units (indicating a depositional hiatus), and are of limited aerial extent and variable thickness, reaching a maximum of  $\sim 185$  m in local depressions adjacent to the ridge. The reflections are nearly horizontal, indicating little post-depositional subsidence of the ridge.



◀ **Fig. 6.23** Schematic model showing history of moat deposition (Rees et al. 1993). Panels show map views and idealized cross sections of the moat in its four main stages of development. The relative importance of subsidence and sediment input are shown by the sizes of the downward- and upward-pointing arrows, respectively. Numbered circles on maps are individual volcanoes that progressively form as the plate moves across the hotspot

Their origin is unclear, and can be deposited either during uplift of older islands, or unique events like Pleistocene sea level low-stand (Rees et al. 1993).

The spatial distribution of moat sediments shows interplay between depositional processes, volcanic activity and plate flexure, resulting in a predominantly upward coarsening stratigraphy in the Hawaiian frontal moat (Leslie et al. 2002; Fig. 6.22). The predominant sequence grades upward from a pelagic sediment, turbidite sequence, distal debris flow avalanches, and finally proximal debris flow deposits, interbedded with lava flows, particularly near volcanic rift zone terminations (Leslie et al. 2002).

### 6.6.2 History of Moat Deposition

The stratigraphic sequence in the Hawaiian moat results from the dynamic influence of sediment influx from large scale mass wasting events, and flexural subsidence of the oceanic plate from successive loads of the newly formed volcanoes (Rees et al. 1993). As the sedimentation and subsidence rates never become equal, the moat deepens, and remains under-filled during periods of high subsidence (compared to sedimentation rates), while the moat gradually fills up with sediments during high rates of sedimentation. During the development of the moat, there is a gradual and systematic change in the subsidence and sedimentation rates, giving rise to a distinctive package of sediments described earlier. Four different stages of moat development are described below (Fig. 6.23):

- A. **Stage 1:** During the initial stages, as a new volcano forms over the oceanic crust, it subsides and rapidly creates a flexural moat around it (Bodine et al. 1981). The only sediment present in the moat is 50–100 m of pelagic sediment blanketing the basement, forming the basal layer. The sediment influx lags in time compared to the subsidence rate, and the moat remains predominantly under-filled.
- B. **Stage 2:** As the moat begins to fill up with volcanic debris, the thin, layered lower landslide units begin to develop. Although there are evidences of slope failure in this stage (Normark et al. 1979; Malahoff 1987), the primary sediment source seems to be along-axis transport of mass wasting deposits from the older volcanoes of the volcanic chain. The newly formed volcano continues to grow and flexural subsidence exceeds the sedimentation rate, resulting in continued deepening of the moat.

- C. **Stage 3:** The moat enters this stage when the sediment flux from mass wasting exceeds the flexural subsidence from loading. Instability along unbuttressed flanks of volcanic islands, particularly along active rift zones trigger large scale mass wasting events that began to fill up the moat. These massive slumps and debris avalanches with poorly sorted volcanic rock form the bulk of the landslide unit.

Among episodic large scale mass wasting events, the moat continues to fill up, at a slower rate, by sediments from adjacent volcanoes or sediments transported along the axis of the moat. These sediments may back-tilt the pre-existing sediments and drown their sources, which leads to the formation of offlapping sequences.

- D. **Stage 4:** In the last stage of the moat development, flexural subsidence of the moat ceases, and flat-lying, horizontal reflectors of the ponded units develop. Their discordance with the underlying units indicates a period of depositional hiatus. This stage is characterized by a small amount of post-depositional subsidence and tilting.

It should be noted that because of episodic nature of both the mass wasting and volcanic growth, the deposition pattern does not represent a unidirectional growth sequence. Instead, the identified stratigraphic units are markers for changes in the balance between sediment input and flexural subsidence. However, over a long time, there is a general progression between the different growth stages as described earlier (Rees et al. 1993).

## References

- Anderson RN, Hobart MA (1976) The relation between heat flow, sediment thickness, and age in the eastern Pacific. *J Geophys Res* 81:2968–2989
- Anderson RN, Skilbeck JN (1981) Oceanic heat flow. In: Emiliani C (ed) *The Seas, 7, the oceanic lithosphere*. Wiley-Interscience, New York, pp 489–5231
- Anderson RN, Langseth MG, Sclater JG (1977) The mechanisms of heat transfer through the floor of the Indian Ocean. *J Geophys Res* 82:3391–3409
- Bargar KE, Jackson ED (1974) Calculated volumes of individual shield volcanoes along the Hawaiian-Emperor chain. *US Geol Surv J Res* 2:545–550
- Barone AM, Ryan WBF (1990) Single plume model for asynchronous formation of the Lamont Seamounts and adjacent East Pacific Rise terrains. *J Geophys Res* 95:10801–10827
- Batiza R, Vanko D (1983) Volcanic development of small oceanic central volcanoes on the flanks of the East Pacific Rise inferred from narrowbeam echo-sounder surveys. *Mar Geol* 54:53–90
- Batiza R, Vanko D (1984) Petrology of young Pacific seamounts. *J Geophys Res* 89:11235–11260
- Bodine JH, Steckler MS, Watts AB (1981) Observations of flexure and rheology of the oceanic lithosphere. *J Geophys Res* 86:3695–3707
- Bruce PM, Huppert HE (1990) Solidification and melting along dykes by the laminar flow of basaltic magma. In: Ryan MP (ed) *Magma transport and storage*. Wiley, New York, pp 87–101

- Calmant S, Francheteau J, Cazenave A (1990) Elastic layer thickening with age of the oceanic lithosphere: a tool for prediction of the age of volcanoes or oceanic crust. *Geophys J Int* 100:59–67
- Christiansen LB, Garven G (2004a) Transient hydrogeologic models for submarine flow in volcanic seamounts: 1. The Hawaiian Islands. *J Geophys Res* 109(B02108):18
- Christiansen LB, Garven G (2004b) Transient hydrogeologic models for submarine flow in volcanic seamounts: 2. Comparison of the Hawaiian, Canary and Marquesas Islands. *J Geophys Res* 109(B02109):18
- Clague DA, Reynolds JR, Davis AS (2000) Near-ridge seamount chains in the northeastern Pacific Ocean. *J Geophys Res* 105:16501–16561
- Crough ST (1978) Thermal origin of mid-plate hot-spot swells. *Geophys J Roy Astron Soc* 35:451–469
- Crough ST (1983) Hotspot swells. *Annu Rev Earth Planet Sci* 11:165–193
- Cullen AB, McBirney AR, Rogers RD (1987) Structural controls on the morphology of Galapagos shields. *J Volcanol Geotherm Res* 34:143–151
- Davies GF (1988) Ocean bathymetry and mantle convection: 1. Large scale flow and hotspots. *J Geophys Res* 93:10467–10480
- Davies GF (1992) Temporal variation of the Hawaiian plume flux. *Earth Planet Sci Lett* 113:277–286
- DeLaughter JE, Stein CA, Stein S (2005) Hotspots: A view from the swells. In: Foulger GR et al (eds) *Plates, plumes, and paradigms*. Boulder, Colorado, Geological Society of America Special Paper 388, pp 257–278
- DePaolo DJ, Bryce JG, Dodson A, Shuster D, Kennedy B (2001) Isotopic evolution of Mauna Loa and the chemical structure of the Hawaiian plume. *Geochem Geophys Geosyst* 2(7):32
- Escarlin J, Cannat M, Pouliquen G, Rabain A, Lin J (2001) Crustal thickness of V-shaped ridges south of the Azores: interaction of the Mid-Atlantic Ridge (36°–39°N) and the Azores hot spot. *J Geophys Res* 106:21719–21735
- Fehn U, Cathles LM (1986) The influence of plate movement on the evolution of hydrothermal convection cells in the oceanic crust. *Tectonophysics* 125:289–312
- Fehn U, Green KE, Von Herzen RP, Cathles LM (1983) Numerical models for the hydrothermal field at the Galapagos spreading center. *J Geophys Res* 88:1033–1048
- Fialko YA, Rubin AM (1999) What controls the along-strike slopes of volcanic rift zones? *J Geophys Res* 104:20007–20020
- Fiske RS, Jackson ED (1972) Orientation and growth of Hawaiian volcanic rifts: the effect of regional structure and gravitational stresses. *Proc R Soc London Ser A* 329:299–326
- Fornari DJ, Ryan WBF, Fox PJ (1984) The evolution of craters and calderas on young seamounts: insights from Sea MARC I and Sea Beam sonar survey of a small seamount group near the axis of the East Pacific Rise at ~10°N. *J Geophys Res* 89:11069–11083
- Fornari DJ, Batiza R, Allan JF (1987) Irregularly shaped seamounts near the East Pacific Rise: implications for seamount origin and rise axis processes. In: Keating BH, Fryer P, Batiza R, Boehlert GW (eds) *Seamounts, Islands and Atolls*. Geophysical monograph series 43, AGU, Washington, DC, pp 35–47
- Frey F, Garcia M, Roden M (1994) Geochemical characteristics of Koolau Volcano: implications of intershield geochemical differences among Hawaiian volcanoes. *Geochim Cosmochim Acta* 58:1441–1462
- Gordon RG, Jurdy DM (1986) Cenozoic global plate motions. *J Geophys Res* 91:12389–12406
- Hamilton EL (1957) Marine geology of the southern Hawaiian Ridge. *Geol Soc Am Bull* 68:1011–1026
- Harris RN, Garven G, Geogren J, McNutt MK, Christiansen L, Von Herzen RP (2000a) Submarine hydrogeology of the Hawaiian archipelagic apron 2. Numerical simulations of coupled heat transport and fluid flow. *J Geophys Res* 105:21371–21385
- Harris RN, Von Herzen RP, McNutt MK, Garven G, Jordahl K (2000b) Submarine hydrogeology of the Hawaiian archipelagic apron 1. Heatflow patterns north of Oahu and Maro Reef. *J Geophys Res* 105:21353–21369

- Head JW, Wilson L (1992) Magma reservoirs and neutral buoyancy zones on Venus: implications for the formation and evolution of volcanic landforms. *J Geophys Res* 97:3877–3903
- Hieronimus CF, Bercovici D (1999) Discrete alternating hotspot islands formed by interaction of magma transport and lithospheric flexure. *Nature* 397:604–607
- Hieronimus CF, Bercovici D (2001) A theoretical model of hotspot volcanism: control on volcanic spacing and patterns via magma dynamics and lithospheric stresses. *J Geophys Res* 106:683–702
- Holcomb RT, Moore JG, Lipman PW, Belderson RH (1988) Voluminous submarine lava flows from Hawaiian volcanoes. *Geology* 16:400–404
- Hollister CD, Glenn MF, Lonsdale PF (1978) Morphology of seamounts in the western Pacific and Philippine Basin from multi-beam sonar data. *Earth Planet Sci Lett* 41(4):405–418
- Ito GT (2001) Reykjanes “V”-shaped ridges originating from a pulsing and dehydrating mantle plume. *Nature* 411:681–684
- Jackson ED, Silver EA, Dalrymple GB (1972) Hawaiian-Emperor chain and its relation to Cenozoic circum-Pacific tectonics. *Geol Soc Am* 83:601
- Jacobson RS (1992) Impact of crustal evolution on changes of the seismic properties of the uppermost ocean crust. *Rev Geophys* 30:23–42
- Leslie SC, Moore GF, Morgan JK, Hills DJ (2002) Seismic stratigraphy of the Frontal Hawaiian Moat: implications for sedimentary processes at the leading edge of an oceanic hotspot trace. *Mar Geol* 184:143–162
- Lindwall DA (1988) A two-dimensional seismic investigation of crustal structure under the Hawaiian Islands near Oahu and Kauai. *J Geophys Res* 93:12107–12122
- Lister CRB (1972) On the thermal balance of a mid-ocean ridge. *Geophys J R Astron Soc* 26: 515–535
- Lister CRB (1982) “Active” and “passive” hydrothermal system in the oceanic crust: predicted physical conditions. In: Fanning KA, Manheim FT (eds) *The dynamic evolution of the ocean floor*. University of Miami, Coral Gables, pp 441–470
- Lister JR (1990) Buoyancy-driven fluid fracture: the effects of material toughness and low viscosity precursors. *J Fluid Mech* 210:263–280
- Lister JR, Dellar PJ (1996) Solidification of pressure-driven flow in a finite rigid channel with application to volcanic eruptions. *J Fluid Mech* 323:267–283
- Lister JR, Kerr RC (1991) Fluid-mechanical models of crack propagation and their application to magma transport in dykes. *J Geophys Res* 96:10049–10077
- Lonsdale P (1989) A geomorphological reconnaissance of the submarine part of the East Rift Zone of Kilauea Volcano, Hawaii. *Bull Volcanol* 51:123–144
- Malahuff A (1987) Geology of the summit of Loihi submarine volcano. *US Geol Surv Prof Pap* 1350:133–144
- McBirney AR, Williams H (1969) Geology and petrology of the Galapagos Islands. *Mem Geol Soc Am* 118
- McNutt MK (1984) Lithospheric flexure and thermal anomalies. *J Geophys Res* 89:11180–11194
- Menard HW (1964) *Marine Geology of the Pacific*. McGraw-Hill, New York
- Menard HW (1986) *Islands*. Scientific American Library Series, Oxford, WH Freeman and Co, New York, p 230
- Mitchell N (2001) Transition from circular to stellate forms of submarine volcanoes. *J Geophys Res* 106:1987–2003
- Molnar P, Stock J (1987) Relative motions of hotspots in the Pacific, Atlantic, and Indian Oceans since late Cretaceous time. *Nature* 327:587–591
- Moore JG, Clague DA, Holcomb RT, Lipman PW, Normark WR, Torresan ME (1989) Prodigious submarine landslides on the Hawaiian Ridge. *J Geophys Res* 94:17465–17484
- Moore JG, Normark WR, Holcomb RT (1994) Giant Hawaiian landslides. *Annu Rev Earth Planet Sci* 22:119–144
- Nercessian A, Hirn A, Lepine J-C, Sapin M (1996) Internal structure of Piton de la Fournaise volcano from seismic wave propagation and earthquake distribution. *J Volcanol Geotherm Res* 70:123–143

- Normark WR, Lipman RW, Moore JG (1979) Regional slump structures on the west flank of Mauna Loa volcano, Hawaii. Paper presented at Hawaii Symposium on Intraplate Volcanism and Submarine Volcanism, International Association of Volcanology and Chemistry of the Earth's interior, Hilo, Hawaii
- Olson P (1990) Hot spots, swells and mantle plumes. In: Ryan MP (ed) *Magma transport and storage*. Wiley, Hoboken, pp 33–51
- Olson P, Christensen U (1986) Solitary wave propagation in a fluid conduit within a viscous matrix. *J Geophys Res* 91:6367–6374
- Parsons B, Sclater JG (1977) An analysis of the variation of ocean floor bathymetry and heat flow with age. *J Geophys Res* 82(5):803–827
- Patterson PL, Lowell RP (1982) Numerical models of hydrothermal circulation for the intrusion zone at an ocean ridge axis. In: Fanning KA, Manheim FT (eds) *The dynamic evolution of the ocean floor*. University of Miami, Coral Gables, pp 471–492
- Phipps Morgan J, Morgan WJ, Price E (1995) Hotspot melting generates both hotspot volcanism and a hotspot swell? *J Geophys Res* 10:8045–8062
- Putirka K (1999) Melting depths and mantle heterogeneity beneath Hawaii and the East Pacific Rise: constraints from Na/Ti and rare Earth element ratios. *J Geophys Res* 104:2817–2829
- Rees BA, Detrick RS, Coakley BJ (1993) Seismic stratigraphy of the Hawaiian flexural moat. *GSA Bull* 105(2):189–205
- Regelous M, Hofmann AW, Abouchami W, Galer SJG (2003) Geochemistry of lavas from the Emperor Seamounts, and the geochemical evolution of Hawaiian magmatism from 85 to 42 Ma. *J Petrol* 44:113–140
- Ribe NM, Christensen UR (1994) Three-dimensional modeling of plume-lithosphere interaction. *J Geophys Res* 99:669–682
- Ryan MP (1987) Neutral buoyancy and the mechanical evolution of magmatic systems. In: Mysen BO (ed) *Magmatic processes: physicochemical principles*, Special publication Geochemical Society, vol 1, pp 259–287
- Sclater JG, Jaupart C, Galson D (1980) The heat flow through oceanic and continental crust and the heat loss of the Earth. *Rev Geophys* 18:269–311
- Scott DR, Stevenson DJ, Whitehead JA (1986) Observations of solitary waves in a viscously deformable pipe. *Nature* 319:759–761
- Simkin T (1972) Origin of some flat-topped volcanoes and guyots. *Mem Geol Soc Am* 132:183–193
- Sleep NH (1990) Hotspots and mantle plumes: some phenomenology. *J Geophys Res* 95:6715–6736
- Sleep NH (1992) Time dependence of mantle plumes: some simple theory. *J Geophys Res* 97:20007–20019
- Sleep NH, Wolery TJ (1978) Egress of hot water from the midocean ridge hydrothermal system: some thermal constraints. *J Geophys Res* 83:5913–5922
- Smith DK (1996) Comparison of the shapes and sizes of seafloor volcanoes on Earth and “pancake” domes on Venus. *J Volcanol Geotherm Res* 73:47–64
- Smith TL, Batiza R (1989) New field and laboratory evidence for the origin of hyaloclastite. *Bull Volcanol* 51:96–114
- Spence DA, Sharp PW, Turcotte DL (1987) Buoyancy-driven crack propagation: a mechanism for magma migration. *J Fluid Mech* 174:135–153
- Spinelli GA, Giambalvo ER, Fisher AT (2004) Sediment permeability, distribution, and influences on fluxes in oceanic basement. In: Davis EE, Elderfield EH (eds) *Hydrogeology of the oceanic lithosphere*. Cambridge University Press, Cambridge, pp 151–188
- Stein CA, Stein S (1992) A model for the global variation in oceanic depth and heat flow with lithospheric age. *Nature* 359:123–129
- Stein CA, Stein S (1993) Constraints on Pacific midplate swells from global depth-age and heatflow-age models. In: Pringle M, et al (eds) *The Mesozoic Pacific*. American Geophysical Union Geophysical Monograph 77, Washington, DC, pp 53–76

- Stein CA, Stein S (1994) Constraints on hydrothermal heat flux through the oceanic lithosphere from global heatflow. *J Geophys Res* 99:3081–3095
- Stein CA, Von Herzen RP (2007) Potential effects of hydrothermal circulation and magmatism on heatflow at hotspot swells. In: Foulger GR, Jurdy DM (eds) *Plates, plumes, and planetary processes*. Geological Society of America Special Paper 430, pp 261–274
- Steinberger B (2000) Plumes in a convecting mantle: models and observations for individual hotspots. *J Geophys Res Solid Earth* 105(B5):11127–11152
- Steinberger B, O’Connell RJ (1998) Advection of plumes in mantle flow: implications for hot spot motion, mantle viscosity and plume distribution. *Geophys J Int* 132:412–434
- Tarduno JA et al (2003) The emperor seamounts: southward motion of the Hawaiian hotspot plume in Earth’s mantle. *Science* 301:1064–1069
- ten Brink U (1991) Volcano spacing and plate rigidity. *Geology* 9:397–400
- ten Brink US, Brocher TM (1987) Multichannel seismic evidence for a sub-crustal intrusive complex under Oahu and a model for Hawaiian volcanism. *J Geophys Res* 92:13687–13707
- ten Brink US, Watts AB (1985) Seismic stratigraphy of the flexural moat flanking the Hawaiian Islands. *Nature* 317:421–424
- Turcotte DL (1981) Some thermal problems associated with magma migration. *J Volcanol Geotherm Res* 10:267–278
- Turcotte DL (1982) Magma migration. *Annu Rev Earth Planet Sci* 10:397–408
- Van Ark E, Lin J (2004) Time variation in igneous volume flux of the Hawaii-emperor hot spot seamount chain. *J Geophys Res Solid Earth* 109(B11)
- Varnes DJ (1978) Slope movement types and processes. In: Schuster RL, Krizek RJ (eds) *Landslides, analysis and control*. Special report 176, National Academy of Sciences, Washington, DC, pp 11–33
- Vidal V, Bonneville A (2004) Variations of the Hawaiian hot spot activity revealed by variations in the magma production rate. *J Geophys Res* 109(B03104)
- Vogt PR (1974) Volcano spacing, fractures and thickness of the lithosphere. *Earth Planet Sci Lett* 21:235–252
- Vogt PR, Smoot NC (1984) The Geisha guyots: multibeam bathymetry and morphometric interpretation. *J Geophys Res* 89(B13):11085–11107
- Von Herzen RP (2004) Geothermal evidence for continuing hydrothermal circulation in older (60 m.y.) ocean crust. In: Davis EE, Elderfield EH (eds) *Hydrogeology of the oceanic lithosphere*. Cambridge University Press, Cambridge, pp 414–447
- Von Herzen RP, Cordery MJ, Detrick RS, Fang C (1989) Heatflow and the thermal origin of hotspot swells: the Hawaiian Swell revisited. *J Geophys Res* 94:13783–13799
- Walker GPL (1984) Downsag calderas, ring faults, caldera sizes, and incremental caldera growth. *J Geophys Res* 89:8407–8416
- Walker GPL (1989) Gravitational (density) controls on volcanism, magma chambers and intrusions. *Aust J Earth Sci* 36:149–165
- Watts AB (1978) An analysis of isostasy in the world’s oceans: 1. Hawaiian-Emperor seamount chain. *J Geophys Res* 83:5989–6004
- Watts AB (2001) *Isostasy and flexure of the lithosphere*. Cambridge University Press, New York, p 458
- Watts AB, ten Brink US (1989) Crustal structure, flexure and subsidence history of the Hawaiian Islands. *J Geophys Res* 94:10473–10500
- Watts AB, ten Brink US, Buhl P, Brocher TM (1985) A multichannel seismic study of lithospheric flexure across the Hawaiian-emperor seamount chain. *Nature* 315:105–111
- Watts AB, Peirce C, Collier J, Dalwood R, Canales JP, Henstock TJ (1997) A seismic study of lithospheric flexure in the vicinity of Tenerife, Canary Islands. *Earth Planet Sci Lett* 146: 431–447
- Weertman J (1971) Theory of water-filled crevasses in glaciers applied to vertical magma transport beneath oceanic ridges. *J Geophys Res* 76:1171–1183
- White RS (1993) Melt production rates in mantle plumes. *Philos Trans Phys Sci Eng* 342:137–153

- Whitehead JA (1987) A laboratory demonstration of solitons using a vertical watery conduit in syrup. *Am J Phys* 55:998–1003
- Williams DL, Von Herzen RP, Sclater JG, Anderson RN (1974) The Galapagos spreading centre: lithospheric cooling and hydrothermal circulation. *Geophys J R Astron Soc* 38:587–608
- Winterer EL (1989) Sediment thickness map of the Northeast Pacific. In: Winterer EL, Hussong DM, Decker RW (eds) *The geology of north America, vol N. The eastern Pacific Ocean and Hawaii, decade of North American geology*, Geol Soc Am, pp 307–310
- Wolery TJ, Sleep NH (1976) Hydrothermal circulation and geochemical flux at mid-ocean ridges. *J Geol* 84:249–275
- Wyss M (1980) Hawaiian rifts and recent Icelandic volcanism: expressions of plume generated radial stress fields. *J Geophys* 19:19–22

# Chapter 7

## The Great Plume Debate

### 7.1 Brief History

The plume hypothesis (Morgan 1971, 1972a, b) has been developed during the 1970s to explain several intraplate volcanic provinces on the earth's surface, apparently not explained by plate tectonics (Fig. 7.1).<sup>1</sup> It postulates a form of thermal convection with narrow upwellings and diffuse, broad downwellings, as an alternative to giant convection cells of Holme's (1944), centered beneath spreading ridges (Hess 1962). The drive for the hypothesis comes from the (apparent) fixity of volcanic island relative to each other, and near-parallelism of island chains in the Pacific Ocean. The hypothesis is based on active mantle upwellings, high temperature and fluid dynamics, and predictions based on the hypothesis include following mechanisms (Morgan 1971, 1972a, b):

1. plumes bring up a large fraction of the earth's heat and magma,
2. plates moving over the plumes have narrow chains of time progressive volcanoes, and
3. plumes are responsible for break-up and drifting of the plates.

The term "hotspot", originally coined by Wilson (1963) to explain within-plate volcanic islands supposed to be due to melting anomalies, have been put forward as effect of mantle plumes impinging below the lithosphere. Various evidences such as fixed position of volcanic islands with respect to the mantle, parallelism of island chains, regular time-progressive volcanism, high rate of volcanism, magma temperature, hotspot heatflow, plate driving mechanism, uplift of large igneous provinces, chondritic Nd-isotope ratios, high <sup>3</sup>He content of magmas and mantle tomography, have been gathered to support the mantle plume hypothesis at one time or the other (Anderson and Natland 2005). Injection experiments in the early 90s made by Campbell and Griffiths (1990, 1993) revived the hypothesis, leading to

---

<sup>1</sup>The pictures in this chapter are intended to bring some humor into this academic conundrum, and are not to be taken seriously.

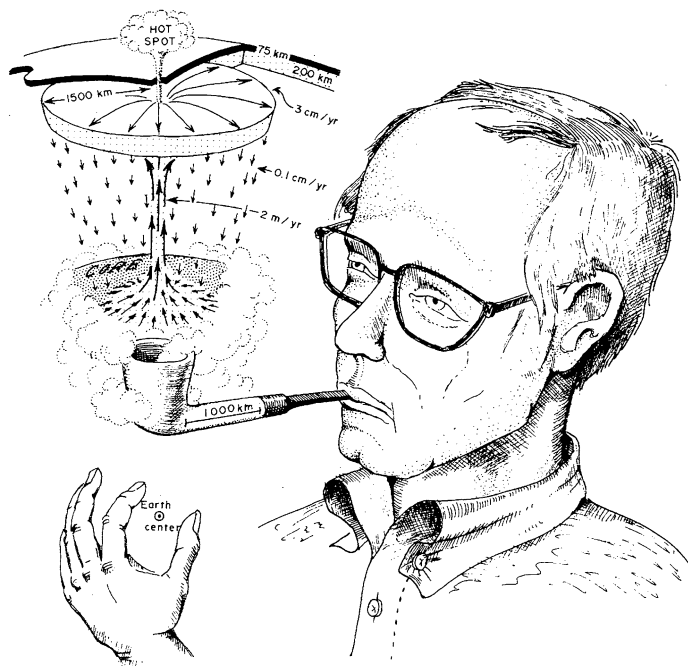


**Fig. 7.1** Conception of the mantle plume hypothesis (Holden and Vogt 1977)

a differentiation between the plume head and the tail. Their experiments point towards the association of a hotspot track (tail) with a large igneous province (head) and precursory crustal uplift. The current views on plumes are somewhat different from that of Morgan (1971, 1972a, b) and Wilson (1963). All the “proofs” have been challenged, and none of them holds as definitive evidences for plumes. Some have been abandoned altogether, while a combination of some of the remaining ones are used to validate the existence and type of plume (Courtillot et al. 2003), though not necessarily a consistent set. The hypothesis is currently under unusual controversy and discussion, and various alternative ideas have been presented to explain the different features considered as confirmation of mantle plumes (see Anderson and Natland 2005, for a quick review).

## 7.2 Problems/Critiques

**Fluid dynamics**—Tozer (1973) and Richter and Parsons (1975) has challenged the fluid dynamic basis of the mantle plume hypothesis. Tozer (1973) pointed out that the Reynolds number of the mantle ( $\sim 10^{-20}$ ) precludes the application of usual fluid dynamic definition of a plume with a bulbous head and a narrow tail. Thermal

boundary layers in the mantle can be thin (Peclet number  $\sim 10^3$ ), while mechanical boundary layers (viscosity/velocity anomaly) are necessarily thick because of low viscosity to thermal diffusivity ratio (Prandtl number,  $\sim 10^{24}$ ; square root of which gives the ratio of thickness of the viscous and thermal boundary layers) and thickness of the mantle. The narrow thermal boundary layers in the mantle are not accompanied by narrow flows. Under the mantle conditions, a thermal plume is more akin to a convective flow with the dimensions dependent on system dimensions, so that the plume flows have dimensions of the entire lower mantle, and not that of a thin thermal boundary layer and a large velocity gradient within a narrow radius is implausible. Such features are termed as superplumes or megaplumes (e.g., Courtillot et al. 2003) in the current literature, but they are far from the concept of the original plume hypothesis.

Injection experiments of Campbell and Griffiths (1990, 1993) and Cordery et al. (1997) revived the plume hypothesis by simulating a plume shape with a bulbous head and a narrow tail by injecting hot fluids into stationary cold fluid. The new predictions require a spatio-temporal association of a flood basalt province in the initial parts of a hotspot track. The most common objections against these experiments are that they are artificial in the sense that plumes are not generated as a result of convective instability in the lower mantle, but, instead, assumed to be due to localized heating. The simulations do not incorporate phase change, pressure effects (Larsen and Yuen 1997) or internal heating. Tackley (1998) had pointed out that fluids that are internally heated or are in a pressure gradient, do not spontaneously develop narrow upwellings. On the contrary, the narrow plumes can only generate in absence of a pressure gradient in the mantle. Also, the experiments did not address the issues of mantle fluid dynamics and scaling of mantle conditions. Successful generation of a thermal plume would require instabilities at the base of the mantle that are orders of magnitudes larger and move more slowly than plates in the upper mantle (Anderson 1987, 1989). Predictions based on the experiments fail to explain the absence of flood basalt provinces in the case of Hawaii, Marquesas and other volcanic chains, the absence of plume tail eruption following several oceanic plateaus like the Ontong-Java Plateau, and a significant fluctuation in eruption volume in island chains like Hawaii. However, thermochemical plumes of Fartenani and Samuel (2005) may provide an alternative explanation to some of these observations.

High velocity mantle anomalies—High velocity seismic anomaly lying in the lowermost mantle near Hawaii has been cited as evidence for the presence of plume (Kanasewich et al. 1972, 1973; Kanasewich and Gutowski 1975), further corroborated by a recent study (Nataf 2000). Wright (1975) argues that the high velocities are not compatible with other observations on plumes (how can a molten blob produce high velocity is not clear) and it is open to other interpretations. Best et al. (1974) showed in a seismic experiment that the seismic velocity beneath Hawaii is not anomalous, ruling out a large, hot, partially molten region below Hawaii. Studies of upper and middle mantle shear-wave propagation efficiency (Sipkin and Jordan 1975) and velocity (Katzman et al. 1998) below Hawaii show both to be higher than the average for south-western Pacific, which points strongly against the

extensive melting below Hawaii. Similar difficulties were also cited by Montelli et al. (2004), using finite-frequency compressional wave seismology. According to them, the difficulties for assigning a definite mantle anomaly to a surface hotspot arise from a lack of coverage and seismic resolution.

Mantle tomography—Tomographic data is often presented as providing evidences for the presence of low velocity, anomalous melting zones in the mantle below major hotspots. Because of the resolution and lack of coverage, the evidence presented is based on interpretation (hence, subjective). However, ponding and spreading of rising mantle plumes below mid-mantle phase boundaries (e.g., 650 km discontinuity) should be easy to image, yet both features are generally lacking where they are expected (Anderson et al. 1992; Woods and Okal 1996). Because of the presence of a large number of surface hotspots, even a random distribution of mantle tomographic anomalies would place at least six hotspots within 300 km of a vertical region of low velocity, giving rise to false positives. Statistical analysis of such arbitrary juxtaposition is required to sort out the random events from the actual causal anomalies. Also, the low-velocity zones may not necessarily be hot, but just partially molten or CO<sub>2</sub> rich (Seth 2003). Tomographic studies also reveal narrow slices of the lithosphere returning to the mantle at subduction zones, and broad upwellings beneath hotspots (Ritesma and van Heijst 2000; Ritesma and Allen 2003), which is contradictory to what is envisaged as a plume.

Heat flow and temperature—The plumes are assumed to bring a large fraction of the core heat to the surface (Morgan 1971, 1972a, b), which remains unconfirmed. The present understanding is that plumes account for a small fraction of the surface heat flow (e.g., Malamud and Turcotte 1999). Another defining characteristic of a thermal plume is high temperature, which is seldom used directly as evidence. It is rather the rate or volume of magmatism, which is used as a proxy. Magma from a mid-mantle depth is expected to reach the surface with a temperature difference of ~400 °C (Mckenzie and Bickle 1988), while it would be about 800 °C for a lower mantle source (Albers and Christensen 1996). This is difficult to establish, as most inferred magma temperatures fall in the range of 1400–1500 °C (still lower value of 1100–1400 °C in Presnall and Gudfinnsson 2005), with an excess temperature of 170–270 °C (Herzberg and O'Hara 2002), equivalent to derivation from upper mantle or depths above 150 km. Examples of “hotspot” temperature shows that they are much colder than thought, having temperature excess of 57, 51 and <70 °C for the Azores, Galapagos and Iceland (Ribe et al. 1995; Feighner et al. 1995), respectively. Ito and Lin (1995) derives a temperature excess of 50–150 °C for Iceland, Azores, Tristan and Easter Islands, while the Galapagos basalts are of lower temperature than that along the nearby ridge segment (Fisk et al. 1982). Thus, hotspots are not really that “hot” and high mantle temperatures also do not seem to be a universal characteristic of hotspots (e.g., Von Herzen et al. 1989; Yaxley 2000; Anderson 2001; Foulger et al. 2005; Presnall and Gudfinnsson 2005).

Mantle temperature—The plume hypothesis is based on an isothermal, sub-solidus, dry and homogeneous upper mantle, disregarding effects of small scale convection and 3D focusing. McKenzie and Bickle (1988) had assumed a “cold”,

mantle temperature of  $1280 \pm 20$  °C, and temperature excess of 150–200 °C is ascribed to localized hot jets (plumes). Present geophysical estimates of the upper mantle temperature are more than 100 °C hotter than this, and the variability is more than an order greater than that adopted by McKenzie and Bickle (1988) (e.g., Anderson and Bass 1984; Anderson 1989; Kaula 1983; Hofmeister 1999). The temperature variation along the mid-oceanic ridges, based on petrology and crustal thickness, gives a value of  $\pm 200$  °C (Klein and Langmuir 1987; Bonatti 1990; Kane and Hayes 1994). The lateral variation in upper mantle temperature below plates ranges between  $\pm 150$ ° and 200 °C (Elder 1976; Anderson 1998a; Lowman and Jarvis 1999), arising from normal convection and plate tectonic processes, even after removing “hotspot” and subduction zone influences. Absolute temperatures in the upper mantle, estimated from mineral physics, seismology, geodynamics, heat flow and petrology are consistent, giving a mean potential temperature of 1400 °C, with an uncertainty of  $\pm 50$  °C (Kaula 1983; Anderson and Bass 1984; Anderson 1989; Duffy and Anderson 1989), with the mean being 100 °C hotter than that assumed by plume theorists. Small-scale convections arising in the upper mantle due to plate tectonic processes like edge-driven convection, slab cooling, cratonic roots, continental insulation and shearing due to plate movement amounts to  $\pm 200$  °C variations (the temperature of upper mantle is thus  $1400 \pm 200$  °C), and can give rise to concentrated, shallow, plume-like upwelling due to 3D focusing (Richter 1973; Parmentier and Morgan 1990; Shen and Forsyth 1992; Anderson 1998b, 2000).

Basalt geochemistry—A consequence of the injection experiments of Campbell and Griffiths (1990, 1993) is the prediction that high MgO picritic lavas should dominate the early melting products of plume heads in the center of a flood basalt province, and becomes less abundant towards the periphery. These features are rarely observed, especially near the center, which may be because they are covered by later flow or never erupted due to high density (Stolper and Walker 1980). Documented cases include the Parana-Etendeka, Deccan (but see Seth 1999), Emeishan, North Atlantic, Siberian Traps and Karoo flood basalts (Campbell and Davies 2006). Geochemists attributed the unusual chemistry of elevated regions of the Mid-Atlantic ridge, with radiogenic isotopes of Sr, Nd, Hf and Pb, and incompatible trace elements, to be derived from the primordial mantle by plumes (e.g., Schilling 1973a, b) (Fig. 7.2). The concept is based on an assumed homogeneity of the mantle composition. However, this observation has been seriously questioned, and it has been pointed out that picritic magma may themselves be melting products of mid-ocean ridge basalt at appreciable depths, under  $>25$  kbar pressure (Anderson et al. 1992; Anderson 1994a, b). Under these conditions, Mg-rich olivine is the first phase to get consumed, producing picritic melts enriched in incompatible elements (Arndt et al. 1993). Similarly, extensive decompression melting of mantle asthenosphere during lithospheric rifting would also produce shallow-level melts of picritic composition, but in this case, not enriched with incompatible elements (Arndt et al. 1993). The enriched incompatible elements can also be accounted for by involvement of components derived from sediments and altered oceanic crust by subduction (e.g., Zindler and Hart 1986; Weaver 1991;

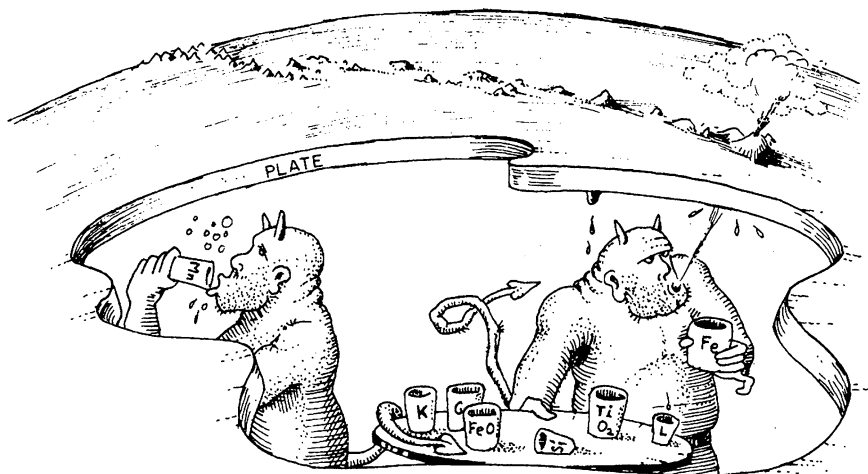


**Fig. 7.2** Strange geochemistry of ocean island tholeiites, hawaiites, balonites and similar hotspot generated rocks attributed to the culinary habits of demons in the mantle (Holden and Vogt 1977)

Hofmann 1997), producing a “fertile” region in the mantle, which is later sampled by mid-ocean ridges.

**Helium isotopic ratio**—High  $^3\text{He}/^4\text{He}$  ratio is taken as a certain proof of plumes being derived from mantle by most geochemists (e.g., Craig and Lupton 1976, 1981; Farley and Nerona 1998; Graham 2000).  $^3\text{He}$  is definitely a primordial isotope, being derived during the Big Bang, but its enrichment process in the mantle and the location of the mantle  $^3\text{He}$  reservoir is unclear. The type hotspot examples of Hawaii, Yellowstone and Iceland have high  $^3\text{He}/^4\text{He}$  ratio, but not high  $^3\text{He}$  content, while a number of high  $^3\text{He}$  hotspots may not be of plume origin (e.g., Courtillot et al. 2003). The high  $^3\text{He}/^4\text{He}$  ratio can result from enrichment of low  $^4\text{He}$  or low U/He ratio, rather than high  $^3\text{He}$ . Such a process can occur during remelting of olivine cumulates, as olivine traps  $^3\text{He}$  isotopes, but does not have U-Th to produce  $^4\text{He}$  isotopes (Seth 2003). The ratio is thus not a definite tracer for a lower mantle source.

**Mantle homogeneity**—Homogeneity of the mantle composition is inherent in the plume hypothesis. However, geochemical indications suggest that it may not be the case. Different authors have suggested a homogeneous lherzolite upper mantle composition (Klein and Langmuir 1987; Langmuir et al. 1992; Plank and Langmuir 1992). Considering such a composition, Hirschmann et al. (1999) showed that increasing the partial melt fraction can generate decreased  $\text{Na}_2\text{O}$  and increased  $\text{CaO}/\text{Al}_2\text{O}_3$  in the melt, in contrast to the inferences of Klein and Langmuir (1987). Presnall et al. (2002) and Presnall and Gudfinnsson (2005) had pointed out that inclusion of  $\text{CO}_2$  lowers the basalt solidus, and melt productivity can increase from 0 to 24 % over a small range of temperature (1240–1260 °C). All these affect the composition of mid-ocean ridge basalts, and the global variations in FeO,  $\text{Na}_2\text{O}$  and

$\text{CaO}/\text{Al}_2\text{O}_3$  can be explained by various degrees of partial melting of a typical spinel lherzolite (pyrolite, most aluminous lherzolite from Ronda) in the mantle, without the presence of a plume.

Involvement of other lithologies like pyroxenite, garnet pyroxenite or eclogite in the mantle (Hirschmann and Stolper 1996; Salters and Dick 2002; Pertermann and Hirschmann 2003a, b) may explain enriched isotopes in the melt, and explains certain “hotspot” geochemistry. Mantle heterogeneity, produced by recycling of lithospheric plates, has been put forward to explain the various geochemical signatures from different hotspots. Subducting lithospheric plates reach various depths depending on their age, with only the oldest and thickest plates penetrating and stalling at the 650 km discontinuity (Rowley 2002; Meibom and Anderson 2004). Inclusion of  $\text{CO}_2$  and water from the downgoing slabs lowers the melting temperature, compared to that of dry peridotite, and produces regions of fertile blobs within the mantle, which may later get reheated and melted at mid-oceanic ridges, producing characteristic “hotspot” magmas enriched in incompatible elements. Such a process has been suggested for the derivation of primitive magma type beneath both Hawaii and Iceland by melting of whole sections of oceanic crust (Hofmann and Jochum 1996; Lassiter and Hauri 1998; Chauvel and Hémond 2000).

Domal uplifts—The arrival of a hot plume head to the upper mantle is expected to produce a domal uplift of 1000–1500 m at the surface, the best demonstrated case being the Emeishan flood basalt province in China (He et al. 2003). Non-plumists argue that this is not a universal occurrence, and the present day Hawaiian Swell, once attributed to high temperature and lithospheric rejuvenation, is currently thought to be due to underplating or addition of buoyant residue by reheated slabs (Presnall and Helsley 1982; Morgan 1997). The Siberian Traps and the Ontong-Java plateau are also put forward as cases where clear-cut domal uplift is not observed. However, it should be noted that the Siberian Traps overlie an unconformity, which would require certain amount of uplift. The observed uplift may differ from the predicted due to sediment cover in western Siberia (Saunders et al. 2007). The uplift in Ontong-Java plateau may remain unobserved because there is no associated erosion, as it took place under deep marine conditions. However an ash bed has been documented in ODP sites 167 and 463, indicating uplift and subaerial volcanic eruptions. Additionally, D’Acremont et al. (2003) and Burov and Guillou-Frottier (2005) had shown that if the rheology of the lithosphere is taken into account, the uplift patterns over plumes can be complex and not simply domal as expected.

Fixed position of hotspots—The lower mantle is believed to have a convective velocity ten times slower than the upper mantle (due to higher viscosity), which pins the location of the ascending plumes with respect to the mantle. Their positions are relatively stationary with respect to plate movement, and the path traced by the hotspots follows the plate motion direction with unidirectional age progression. This is in disagreement with the original concept of Morgan (1971, 1972a, b), but accepted within the current plume community as intrinsic to the character of plumes.

Semantic issues—The long history of plume and hotspot literature has developed a rich and confusing vocabulary, arising from the difficulty in defining a plume. The concept of a “hotspot” as a zone of anomalous intra-plate volcanism Wilson (1963) has been confused, and, in many studies, is used interchangeably with a “plume”. In mantle geochemistry literature, the term plume is used instead of hotspot to describe surface features such as Iceland (e.g. Iceland plume, Yellowstone plume), assuming a firm establishment of the cause-effect relationship. A plume is a hypothetical mantle feature which cannot be observed directly, while a hotspot is an actual region of significant volcanism. In the plume hypothesis, a hotspot is the surface manifestation of a plume, which can also be applied to mantle tomographic anomalies without any surface expression (Nataf 2000; Courtillot et al. 2003; Montelli et al. 2004). The vagueness of the concept is shown by the increase in the number of hotspots from the original 20, as defined by Wilson (1963) and Morgan (1971), to 117 (Burke and Wilson 1976), with recent lists containing ~50 hotspots (e.g., Courtillot et al. 2003), without any consistency between different authors. Another source of confusion arises from the proliferation of terms used to describe hotspots, such as midplate volcanism, intraplate volcanism, melting anomaly etc. Some hotspots are labeled as “coldspots”, “wetspots”, “hotlines”, “crackspots”, “fertile spots” etc. by various authors. Other associated terms include using plume heads for flood basalt provinces and oceanic plateaus (e.g., Ontong-Java plume head), and enriched components in magmas as plume components.

The term “plume” itself is not very well defined, and its defining characteristics seem to be any characteristics displayed by regions empirically defined as due to plume activity, such as Iceland, Hawaii, etc. and not the other way round. Any density-driven upwelling is termed as a plume in fluid dynamics, but not in geology. Low-density layers producing upwelling in the crust are termed as “diapirs” or “domes” (as in salt domes, but see Ramberg 1981). Upper mantle instabilities are technically plumes, but uncomfortable to most geologists. Most of the geological studies consider plumes rising from the hot lower mantle only.

### 7.3 Plate Tectonic Considerations

Many of the data used to support the plume hypothesis are debatable and subject to multiple interpretations (Fig. 7.3). Early ideas of crack propagation, membrane tectonics, self-perpetuating volcanic chains, gravitational anchors, dyke propagation, resurfacing slabs etc. have all provided partial explanations for the Hawaii-Emperor chain volcanoes (e.g., Shaw and Jackson 1973; Turcotte and Oxburgh 1973; Jackson and Shaw 1975; Jackson et al. 1975; Shaw et al. 1980; Presnall and Helsley 1982; Clague and Dalrymple 1987; Hieronymus and Bercovici 1999). These are currently disfavored as not being of holistic applicability, and being unable to explain features such as relative fixity of volcanic islands, midplate volcanism, large and variable magma volume etc. The problems arise from the

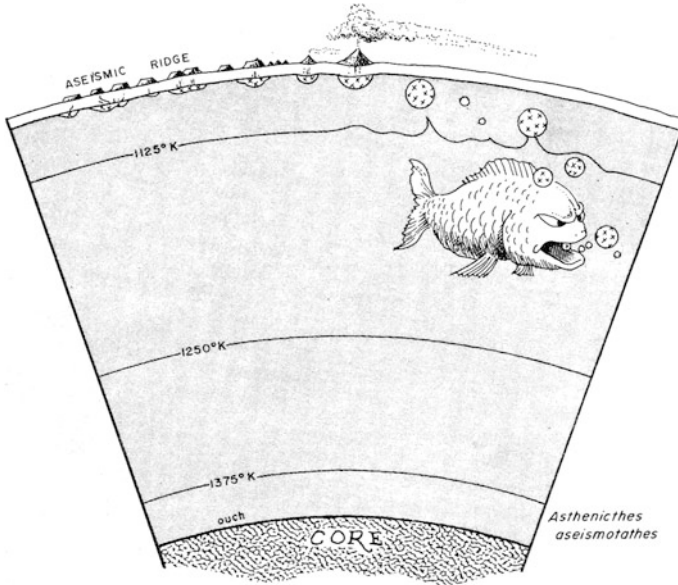


**Fig. 7.3** Alternative to the mantle plume hypothesis, based on ancient Japanese legend (Holden and Vogt 1977)

assumptions in the plate tectonic theory used in these models, such as an isothermal homogeneous mantle of fixed melting point and plate rigidity. A more generalized theory of plate tectonics, involving recycling, incipient and reactivated plate boundaries, and ephemeral plates combines and presents a single theory explaining plate tectonics, large igneous provinces and linear volcanic chains, without the involvement of mantle plumes (Anderson 2002a, b, c, 2005; Natland and Winterer 2005).

## References

- Albers M, Christensen U (1996) The excess temperature of plumes rising from the core-mantle boundary. *Geophys Res Lett* 23:3567–3570
- Anderson DL (1987) A seismic equation of state II: Shear properties and thermodynamics of the lower mantle. *Phys Earth Planet Inter* 45:307–323
- Anderson DL (1989) *Theory of the earth*. Blackwell Scientific Publications, Boston, p 366
- Anderson DL (1994a) The sublithospheric mantle as the source of continental flood basalts: the case against the continental lithosphere and plume head reservoirs. *Earth Planet Sci Lett* 123:269–280
- Anderson DL (1994b) Komatiites and picrites: evidence that the ‘plume’ source is depleted. *Earth Planet Sci Lett* 128:303–311
- Anderson DL (1998a) The scales of mantle convection. *Tectonophysics* 284:1–17

- Anderson DL (1998b) The EDGES of the mantle. In: Gurnis M, Wysession ME, Knittle E, Buffett B (eds) *The core-mantle boundary region*. American Geophysical Union, Washington, DC, pp 255–271
- Anderson DL (2000) The thermal state of the upper mantle; no role for mantle plumes. *Geophys Res Lett* 27(22):3623–3626
- Anderson DL (2001) Top-down tectonics. *Science* 293:2016–2018
- Anderson DL (2002a) How many plates? *Geology* 30:411–414
- Anderson DL (2002b) Occam's razor: simplicity, complexity, and global geodynamics. *Proc Am Philos Soc* 146(1):56–76
- Anderson DL (2002c) Plate tectonics as a far-from-equilibrium self-organized system. In: Stein S, Freymueller JT (eds) *Plate boundary zones*. Geophysical monograph, geodynamics series 30. American Geophysical Union, Washington, DC, pp 411–442
- Anderson DL, Bass JD (1984) Mineralogy and composition of the upper mantle. *Geophys Res Lett* 11:637–640
- Anderson DL, Natland JH (2005) A brief history of the plume hypothesis and its competitors: Concept and controversy. In: Foulger GR, Natland JH, Presnall DC, Anderson DL (eds) *Plates, plumes, and paradigms*. Geological Society of America Special Paper 388, pp 119–145
- Anderson DL, Tanimoto T, Zhang YS (1992) Plate tectonics and hotspots: the third dimension. *Science* 256:1645–1651
- Arndt NT, Czamanske GK, Wooden JL, Fedorenko VA (1993) Mantle and crustal contributions to continental flood volcanism. *Tectonophysics* 223:39–52
- Best WJ, Johnson LR, McEvilly TV (1974) ScS and the mantle beneath Hawaii. *Eos Trans Am Geophys Union (Fall Meeting Supplement)* 55:1147
- Bonatti E (1990) Not so hot “hot spots” in the oceanic mantle. *Science* 250(4977):107–111
- Burke KC, Wilson JT (1976) Hot spots on the Earth's surface. *J Geophys Res* 93:7690–7708
- Burov E, Guillou-Frotier L (2005) The plume head-continental lithosphere interaction using a tectonically realistic formulation for the lithosphere. *Geophys J Int* 161:469–490
- Campbell IH, Davies GF (2006) Do mantle plumes exist? *Episodes* 29(3):162–168
- Campbell IH, Griffiths RW (1990) Implications of mantle plume structure for the evolution of flood basalts. *Earth Planet Sci Lett* 99:79–93
- Campbell IH, Griffiths RW (1993) The evolution of the mantle's chemical structure. *Lithos* 30:389–399
- Chauvel C, Hémond C (2000) Melting of a complete section of recycled oceanic crust: trace element and Pb isotopic evidence from Iceland. *Geochem Geophys Geosyst* 1(2):1001
- Clague DA, Dalrymple GB (1987) The Hawaiian-emperor volcanic chain: Part I, Geologic evolution. In: Decker RW, et al (eds) *Volcanism in Hawaii*. United States Geological Survey Professional Paper 1350, Reston, Virginia, pp 5–54
- Cordery MJ, Davies GF, Campbell IH (1997) Genesis of flood basalts from eclogite-bearing mantle plumes. *J Geophys Res* 102:20179–20197
- Courtillot V, Davaille A, Besse J, Stock JM (2003) Three distinct type of hotspots in the Earth's mantle. *Earth Planet Sci Lett* 205:295–308
- Craig H, Lupton J (1976) Primordial Ne, He and H in oceanic basalts. *Earth Planet Sci Lett* 31:369–385
- Craig H, Lupton J (1981) Helium-3 and mantle volatiles in the ocean and the oceanic crust. In: Emiliani C (ed) *The sea*, 7. Wiley, New York, pp 391–428
- D'Acromont E, Leroy S, Burov EB (2003) Numerical modeling of a mantle plume: the plume head-lithosphere interaction in the formation of an oceanic large igneous province. *Earth Planet Sci Lett* 206:379–396
- Duffy TS, Anderson DL (1989) Seismic velocities in mantle minerals and the mineralogy of the upper mantle. *J Geophys Res* 94:1895–1912
- Elder J (1976) *The bowels of the earth*. Oxford University Press, London, p 222
- Farley KA, Neroni E (1998) Noble gases in the Earth's mantle. *Annu Rev Earth Planet Sci* 26:189–218

- Farnetani CG, Samuel H (2005) Beyond the thermal plume paradigm. *Geophys Res Lett* 32 (L07311):4
- Feighner M, Kellogg L, Travis B (1995) Numerical modeling of chemically buoyant mantle plumes at spreading ridges. *Geophys Res Lett* 22:715–718
- Fisk MR, Bence AE, Schilling JG (1982) Major element chemistry of Galapagos rift zone magmas and their phenocrysts. *Earth Planet Sci Lett* 61(1):171–189
- Foulger GR, Natland JH, Anderson DL (2005) Genesis of the Iceland melt anomaly by plate tectonic processes. In: Foulger GR, Natland JH, Presnall DC, Anderson DL (eds) *Plates, plumes, and paradigms*. Geological Society of America Special Paper 388, pp 595–625
- Graham DW (2000) Noble gas isotope geochemistry of mid-ocean ridge and ocean island basalts: Characterization of mantle source reservoirs. In: Porcelli D, et al (eds) *Noble gases in geochemistry and cosmochemistry*. *Rev Mineral Geochem* 47:247–317
- He B, Xu Y-G, Chung S-L, Xiao L, Wang Y (2003) Sedimentary evidence for a rapid crustal doming prior to the eruption of the Emeishan flood basalts. *Earth Planet Sci Lett* 213:389–403
- Herzberg C, O'Hara MJ (2002) Plume-associated ultramafic magmas of Phanerozoic age. *J Petrol* 43:1857–1883
- Hess HH (1962) A history of ocean basins. In: Engel AEJ et al (eds) *Petrologic studies: a volume in honor of A.F. Buddington*. Geological Society of America, Boulder, Colorado, pp 599–620
- Hieronimus CF, Bercovici D (1999) Discrete alternating hotspot islands formed by interaction of magma transport and lithospheric flexure. *Nature* 397:604–607
- Hirschmann MM, Stolper EM (1996) A possible role for garnet pyroxenite in the origin of the “garnet signature” in MORB. *Contrib Miner Petrol* 124:185–208
- Hirschmann MM, Ghiorso MS, Stolper EM (1999) Calculation of peridotite partial melting from thermodynamic models of minerals and melts, II: isobaric variations in melts near the solidus and owing to variable source composition. *J Petrol* 40:297–313
- Hofmann AW (1997) Mantle geochemistry: the message from oceanic volcanism. *Nature* 385:219–229
- Hofmann AW, Jochum KP (1996) Source characteristics derived from very incompatible trace elements in Mauna Loa and Mauna Kea basalts, Hawaii Scientific Drilling Project. *J Geophys Res* 101:11831–11839
- Hofmeister AM (1999) Mantle values of thermal conductivity and the geotherm from phonon lifetimes. *Science* 283(5408):1699–1706
- Holden JC, Vogt PR (1977) Graphic solutions to problems of plumacy. *EOS Trans* 56:573–580
- Holmes A (1944) *Principles of physical geology*, 1st edn. Thomas Nelson & Sons, London, p 532
- Ito GT, Lin J (1995) Oceanic spreading center-hotspot interactions; constraints from along isochron bathymetric and gravity anomalies. *Geology* 23(7):657–660
- Jackson ED, Shaw HR (1975) Stress fields in central portions of the Pacific plate: delineated in time by linear volcanic chains. *J Geophys Res* 80:1861–1874
- Jackson ED, Shaw HR, Bargar KE (1975) Calculated geochronology and stress field orientations along the Hawaiian chain. *Earth Planet Sci Lett* 26:145–155
- Kanasewich ER, Gutowski PR (1975) Detailed seismic analysis of a lateral mantle inhomogeneity. *Earth Planet Sci Lett* 25:379–384
- Kanasewich ER, Ellis RM, Chapman CH, Gutowski PR (1972) Teleseismic array evidence for inhomogeneities in the lower mantle and the origin of the Hawaiian Islands. *Nature* 239: 99–100
- Kanasewich ER, Ellis RM, Chapman CH, Gutowski PR (1973) Seismic array evidence of a core boundary source for the Hawaiian linear volcanic chain. *J Geophys Res* 78:1361–1371
- Kane KA, Hayes DE (1994) A new relationship between subsidence rate and zero-age depth. *J Geophys Res* 99(11):21759–21777
- Katzman R, Zhao L, Jordan TH (1998) High-resolution, two-dimensional vertical tomography of the central Pacific using ScS reverberations and frequency-dependent travel times. *J Geophys Res* 103:17933–17971
- Kaula WM (1983) Minimal upper mantle temperature variations consistent with observed heat flow and plate velocities. *J Geophys Res* 88:10323–10332

- Klein EM, Langmuir CH (1987) Global correlations of ocean ridge basalt chemistry with axial depth and crustal thickness. *J Geophys Res* 92:8089–8115
- Langmuir CM, Klein EM, Plank T (1992) Petrological systematics of mid-ocean ridge basalts: constraints on melt generation beneath ocean ridges. In: Phipps Morgan J et al (eds) *Mantle flow and melt generation at mid-ocean ridges*. American Geophysical Union Geophysical Monograph 71, Washington, DC, pp 183–280
- Larsen T, Yuen D (1997) Fast plumeheads. *Geophys Res Lett* 24:1995–1998
- Lassiter JC, Hauri EH (1998) Osmium-isotope variations in Hawaiian lavas: evidence for recycled oceanic lithosphere in the Hawaiian plume. *Earth Planet Sci Lett* 164:483–496
- Lowman JP, Jarvis GT (1999) Effects of mantle heat source distribution on supercontinent stability. *J Geophys Res* 104(6):12733–12747
- Malamud BD, Turcotte DL (1999) How many plumes are there? *Earth Planet Sci Lett* 174:113–124
- McKenzie D, Bickle J (1988) The volume and composition of melt generated by extension of the lithosphere. *J Petrol* 29:625–679
- Meibom A, Anderson DL (2004) The statistical upper mantle assemblage. *Earth Planet Sci Lett* 217:123–139
- Montelli R, Nolet G, Dahlen FA, Masters G, Engdahl ER, Hung S-H (2004) Finite-frequency tomography reveals a variety of plumes in the mantle. *Science* 303:338–343
- Morgan WJ (1971) Convective plumes in the lower mantle. *Nature* 230:42–43
- Morgan WJ (1972a) Deep mantle convection plumes and plate motions. *Bull Am Assoc Petrol Geol* 56:203–213
- Morgan WJ (1972b) Plate motions and deep mantle convection. In: Shagam R et al (eds) *Studies in Earth and space sciences: a volume in honor of Harry Hammond Hess*. Boulder, Colorado, Geological Society of America Memoir 132, pp 7–22
- Nataf H-C (2000) Seismic imaging of mantle plumes. *Ann Rev Earth Planet Sci* 28:391–417
- Natland JH, Winterer EL (2005) Fissure control on volcanic action in the Pacific. In: Foulger GR, Natland JH, Presnall DC, Anderson DL (eds) *Plates, plumes, and paradigms*. Geological Society of America Special Paper 388, pp 687–710
- Parmentier EM, Morgan JP (1990) Spreading rate dependence of three-dimensional structure in oceanic spreading centres. *Nature* 348:325–328
- Pertermann M, Hirschmann MM (2003a) Anhydrous partial melting experiments on MORB-like eclogite: phase relations, phase compositions and mineral melt-partitioning of major elements at 2–3 GPa. *J Petrol* 44:2173–2201
- Pertermann M, Hirschmann MM (2003b) Partial melting experiments on a MORB-like pyroxenite between 2 and 3 GPa: constraints on the presence of pyroxenite in basalt source regions from solidus location and melting rate. *J Geophys Res* 108:17
- Phipps Morgan J (1997) The generation of a compositional lithosphere by midocean ridge melting and its effect on subsequent off-axis hotspot upwelling and melting. *Earth Planet Sci Lett* 146:213–232
- Plank T, Langmuir CH (1992) Effects of melting regime on the composition of the oceanic crust. *J Geophys Res* 97:19749–19770
- Presnall DC, Gudfinnsson GH (2005) Carbonate-rich melts in the oceanic low-velocity zone and deep mantle. In: Foulger GR, Natland JH, Presnall DC, Anderson DL (eds) *Plates, plumes, and paradigms*. Geological Society of America Special Paper 388, pp 207–216
- Presnall DC, Helsley CE (1982) Diapirism of depleted peridotite: a model for the origin of hot spots. *Phys Earth Planet Inter* 29:148–160
- Presnall DC, Gudfinnsson GH, Walter MJ (2002) Generation of midocean ridge basalts at pressures from 1 to 7 GPa. *Geochim Cosmochim Acta* 66:2073–2090
- Ramberg H (1981) *Gravity, deformation and the Earth's crust*, 2nd edn. Academic Press, London, p 452
- Ribe NM, Christensen UR, Theißing J (1995) The dynamics of plume-ridge interactions; ridge-centered plumes. *Earth Planet Sci Lett* 134(1–2):155–168
- Richter FM (1973) Dynamic models for sea floor spreading. *Rev Geophys* 11:223–287

- Richter FM, Parsons B (1975) On the interaction of two scales of convection in the mantle. *J Geophys Res* 80:2529–2541
- Ritsema J, Allen RM (2003) The elusive mantle plume. *Earth Planet Sci Lett* 207:1–12
- Ritsema JH, van Heijst J (2000) Seismic imaging of structural heterogeneity in Earth's mantle: evidence for large-scale mantle flow. *Sci Prog* 83:243
- Rowley DB (2002) Rate of plate creation and destruction: 180 Ma to present. *Geol Soc Am Bull* 114:927–933
- Salters VJM, Dick BJB (2002) Mineralogy of the mid-ocean-ridge basalt source from neodymium isotopic composition of abyssal peridotites. *Nature* 418:68–72
- Saunders AD, Jones SM, Morgan LA, Pierce KL, Widdowson M, Xu YG (2007) Regional uplift associated with continental large igneous provinces: the roles of mantle plumes and the lithosphere. *Chem Geol* 241:282–318
- Schilling JG (1973a) Iceland mantle plume: geochemical study of Reykjanes ridge. *Nature* 242:565–571
- Schilling JG (1973b) Mantle plume–spreading ridge system: geochemical evidence. *Eos Trans Am Geophys Union* 54:243
- Seth HC (1999) Flood basalts and large igneous provinces from deep mantle plumes: fact, fiction, and fallacy. *Tectonophysics* 311:1–29
- Seth HC (2003) Beyond the plume hypothesis. *Curr Sci* 85(11):1518–1520
- Shaw HR, Jackson ED (1973) Linear island chains in the Pacific: result of thermal plumes or gravitational anchors? *J Geophys Res* 78:8634–8652
- Shaw HR, Jackson ED, Bargar KE (1980) Volcanic periodicity along the Hawaiian-emperor chain. *Am J Sci* 280A (Jackson volume): 667–708
- Shen Y, Forsyth DW (1992) The effects of temperature- and pressure-dependent viscosity on three-dimensional passive flow of the mantle beneath a ridge-transform system. *J Geophys Res* 97(B13):19717–19728
- Sipkin SA, Jordan TH (1975) Lateral heterogeneity of the upper mantle determined from the travel times of ScS. *J Geophys Res* 80:1474–1484
- Stolper EM, Walker D (1980) Melt density and the average composition of basalt. *Contrib Mineral Petrol* 74:7–12
- Tackley P (1998) Three dimensional simulations of mantle convection with a thermo-chemical basal boundary layer. In: Gurnis M, et al (eds) *The core mantle boundary region*. American Geophysical Union, Washington, DC, *Geodynamics Series* 28, pp 231–353
- Tozer DC (1973) Thermal plumes in the Earth's mantle. *Nature* 244:398–400
- Turcotte DL, Oxburgh ER (1973) Mid-plate tectonics. *Nature* 244:337–339
- von Herzen RP, Cordery MJ, Detrick RS, Fang C (1989) Heat-flow and the thermal origin of hot spot swells: the Hawaiian swell revisited. *J Geophys Res* 94:13783–13799
- Weaver B (1991) Trace element evidence for the origin of ocean-island basalt. *Geology* 19: 123–126
- Wilson JT (1963) A possible origin of the Hawaiian Islands. *Can J Phys* 41:863–870
- Woods M, Okal E (1996) Rayleigh-wave dispersion along the Hawaiian swell: a test of lithospheric thinning by thermal rejuvenation at a hot spot. *Geophys J Int* 125:325–339
- Wright C (1975) Comments on “Seismic array evidence of a core boundary source for the Hawaiian linear volcanic chain” by E.R. Kanasewich et al. *J Geophys Res* 80:1915–1919
- Yaxley GM (2000) Experimental study of the phase and melting relations of homogeneous basalt + peridotite mixtures and implication for the petrogenesis of flood basalts. *Contrib Miner Petrol* 139:326–338
- Zindler A, Hart SR (1986) Chemical geodynamics. *Ann Rev Earth Planet Sci* 14:493–571